Electrospun Hydroxyapatite-Containing Chitosan Nanofibers Crosslinked with Genipin for Bone Tissue Engineering Applications

A Thesis

Submitted to the Faculty

of

Drexel University

By

Michael E. Frohbergh

in partial fulfillment of the

requirements for the degree

of

Doctorate of Philosophy in Biomedical Science

October 2012

Acknowledgements

I would like to extend my deepest gratitude to all of the people that have helped me on this journey through my PhD Thesis work.

To my thesis advisor, mentor and friend Dr. Peter Lelkes, I offer my thanks in the highest regards. Your guidance and academic prowess gave me the tools I needed to complete my work in an independent and timely manner and develop the work ethics I have in the laboratory today. When I started here at Drexel, your skepticism was warranted. However, over the past five years, my maturity and knowledge in the field has increased exponentially and will continue to grow from the life lessons I have obtained from you. Your kind hearted nature and drive for success is truly an inspiration to me and I will carry that with me to all of the endeavors I undertake from here out. I wish you all of the best at your new position and cannot wait to see the progress of bioengineering in Philadelphia due to your presence.

To Dr. Kurt Hankenson, a great collaborator at the University of Pennsylvania, I give much praise for your knowledge in animal models and bone development. Our fruitful conversations early on when the animal projects were first being discussed helped me to develop the appropriate models for optimal results. Your knowledge in the field is insurmountable and will follow me wherever I go.

To Dr. Norman Johanson, your contribution to the field of tissue engineering research from the clinical side is unmatched. With such collaborations, our research in the lab does not go in vein and has the potential to see clinical applications and acceptance. I

hope to maintain this relationship with you in the future and build on models to eventually reach the clinic and help save lives.

To Dr. Jeff Oristaglio, your mentorship and guidance for *in vivo* work was the final stepping stone to getting me through my thesis. Your patience with me as I learned the techniques is much appreciated. Without the use of your equipment and laboratory, I would more than likely still be running around trying to figure out where and how to do these surgeries. For this, I am most grateful.

To Dr. Philip Lazarovici, a great friend and mentor who helped me get my first publication in order. Without your constant persistence to push to get it written and completed, it may very well still be sitting on the shelf. Your friendship and guidance throughout these five years was imperative to me finishing with such high regards. You taught me a lot about what it is to be a successful research scientist and writer. These attributes are invaluable and will help me to develop my career as I progress.

To Dr. Anna Katsman, who is responsible for molding me into a productive and organized scientist, I offer my esteemed gratitude. Your friendship, intellectual input and general positive outlook on life helped me to become who I am today and I am forever indebted to you for this. I will never forget the year that we spent together in the lab, the production that came about from your presence and for whipping me into shape and getting me organized, focused and on the right track. Good luck with the rest of your ortho residency.

To my lab members, I would not be where I am at now without your constant support and friendship. Everyone in the Lelkes lab displays hard work and perseverance, which

is contagious and has rubbed off on me for the best. I would like to thank Jessica Falcon, Collin Stabler, Gozde Senel, Seda Karamil, Patrick Thompson, Yah-el Ha-rel, Shimon Lecht and all of the others who have come through the lab. You have all been the greatest of friends through this time and have offered great intellectual help as well as great escape from intellect when required. Our friendship will last a lifetime.

A special thanks to lab members Sean Devlin and Jonathan Gerstenhaber and especially to Dr. Mark Mondrinos, for their aid in getting this thesis finished. Sean and Jon, I could not have done the modeling without your assistance and this will not be forgotten. Thank you very much for your continued support. Mark, your help with the histological analysis really drove home the finishing touches for the chitosan story. You have kept me sane throughout these last couple of months that you have rejoined the Lelkes lab and have been a truly great friend. And I fear this is only the beginning of our work and friendship over a long period of time…

A special thanks to Mie Pimton, who helped me to generate my PCR data and in the formatting of this document. Her intellectual help in the lab and friendship outside of the lab have proven to be instrumental in me achieving my goal and having such a great and fulfilled time here in the Lelkes Lab. I will cherish your friendship forever and keep in touch with you as you move forward to do big things in Thailand.

A special thanks to Dr. Anant Chopra, who has been one of my best friends throughout my thesis endeavors. His constant blabbing about science has inspired me to always think outside of the box and stay motivated, on top of the field and productive in my experiments. His knowledge is superior to many at his level and he will undoubtedly

be one of the most successful scientists I had the pleasure of spending my five year PhD experience with. Good luck at UPenn my friend.

To all of the previous Lelkes lab members who were integral to my initial years at Drexel, I offer my thanks for the introduction. Leko Lin, Jingia Han, Devika Varma and Anat Katsir, your help and guidance when I was beginning is undeniably what got me to where I am at now. A special thanks to Anat (lab mom) who was always there for help and to help calm me down when I was losing it. Also, a very special thanks to Greg Botta, whom was a great mentor and offered a great deal of help and intellectual support throughout this endeavor. Your friendship was crucial throughout these times and it would have been impossible to succeed without it.

To all of my friends outside of the lab who have kept me going through these times, even when I was down and ready to quit. Mario Corrado, Ted Jabara, Caitlin Brown, Anthony Aldorasi, Chris Haines and Brad Giosa, you have all been my friends forever now and I know this will continue for a lifetime. Your support and help through my thesis and my outlet to get out of science when necessary will always be remembered and for this I love all of you.

A special thanks to Lisa Williams, Natalia Broz, Danielle Crocker, Frank Kepics, Dolores Conver and everyone else in the Biomed office and department for the continued help and support with all administrative issues. You all are so patient and understanding when all of us come to you with problems and this should never go overlooked. It takes a lot to deal with these issues and all of us students on a daily basis and for this we/I are truly grateful for your continued support.

Last, but certainly not least, to my family, to whom I owe all of this. Without your constant love and support, this simply would have been impossible. To my mom and dad, Donna and Rich, this entire life endeavor is attributed to your unbelievable patience, love and dedication to your beliefs in my abilities. You have never given up on me and now I have shown you why that was a good choice. To my sister and brother, Karyn and Dennis, I love you both with all of my heart. Thank you for being the absolute best siblings a brother could ask for. I love all of you and this is for you.

Table of Contents

List of Figures

Abstract

Electrospun Hydroxyapatite-Containing Chitosan Nanofibers Crosslinked with Genipin for Bone Tissue Engineering Applications

Michael Frohbergh

Dr. Peter I. Lelkes, PhD

Reconstruction of large bone defects remains problematic in orthopedic and craniofacial clinical practice. Engineering a functional scaffold mimicking the architectural structure of bone and the regenerative capacity of periosteum offers a potential solution. Electrospun nanofibrous scaffolds are superior in surface area, biomimetic properties, and architecture for the proliferation, and differentiation of osteoprogenitor cells. Chitosan (CTS), the deacetylated form of chitin found in the exoskeleton of crustaceans, is a versatile biomaterial with structural similarity to the extracellular matrix (ECM) of bone.

In this thesis, the need of fabricating a regenerative material for bone tissue engineering is addressed by demonstrating the ability of genipin crosslinked electrospun chitosan (CTS-GP) nanofibers mineralized with hydroxyapatite (CTS-HA-GP) to act as osteogenic templates capable of supporting osteoblast adhesion and differentiation with the potential to induce mesenchymal stem cell differentiation and craniofacial regeneration *in vivo.* Fibrous scaffolds with average fiber diameters of 227±154 nm as spun and 335±119 nm after crosslinking with genipin were generated. Physical, chemical and mechanical analyses were performed for scaffold characterization as well as

cytocompatability and osteogenic expression of 7F2 mouse osteoblasts to demonstrate the ability of these scaffolds to support functional osteoblasts. Induction was also observed by the capacity of these scaffolds to induce osteogenic differentiation of human bone-marrow derived mesenchymal stem cells *in vitro.* Finally, the osseointegrative capacity of these scaffolds was observed by *in vivo* implantation into a murine calvarial defect model, demonstrating no immunorejection and the early presence of calcified tissue formation.

Furthermore the need for enhanced porosity in electrospun scaffolds to induce proper cell infiltration into the scaffold using mesenchymal stem cells on PLGA scaffolds with sacrificed gelatin fibers was also explored. PLGA was used to look into optimizing an appropriate scaffold for bone regeneration due to its ease in fabrication and manipulation by observing mechanical properties and porosity at different ratios compared with cell infiltration. However, it was observed that the gelatin was not being removed as hypothesized and was rather modifying the physical properties of the scaffold. A mathematical model was developed to describe cell proliferation across the scaffolds and cell infiltration into the scaffold.

List of Publications

The following are published journal articles, patents and pending manuscripts in print or to be submitted that the following work is based on

1. Frohbergh ME, Katsman A, Botta GP, Lazarovici P, Schauer CL, Wegst UG, et al. Electrospun hydroxyapatite-containing chitosan nanofibers crosslinked with genipin for bone tissue engineering. Biomaterials. 2012.

2. New PCT Patent Appl. No. PCT/US11/55209, filed October 7, 2011 (Claims priority to U.S. Prov'l Appl. No. 61/390,918, filed October 7, 2010). Title: Electrospun Mineralized Chitosan Nanofibers Crosslinked With Genipin For Bone Tissue Engineering

3. Frohbergh ME, Katsman A, Mondrinos M, Pimton P, Hankenson K, Oristaglio J, Lelkes P. Bridging the Gap: The Osseointegrative Properties of Electrospun Hydroxyapatite-Containing Crosslinked Chitosan Nanofibrous Scaffolds. Manuscript in Progress

Chapter 1. **Introduction**

1.1 Tissue Engineering, Biomaterials and Regenerative Medicine

Tissue engineering is a multidisciplinary field aimed at revolutionizing the way we diagnose and treat disease and improve the quality of life. It utilizes tools from biology, engineering and medicine to develop tissues and organs either in or outside of the body for diagnostic evaluation and eventual implantation. From a material engineering stance, the fabrication of natural and synthetic scaffolds to act as templates to allow proper tissue formation and regeneration is a cornerstone foundation for tissue engineering. From a biological stance, the use of specific growth factors, biomolecules and signaling cues aims at creating the appropriate spatial and temporal environment that the human body experiences during organogenesis and development. The focus of this thesis will be the union of these two concentrations to create biomimetic scaffolds that aim at inducing bone tissue regeneration which is further complemented by the presence of cells to induce biological cues responsible for inducing enhanced interaction between the native tissue and the fabricated scaffolds. To date, engineered scaffolds are generally lacking in the ability to either fully integrate with the surrounding tissue or are incapable of driving specific regeneration. However, incorporation of cellular or biological components has shown to greatly enhance the integrative and regenerative capacity of these scaffolds. Here, we observe this phenomenon using electrospun scaffolds to mimic the natural extracellular matrix structure and organization along with the presence of mesenchymal stem cells to enhance osteoconduction.

1.2 Significance for the Advancement of Bone Tissue Engineering

The field of bone tissue engineering focuses on developing regenerative materials, rather than the standard replacement materials that are available today. Current strategies for bone replacement involve using inert materials to replace the structural properties of bone and also aid in the general functionality of support that the skeletal system provides. However, few therapies focus on the regeneration of tissue. A major issue with replacing bone is stress shielding. When using inert materials such as metals to repair bone fractures, the implant takes on the entire normal load that the bone is usually subject to. This mechanical stimulation causes the natural processes of resorption and renewal of bone. When the load is removed and placed onto a permanent implant, the bone no longer goes through this process and begins to degrade over time, leading to complications such as osteoporosis and weakened tissue leading to new fractures. It is for reasons like this that new substitutes are required to aid in bone regeneration rather than replacing in load bearing bones.

In non-load bearing bones, such as cranial and maxillofacial bones, there is also more focus on replacement rather than studying strategies crucial to induce natural regeneration. Craniofacial reconstruction involves the remodeling of the malformed or fractured skull or facial bones due to a genetic disorder or traumatic injury. In the United States alone, nearly 227,500 children are born with birth defects to the skull, head or face yearly. Such birth defects can lead to serious cosmetic and potentially life threatening issues. Special surgical techniques must be implemented with children considering that the bones are still undergoing development and not fully matured [6].

In adults, craniofacial surgery is usually required after a traumatic head injury due to combat or accidents or when large tumors affect the integrity of craniofacial bones or soft tissue. In 2001, almost 25,000 people in the U.S. needed maxillofacial surgery as a result from trauma [6]. The National Cancer Institute estimates that annually nearly 250,000 people in the U.S. suffer from orbital cavity and throat related cancers, 40,000 from bone and joint cancers and 130,000 from brain tumors which result in cranial resection for removal [7]. Critical size defects are fractures or pathologic areas that will not spontaneously heal on their own [8]. The surgeries necessary to restore these areas can sometimes leave the patient disfigured causing psychological problems and decreased quality of life. [6].

Bone grafting is the conventional practice in the reconstruction of critical size bone defects, most commonly using autologous bone harvested from the patient. However, there are several issues with this method. These autografts introduce a secondary operative site (usually the illial crest), which can lead to complications including donor site morbidity, infection, pelvic instability, hematoma development and pelvic fracture [9, 10]. If a large graft is needed, the secondary site tends to be limited in its ability to compensate without causing permanent damage [11]. Furthermore, chronic pain has been reported from the donor site, which leads to a decrease in the patient's quality of life [12].

Within the past 30 years, a variety of different types of biomimetic matrices in place of autologous grafts have been explored. Ideally these would be both osteoconductive (enhancing the invasion of bone progenitor cells into an inert matrix) and osteoinductive, i.e. promoting the transformation of these recruited precursor cells into osteoblasts to

form new bone [13]. These matrices can be either inorganic, such in the case of hydroxyapatite (HA) [14-16], or organic as in demineralized bone matrix (DBM) [17].

1.3 Bone Anatomy, Physiology and Function

The macroscopic structure of bone, though varying among different types of bone, is generally broken up into a number of different segments. The diaphysis is the shaft of a bone, while the epiphysis is the ends. The metaphysis connects the diaphysis and the epiphysis. The epiphyseal plate (or growth plate) is responsible for elongating bones during development. Bone marrow resides in the medullary cavity, which is located in the center of most bones. The medullary cavity is lined with trabeculae, which is the main constituent of trabecular bone. The inner and outer layers of bones are the endosteum and periosteum respectively [18]. Hyaline cartilage covers joints to produce lubrication and reduce friction. Figure 1 depicts the basic structure of long bones in the body.

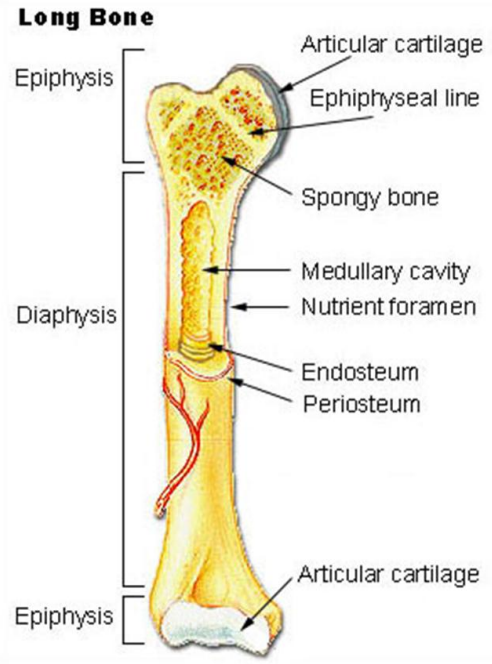

Figure 1. The typical anatomy and structure of bone. The two main segments of long bone are epiphysis and diaphysis. Bone consists of compact bone and trabecular bone. The outer lining is the periosteum and the inner lining is the endosteum. The medullary cavity contains bone marrow. Image taken from http://thesebonesofmine.wordpress.com/2011/02/28/the-biological-basis-of-bone-anatomical-directional-terms/

There are two main types of bone found in the human body, namely primary bone, which is also called non-woven bone, and secondary bone, which is mature bone. Primary bone is the initial bone that forms during development and regeneration. It is composed of a large number of osteocytes and irregularly arranged collagen fibers. Over time, primary bone is replaced by secondary bone, the mature bone that is present throughout a fully developed human, characterized by its dense mineralization and organized structure [19].

The two types of secondary bone found in the body are cortical bone and trabecular bone. Cortical bone composes the outer mineralized surface while trabecular bone is

within and contains the bone marrow, where hematopoietic and mesenchymal stem cells reside. The hierarchical structure of cortical bone is organized into a lamellar structure, which is composed of osteons surrounding Haversian canals, where blood vessels and neurons enter bone. Lacunae are small cavities in the osteons which contain osteocytes, cells that are responsible for maintaining the bone. Canaliculi are small canals that allow small blood vessels to connect lacunae for cellular communication and nutrient/waste transfer between osteocytes. Along with osteons, there are also the outer circumferential lamellae, which is the outermost layer of bone connected to the periosteum and the inner circumferential lamellae, which completely encircles the bone marrow [18]. The hierarchical structure of compact bone is depicted in Figure 2. Trabecular bone is where bone marrow resides. Bone marrow aid in bone regeneration, as it houses mesenchymal stem cells that can be differentiated into osteoblasts for bone formation. It is also highly vascularized and is a site for hematopoietic progenitor cells [18, 19]. The structure of trabecular bone can also be seen in Figure 2.

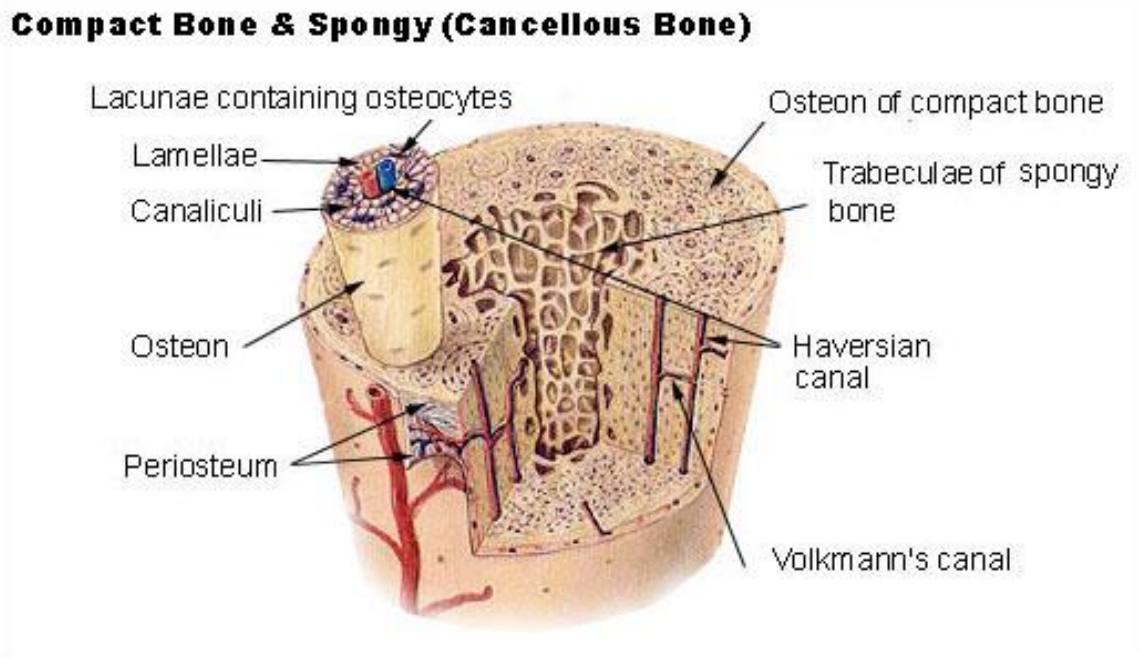

Figure 2. The hierarchical structure of compact bone. The microstructure is composed of an organized lamellar structure containing osteons containing lacunae as the functional unit of bone and the Haversian system containing vasculature and nerves inter-connected by canaliculi. The inner region is trabecular bone where hematopoietic and mesenchymal stem cells reside. Image taken from the National Cancer Institute page of Bone Structure. http://training.seer.cancer.gov/anatomy/skeletal/tissue.html.

There are four specific types of cells in bone tissue. Osteoprogenitor cells are mesenchymal stem cells that undergo osteogenic differentiation into osteoblasts. They are most active during development of the skeletal system, but are frequently reactivated during the normal bone turnover process and large numbers are activated during fracture repair. They reside mainly in the periosteum, or outer layer of bone, and can also be found in the endosteum, the inner layer of bone, and lining the canals. Osteoblasts are responsible for bone remodeling. They consistently lay down the organic matrix of bone, which is called osteoid. Once an osteoblast has completely surrounded itself with osteoid, it is called an osteocyte. Osteocytes maintain bone in adults. The resorption of bone is performed by osteoclasts. These are large, multi-nucleated cells that

enzymatically digest bone matrix and deposit it into circulation via endocytosis. The turnover process of bone is the term given to the constant remodeling of bone during adulthood. Osteoblasts are much more active during development, however the ratio of matrix deposition to matrix resorption steadily evens out with age. [20]. Figure 3 illustrates the different types of cells found in bone tissue. At some point, the ratio of resorption may become larger than deposition, which can lead to bone degenerative diseases mainly seen in senior citizens, such as osteoporosis.

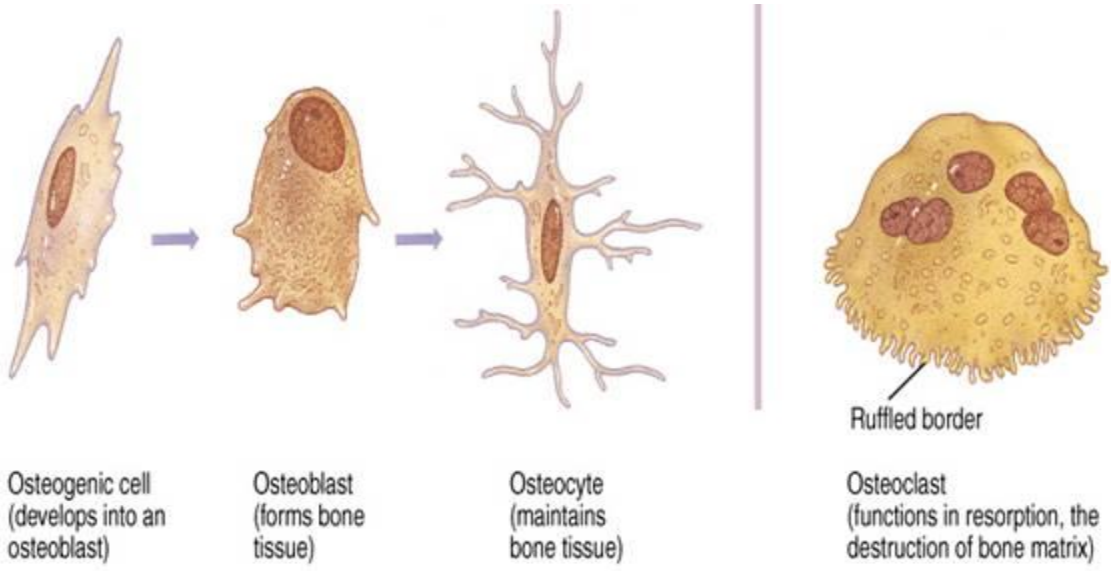

Figure 3. The progression of osteogenic progenitor cells leads to osteoblasts which synthesize bone matrix and osteocytes which maintain it. Osteoclasts are larger cells responsible for bone resorption. A balance in matrix deposition from osteoblasts and matrix resorption from osteoclasts leads to homeostatic turnover. When the ratio begins to favor resorption, degenerative diseases like osteoporosis are observed. Image taken from http://spaces.imperial.edu/thomas.morrell/cha_6_tortora_bone_tissue.htm.

The outer layer of bone is called the periosteum. The periosteum is divided into an outer fibrous layer, containing mainly fibrous ECM proteins and molecules as well as fibroblasts and is highly vascularized, while the inner cambium layer is composed of periosteal cells. These cells are multipotent cells shown to be capable of differentiating

into osteoblasts and chondrocytes [21, 22]. Sharpey's fibers are large bundles of collagen fibers that affix the periosteum to cortical bone. During development, sharpey's fibers are low in number, allowing the periosteum to move more freely, causing a much more highly activated layer of osteoprogenitor cells to induce tissue formation. Periosteum plays a large role in the initiation of bone regeneration during injury [2, 19, 20, 23]. Figure 4 shows the layers and structure of periosteum. The inner layer of bone, the endosteum, is a thin layer of osteoprogenitor cells, osteoblasts and connective tissue that attaches the cortical bone to the trabecular bone [20].

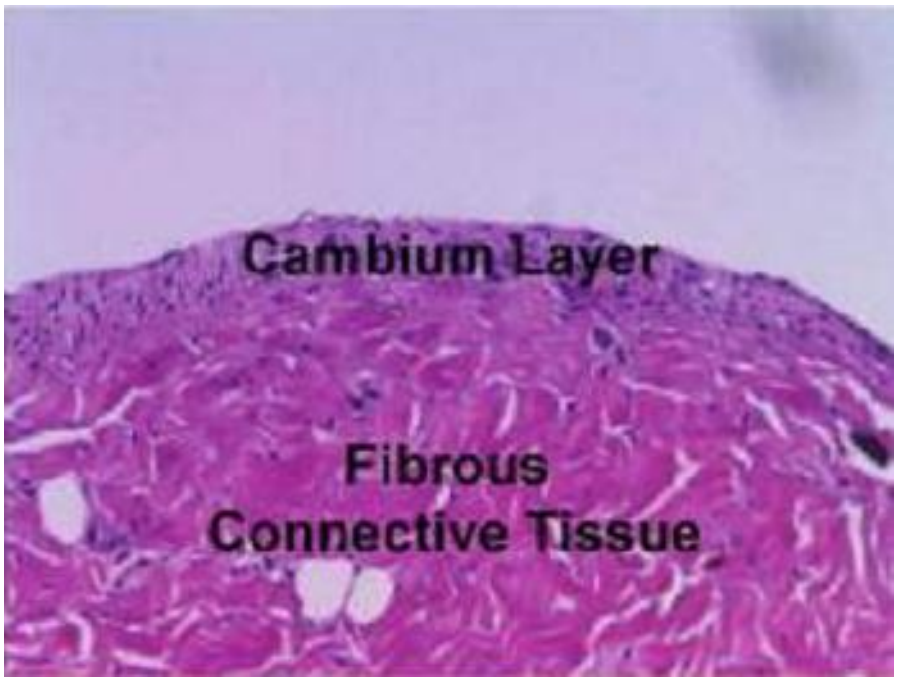

Figure 4. The periosteum is divided into two distinct layers. The fibrous layer contains Sharpey's fibers which are responsible for attaching the periosteum to the surface of cortical bone. The inner cambium layer is an osteoprogenitor-rich cell layer which is highly active during development. It also plays a key role in the initiation of wound healing [2].

The two main functions of bone tissue are structural support and internal organ protection. A very tight interaction between the skeletal system and the muscles, tendons and ligaments in the body give animals and vertebrates the wide range of motion and stability we need to survive. Also, cranial bones, rib cages and other regions provide protection for vital internal organs such as the brain, heart, lungs, etc. What distinguishes bone from other connective tissue is the presence of a highly mineralized, hence dense and rigid matrix. Bone matrix consists of an organic component (mainly collagen I) and an inorganic component (hydroxyapatite) [18-20]. This biphasic nature is unique to all other tissues in the body and gives bone the structural integrity for support, mobility and protection.

1.4 Bone Development

Bone development generally occurs in two distinct ways. Endochondral ossification is the mineralization of cartilage matrix converting it into bone matrix. Intramembranous ossification is the direct deposition of bone matrix from osteoblasts. Both begin with the production of non-woven immature bone, can lead to the formation of cortical and trabecular bone and are crucial for normal skeletal development. Endochondral ossification is initiated by chondrocyte hypertrophy and intramembranous ossification from osteoblasts surrounding the cartilage matrix. As chondrocytes die, osteoblasts infiltrate and begin to mineralize the cartilage matrix, resulting in bone tissue. The perichondrium, or outer layer of cartilage, becomes infiltrated by osteoprogenitor cells and vasculature and becomes periosteum. This blocks nutrient flow to all surrounding chondrocytes and they die. The resulting product is newly formed bone tissue. Generally, endochondral ossification produces the short and long bones of the skeletal system. Cartilage remains in two places after endochondral ossification, as hyaline cartilage covering the joints and in the epiphyseal plate, which continues to grow as cartilage and elongate bones to their proper length, when the epiphyseal plate is then replaced by the epiphysis [18, 20, 24]. The steps of endochondral ossification are illustrated in Figure 5.

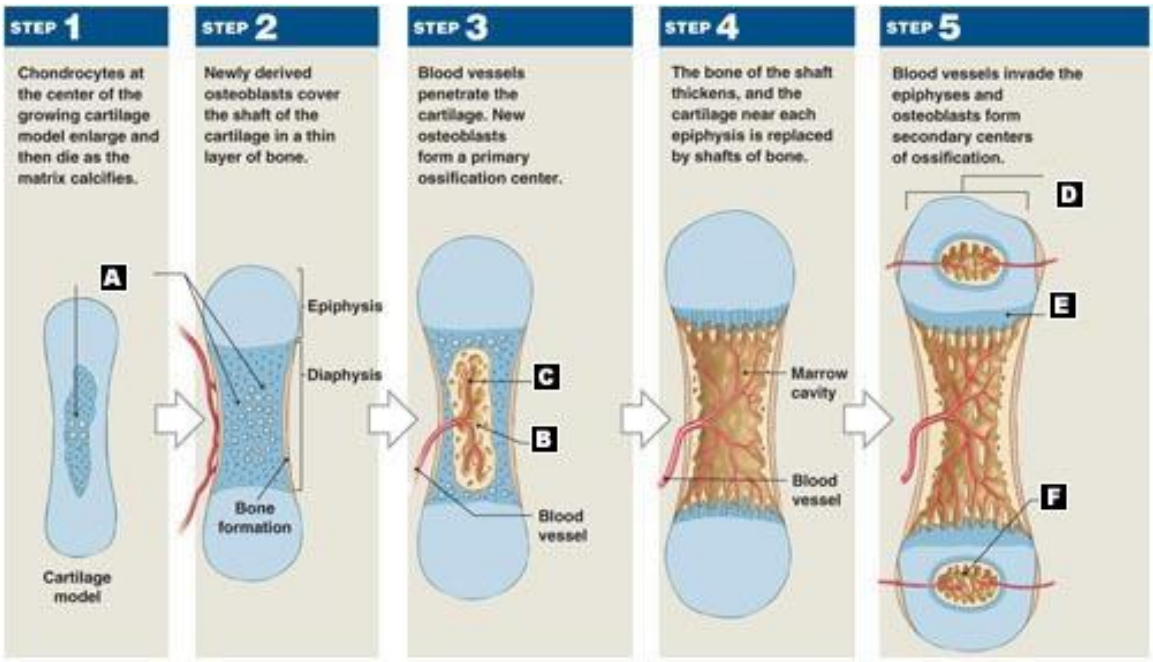

Figure 5. A representative schematic of endochondral ossification illustrates the steps involved for bone development. Cartilage tissue begins to calcify as osteoblasts invade the region and begin depositing matrix (step 1). As osteoblasts begin to proliferate, chondrocyte hypertrophy occurs resulting in apoptosis (step 2). As vasculature penetrates the newly forming bone matrix, osteoblasts proliferate further and form ossification centers which eventually completely replace the cartilage (steps 3 and 4). As blood vessels spread, the osteoblasts begin to form the mature structure of bone tissue including the formation of lacunae for osteocytes and the Haversian/canaliculi system for vascular penentration (step 5). Image taken from http://wps.aw.com/bc_martini_eap_5/108/27708/7093409.cw/index.html

Intramembranous ossification is the production of mineralized bone matrix by osteoblasts and is usually responsible for the formation of flat bones, such as cranial and maxillofacial bones. This process is initiated in highly vascularized mesenchyme areas, where mesenchymal stem cells begin to differentiate into osteoblasts. As the osteoblasts begin to become surrounded by matrix, they become osteocytes. Separate colonies of osteocytes and bone matrix form an irregular collagen I matrix (primary bone) which grow quickly and begin to fuse. Areas of mesenchymal stem cells that do not differentiate give rise to the bone marrow. Areas that do not calcify become the periosteum and endosteum [18, 19, 24].

1.5 Fracture Repair

During injury in long and short bones, bone cells and matrix are destroyed. Initiation of healing begins by clotting from the surrounding vascularization. Clots, remaining bone matrix debris and cells are removed by macrophages, which is followed by the formation of granulation tissue. Granulation tissue is replaced by endochondral ossification, where fibrocartilage begins to form which is slowly replaced by calcified bone matrix and osteoblasts [25].

In irregular and flat bones, a similar process of clearing, clotting and granulation occurs. However, this is followed by intramembranous ossification due to the large presence of mesenchymal tissue in these areas. In summary, repair occurs similarly to the processes of development. However, in some instances, defects are too large to be healed by spontaneous bone formation. It is these instances where replacement materials are used and the need for tissue engineered constructs to induce regeneration and bridge these large gaps becomes relevant [25].

Chapter 2. **The Role of Periosteum in Bone Regeneration**

Although it is clear that osteoprogenitor cells reside in the cambium layer of the periosteum [2], the origins of these periosteal cells still remain unknown. Osteoprogenitor cells are hypothesized to originate from mesenchymal stem cells. Based on the biomarkers present, there is a lack of evidence for the origin of these osteoprogenitor cells during fracture repair and if there are other cells present as well [18]. The cellular signaling that regulates the stages of repair, including inflammation, differentiation and bone formation are not well studied.

As mentioned, the current gold standard for craniofacial reconstruction involves autologous graft materials due to the presence of an intact and functional periosteal layer [23, 26]. Current methods for manufacturing bone grafts from either synthetic/natural materials or the use of donor grafts from cadavers are not optimal due to the lack of a functional periosteum [23]. Engineered materials lack the ability to successfully integrate with the host tissue and fail to induce osseointegration. This integration between the host and the graft is what will cause the migration of osteoprogenitor cells into the graft from the host and induce quicker, more regenerative responses and bone formation.

In the skull, the outer fibrous layer of the periosteum consists of fibroblasts and Sharpey's fibers, which are responsible for binding the cranial bones firmly, but at the same time allowing them to move and absorb shock or trauma. These fibers are most abundant in areas where bones are commonly subjected to the greatest forces in separation. The inner layer of the periosteum harbors multipotent cells that have a fibroblast like morphology and can differentiate towards either a chondrogenic or an osteogenic lineage. [21].

Cell labeling and tracking has shown the contribution of the periosteum and endosteum to bone healing to be about 90% while other resident stromal cells and circulating marrow cells contribute to as low as 10% during the healing process. One study demonstrated the importance of the periosteum in bone regeneration by removing it from an autograft prior to implantation. A 73% decrease in new bone formation occurred when the periosteum was missing, as well as a 10-fold decrease in neovascularization. There was also a 75% decrease of osteoclast migration onto the bone scaffold, which led to poor remodeling of the damaged area and a hindrance in new bone formation. On the other hand, removal of bone marrow cells had a minimal effect on the regenerative capacity of the autograft [27].

Another study observed the migratory patterns of periosteal cells onto a graft. It was observed, using β-Galactosidase as a tag, that the cells were mainly seen to localize on and around the graft, differentiating into osteoblasts, chondrocytes, osteocytes and vessel lining cells. This study shows the multipotency of these cells as well as shows that they tend to remain on the surface of the graft rather than migrating into it. By days 7 and 10, 70% and 90% of the cells present on the surface of the graft were β-Gal positive respectively. This indicates that the periosteal cells are crucial in beginning the healing process of a bone fracture or injury. Further, by day 28, most cells were β-Gal negative, indicating that as healing progresses, the host cells begin to infiltrate the scaffolds and the role of the periosteum as an initiator is complete [28].

Although the molecular signaling involved in the initiation and morphogenesis of periosteal bone healing is not well defined, a number of molecules, such as BMPs, Hedgehog proteins and Wnt proteins are known to play active roles. FGFs and IGFs

have also been shown to be upregulated in bone healing [23]. The general consensus suggests that the wound healing shares some similarities with the natural fetal limb budding and normal bone development. Some studies suggest that BMP-2 is upregulated during the formation of the periosteal callus, which is the initiator to bone healing during a cortical bone fracture [29]. Interestingly, knockout of BMP-2 during organogenesis does not cause any irregularities during bone development, however it has shown to disrupt the progression of healing during injury (Figure 6) [4]. Similarly, it is known that hedgehogs and Wnt proteins are involved processes such as differentiation and morphogenesis, however their involvement in bone healing is still unknown [30].

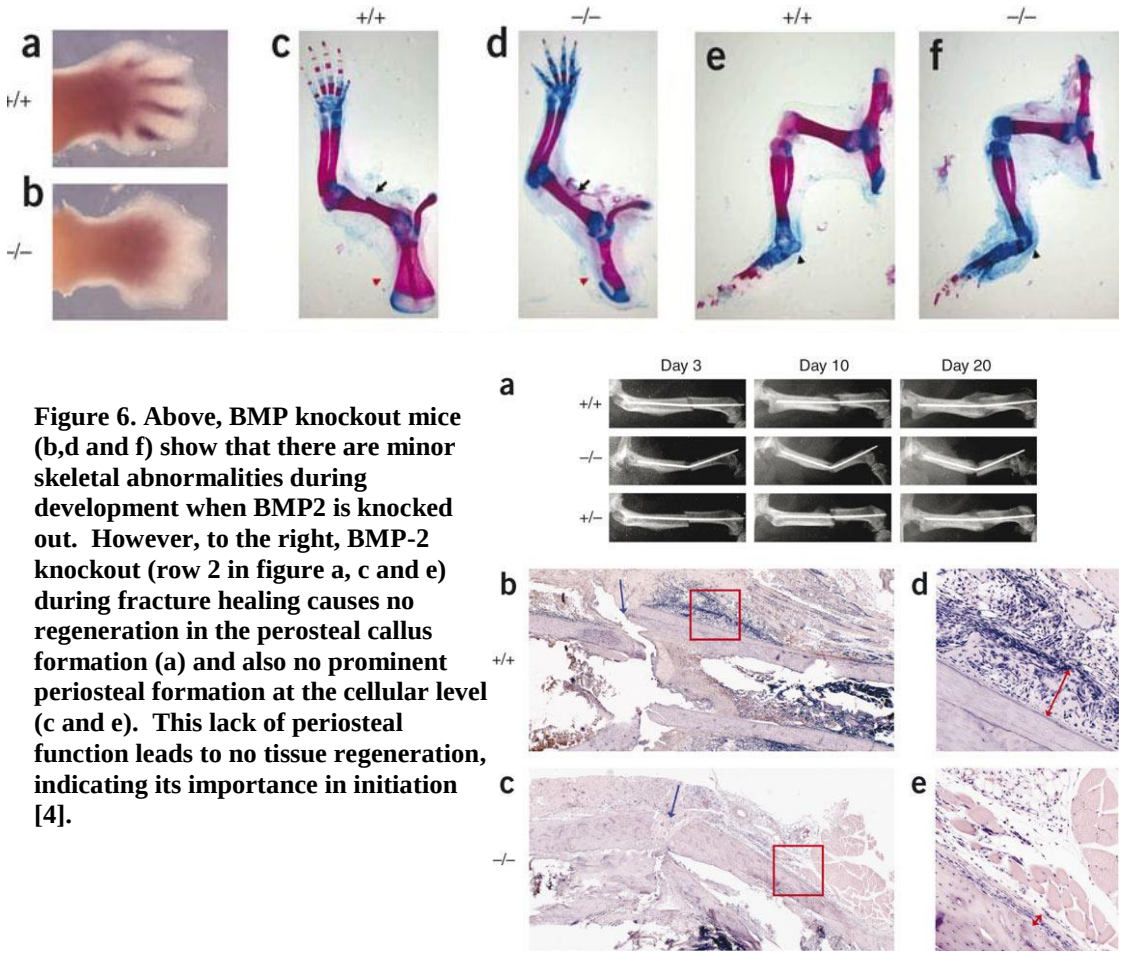

Figure 6. Above, BMP knockout mice (b,d and f) show that there are minor skeletal abnormalities during development when BMP2 is knocked out. However, to the right, BMP-2 knockout (row 2 in figure a, c and e) during fracture healing causes no regeneration in the perosteal callus formation (a) and also no prominent periosteal formation at the cellular level (c and e). This lack of periosteal function leads to no tissue regeneration, indicating its importance in initiation [4].

The main component of the periosteum responsible for healing is the cellular component. It is these cells that begin the healing process. It is also the reason that allografts and engineered materials are not nearly as successful as autografts. Studies have shown that covering the surface of allografts with living tissue can increase bone regeneration. For example, seeding an allograft with mesenchymal stem cells expressing BMP2 enhanced bone remodeling, angiogenesis and the mechanical stability of the allograft due to host/graft incorporation [31]. Moreover, PCL/calcium phosphate graft seeded with porcine stromal cells was capable of forming new bone tissue when

implanted subcutaneously in a rat model. The study showed that endochondral ossification was initiated and bone formation was achieved (Figure 7) [3].

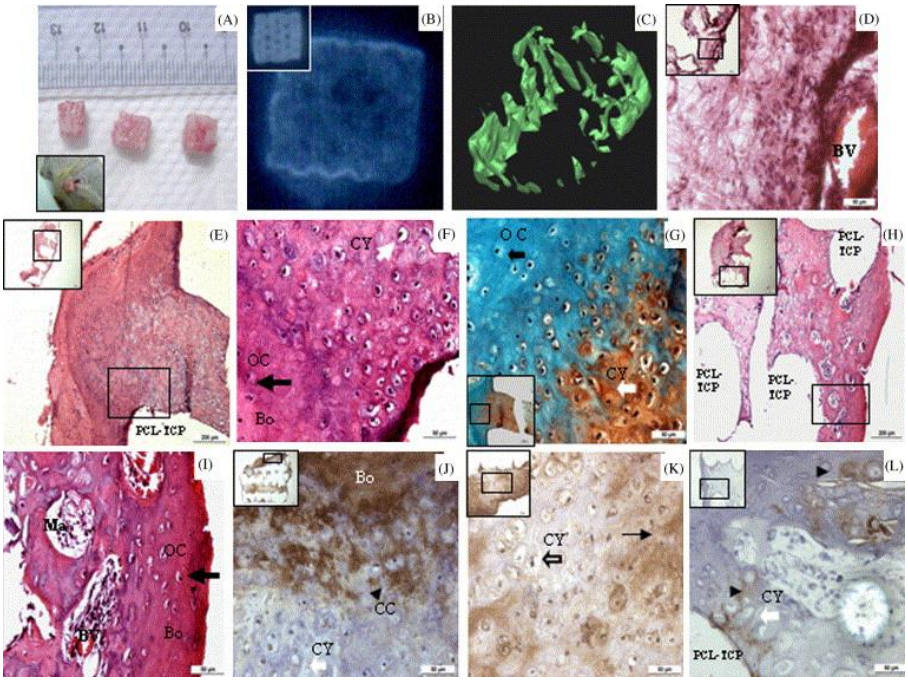

Figure 7. Scaffold constructs wrapped in cell sheets were seeded with cells for 49 days and harvested after 28 days. They showed good vascularization (a), osteogenesis (b, c and e) as opposed to fibrous tissue without cells sheets and endochondral ossification (f and g). Cortical bone and marrow cavities were observed (h and i) and specific bone and cartilage markers osteocalcin (j), collagen I (k) and collagen II (l) [3].

Another potential solution to enhancing the potency of allograft bone substitutes is to use a type of periosteal covering around the allograft, either with a cell sheet or engineered material. The main goal here is to induce osseointegration of the host bone with the allograft via cell signaling and recruitment from the covering. The main problem with allografts is they do not induce osseointegration, so the graft remains decellularized and leads to the formation of necrotic tissue that cannot mimic bone in structure or mechanical properties [3, 32, 33]. This all begins with proper and appropriate vascularization, which has been shown to have a reciprocal effect on

osteogenesis. Factors such as VEGF, PDGF not only aid in vascularization, but also aid in bone formation as well. Also, FGFs and BMPs also aid in vessel formation, which shows that all of these angiogenic and osteogenic factors work synergistically, indicating the necessity and upmost importance of vessel formation for bone healing. With vascularization of the allografts via periosteal wrapping, new, viable bone tissue can be formed rather than necrotic tissue that leads to fibrosis and poor mechanical strength [34].

The three main criteria to produce a periosteal sleeve around a graft material are live osteogenic cells, osteoinductive genes or factors and an osteoconductive scaffolding material. In terms of cell sourcing, the most common choices are mesenchymal stem cells derived from the bone marrow or adipose derived stem cells, as well as periosteal cells [23]. These cell types offer a unique opportunity to avoid ethical issues involved with embryonic stem cells as well as provide a renewable and autologous cell source. Interestingly, fibroblasts have also been shown to have osteogenic potential, especially human derived dermal and gingival fibroblasts [35]. This was verified in a study that showed osteogenic differentiation of human fibroblasts in the presence of BMPs on a tricalcium phosphate porous scaffold [36]. Also, studies have been developing the idea of using BMPs in human studies. BMPs are proven to induce bone formation and osteogenic differentiation in animal models, but human studies show a lack of bone formation except in very large and sustained release. They also have very little effect on non-union fractures. In contrast, parathyroid hormone treatments have been shown to enhance bone regeneration in humans. This is thought to act through the upregulation of Wnt proteins and IGFs [37].

The microenvironments in which stem cells and progenitor cells reside is called a niche. The niches are composed of nanofibrous extracellular matrix proteins, including collagens, elastins and others. One of the main focuses of fabricated tissue scaffolds is biomimetic properties, and one of those properties is mimicking this nanofiber structure. Fiber formation techniques have emerged in the form of electrospinning, self-assembly and phase separation. The goal is to create an environment that makes the cell feel at "home," and emulate this niche and its components. Structure and mechanics are shown to be two of the main causes to induce cellular instructions, like differentiation or proliferation [23].

The periosteum lines the entire cortical bone surface throughout the body. Many of the biochemical cues and mechanical stimuli to drive cell migration and differentiation of osteoprogenitor cells residing there come from cortical bone. The main constituents leading to periosteal activity are the vascularization of cortical bone during formation and remodeling, electrochemical signaling that occurs between periosteum and cortical bone and blood circulation/oxygen tension that occurs in the vessels found in cortical bone. Oxygen tension plays a role in periosteal cell differentiation to either a chondrogenic or osteogenic lineage. At 10-15% oxygen levels, chondrogenesis is at its highest, where significantly low or high levels (less than 5% or greater than 90%) lead to chondrogenic hypertrophy and the induction of osteogenesis [22] Physical properties, such as elasticity, tensile strength, toughness, etc. also induce changes in bone patterning and morphogenesis during development, and these cues also aid in repair and remodeling [21].

All of these studies have paved the way to exploring how engineered constructs mimicking and integrating with periosteum can lead to appropriate bone formation in critical sized defects. Although the main focus of bone repair now is either autografts or replacement materials, a shift to regeneration has become the focus over the past decade. To these means, cellular infiltration and interaction becomes of upmost important and specific properties of recruiting cells from the host tissue to migrate into the tissue, suppressing immunorejection and mimicking the ECM to promote cell attachment and functionality.

Chapter 3. **Chitosan as a Biopolymer for Tissue Engineering**

Chitin is a naturally occurring polysaccharide found in the form of crystalline microfibrils that form the structural components of the exoskeleton of crustaceans. It is also included in the cell walls of fungi and yeast as well as other organisms that utilize the strength and reinforcement of chitin [5, 38, 39]. Chitin is the world's second most abundant polymer after only cellulose. Chitin's chemical structure is very similar to cellulose with the only difference being the hydroxyl at the C2 position of cellulose is replaced by an acetamido group in chitin (Figure 8) [5].

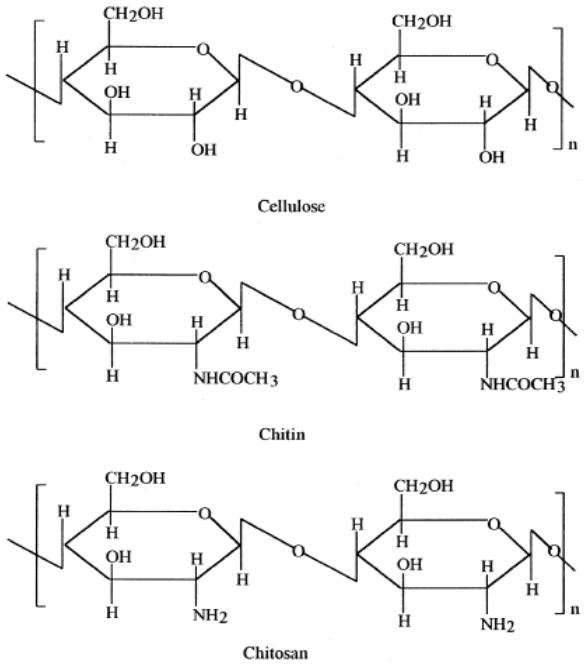

Figure 8. Molecular structure of cellulose, chitin and chitosan. Notice the close similarity between chitin and cellulose only replacing the ethyl group on the C2 carbon with an acetamido group. Further, deacetylating chitin yields the usable biopolymer chitosan, applicable in many areas of tissue engineering [5].

The most common source of chitin is from the waste generated by shrimp and crab processing facilities. Chitin can be extracted through a process that includes the addition of hydrochloric acid to dissolve calcium carbonate from exoskeletons followed by an alkaline treatment to remove proteins. Chitin can be further processed to form chitosan, its most versatile derivative used for agricultural purposes [40], filtration [41], industrial uses [42] and biomedical applications [43-50], by using an alkaline treatment to partially deacetylate chitin [51]. However, deacetylation will almost never proceed to 100% completion (95% is considered the maximum) and the polymer chain is expected to degrade significantly if it is exposed to these strong alkaline treatments for extended periods of time. It is generally accepted that a polymer with greater than 70% deacetylation be considered chitosan [52].

In terms of bone tissue engineering, chitosan is an attractive biomaterial due to its enhanced mechanical properties when modified or crosslinked. Use of chitosan may help to overcome problems such as stress shielding that occurs with metallic bone implants. Stress shielding occurs when the implant removes the entire mechanical load from the bone [53]. Bone is known to regenerate and remodel itself as load is applied, so when a metal implant takes on the entire load that is applied in everyday motion, the bone no longer remodels and repairs itself, which leads to degradation and deterioration [53]. Chitosan can be blended with ceramics similar to that found in bone tissue, like hydroxyapatite or tricalcium phosphate, to mimic the mechanical properties and bioactivity of natural bone [50, 54, 55]. Mineralized chitosan scaffolds can be implanted into bone tissue, with the aid of a cast to keep the bone set in place, to begin self-regeneration. Not only would mineralized chitosan scaffold more closely mimic natural

bone better than metal (Figure 9), but these scaffolds will also have a much more similar fracture toughness then metal replacements [1].

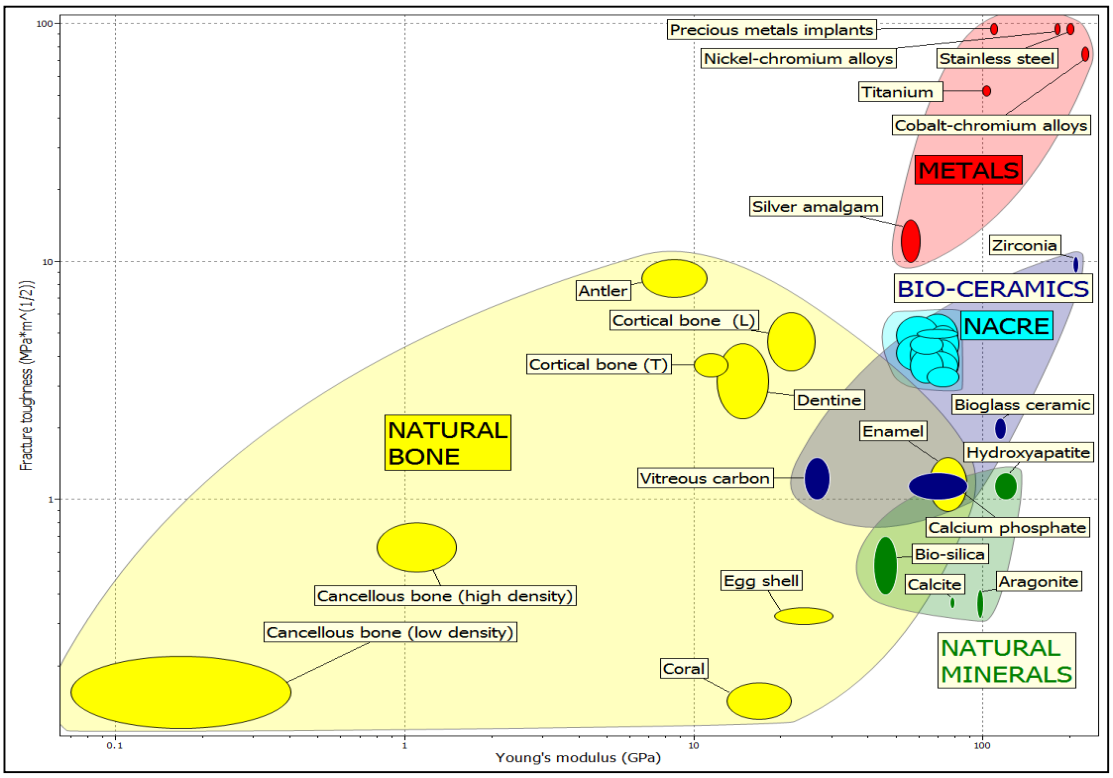

Figure 9. The fracture toughness for a composite of chitosan and natural mineral, like hydroxyapatite, would much more closely mimic the ECM of natural bone tissue over metal implants. This is a novel concept for developing new and improved bone replacement biomaterials. [1]

For applications in non-load bearing bones, structural integrity and support are less of a requirement and there is more of a focus towards regenerative capacity. Scaffold fabrication techniques such as electrospinning offer an ideal, platform technology to act as a template to promote tissue integration from the host. Electrospinning is a promising method for scaffold fabrication due to the structural resemblance of the fibers of the electrospun matrix to the natural fibrous ECM of bone [54]. Electrospinning involves extruding a polymeric solution through a charged syringe

tip and gathering the polymer fibers on a collector [56]. Co-electrospinning involves the electrospinning of two different types of polymers, a polymer together with microspheres or nanoparticles, or a polymer/composite solution containing an inorganic material [57, 58][59]. Recent approaches address the possibility of co-electrospinning chitosan with other materials to generate biocomposite scaffolds for bone tissue engineering and emulate the composition and nanostructure of the bone [59-62].

A challenge in fabricating bone tissue scaffolds for weight bearing bones is obtaining enough mechanical strength (tensile modulus of 10GPa) [63]. However, when dealing with non-load bearing bones, such as craniofacial or other flat bones, the scaffolds will rather mend and regenerate the wounds instead of providing load-bearing support. Thus, our goal was to create a patch for craniofacial defects mimicking the mechanics of the periosteal bone with a tensile modulus ~ 120MPa. [64]. This is still a rather high range for as-spun natural nanofibers, which is usually in the range of 75MPa for electrospun chitosan [60], so crosslinking is needed to enhance the mechanical properties of the base material.

There are many techniques including physical, enzymatic and chemical crosslinking methods to enhance the mechanical properties of bio-polymers to match those of bone [65-67]. Genipin is a natural, non-toxic crosslinker derived from the fruit of gardenia extracts. It binds to the free, outer amine groups of a chitosan polymer chain, forming new bonds between the fibers and leading to an increases in mechanical strength [68].

Another challenge with electrospun scaffolds is the limited pore size that is generated due to the densely packing of fibers during the electrospinning process. These scaffolds do contain interconnected pores throughout, which generate a relatively high porosity; however there is limited ability for the cells to infiltrate the scaffolds due to a lack of adequate pore size [69]. A number of methods have been employed to increase pore sizes in electrospun scaffolds. One promising technique is the incorporation of sacrificial fibers that can be removed post-spinning [69-71], which in turn leads to the creation of larger pore sizes in the scaffolds, enhanced cell migration into the scaffolds and eventually to osseointegration of the bone scaffolds *in vivo*. Although crosslinking CTS with GP has been proposed to increase the stiffness of hydrogels used for soft tissue engineering [72], this approach has been considered only recently for bone engineering [73, 74] and was not reported for CTS-HA composite scaffolds until the studies presented here [50].

The versatility and biocompatibility of chitosan offer a set of unique and promising capabilities for developing appropriate scaffolds for bone tissue engineering. This thesis adds some new results and information to the overall goal of engineering suitable, biomimetic scaffolds that are capable of promoting cell growth and viability while integrating host tissue infiltration and inducing self-regeneration and natural healing rather than replacement.

Chapter 4. **Materials and Methods**

4.1 Materials

Medium molecular weight chitosan (CTS, 75% - 85% deacetylated), trifluoroacetic acid (TFA, ≥98%), and hydroxyapatite (HA, reagent grade, <200 nm nanoparticles), 1,1,1,3,3,3-Hexafluoro-2-propanol (HFP), ascorbate-2-phosphate, β-glycerosphosphate, ferric chloride, Beibrich's Scarlet, Acid Fuchin, phosphomolybolic acid and phosphotungstic acid were purchased from Sigma-Aldrich Co. Ltd. (St. Louis, MO). Hematoxylin, eosin Y, 37% formaldehyde, hydrochloric acid (HCl), aniline blue and Permount were purchased from Fisher Scientific (Kalamazoo, MI). Picric acid was purchased from EMS (Hatfield, PA). Genipin (GP, ≥ 98% pure) was purchased from Wako Pure Chemical Industries Ltd. (Osaka, Japan). Ultrapure bovine gelatin was purchased from HiMedia (Mumbai, India). Glacial acetic acid was purchased from Amresco (Solon, OH). Ethyl acetate was purchased from EMD (Billerica, MA). Poly-lactic-co-glycolic acid (PLGA, 90:10 L:G ratio) was provided courtesy of Changchun Institute of Applied Chemistry, Chinese Academy of Science, P.R. China. 1,1′-Dioctadecyl-3,3,3′,3′-tetramethylindocarbocyanine perchlorate (DiI) and 3,3′-Dioctadecyloxacarbocyanine perchlorate (DiO) fluorescent dyes were provided courtesy of Dr. Alan Waggoner from Carnegie Mellon University (Pittsburgh, PA). The alamar blue colorimetric assay kit was purchased from AbD Serotec (Raleigh, NC). The alkaline phosphatase colorimetric assay was purchased from Abcam (Cambridge, MA). All PCR kits and master mixes were purchased from Qiagen (Valencia, CA) and all primers from Applied Biosystems (Carlsbad, CA). Mouse mesenchymal stem cells (moMSC) and green fluorescent protein tagged moMSC (GFP moMSC) were provided courtesy of a

material transfer agreement from the University of Texas A&M. Dexamethasone was purchased from Alfa Aesar (Ward Hill, MA). Xylene was purchased from VWR Laboratories (West Chester, PA). CD-1 strain female mice (-30g) were purchased from The Jackson Laboratory (Bar Harbor, ME). All surgical supplies were purchased from PennVet (Lancaster, PA). Trephines (2.1mm diameter) were purchased from Fine Science Tools (Foster City, CA).

4.2 Fabrication of Electrospun and Modified Chitosan Scaffolds

4.2.1 Electrospinning

CTS and HA-containing CTS scaffolds were electrospun from a solution of CTS dissolved in TFA to yield 7% (w/v) CTS. HA-containing scaffolds were generated by admixing 0.8%, 1.0% or 2.0% HA nanoparticles (w/v) to the CTS solution. All solutions were stirred at room temperature for at least 5 days. Electrospinning was performed in a homemade system, essentially as previously described [75, 76]. In brief, 5 mL glass syringes (BD, multifit syringes) containing 4 ml each of the above solutions were mounted in a KDS200 syringe pump (KD Scientific). The flow rate was set to 1.2 ml/hr. A voltage of 15 kV between the syringe tip and the target, generated by an ES-30 Gamma High Voltage Research power supply (Gamma High Voltage Research), was applied by connecting the cathode to the syringe needle and the anode to a rectangular 6 × 2 cm aluminum collecting plate placed 15 cm from the tip of the needle.

4.2.2 Crosslinking

Electrospun scaffolds were crosslinked with 0.1 % (w/v) GP. The scaffolds were first stabilized ("waterproofed") by soaking them for 20 minutes in 0.5% sodium hydroxide (NaOH) dissolved in 100% ethanol, followed by five 30 second washes with 1X phosphate buffer solution (PBS) to remove any trace amounts of ethanol [77]. The stabilized scaffolds were then crosslinked in 0.1% (w/v) genipin dissolved in 1X PBS for 24 hours. The crosslinking process was terminated by washing the scaffolds in PBS, as described above. The resulting scaffolds were termed chitosan-genipin crosslinked scaffolds (CTS-GP) or chitosan-hydroxyapatite-genipin crosslinked composite scaffolds (CTS-HA-GP).

4.3 Scaffold Characterization

4.3.1 Scanning Electron Microscopy

For ultrastructural analysis, circular scaffold samples of 10.3 mm diameter were sputter coated with carbon for about 30 seconds. The samples were viewed and digitally photographed in a Zeiss Supra50VP field emission scanning electron microscope (FESEM) equipped with an Oxford Instruments INCA Energy Dispersive Spectrometer at 5 kV with the SE2 detector using a 30 µm final aperture.

4.3.2 Electron Dispersive X-ray Spectroscopy (EDS)

An FESEM equipped with an EDAX electron dispersive X-ray spectroscopy system was used to assess calcium and phosphorous contents of the scaffolds. X-ray spectra were taken at 10 kV using a 60 µm final aperture. EDS was performed using the FESEM at an acceleration voltage of 10 kV.

4.3.3 X-ray Diffraction (XRD)

XRD was performed using a Siemens D500 powder diffractometer using conventional Bragg–Brentano geometry in q – 2q configuration, with Cu_{Ka} source (l = 0.154 nm). 2q scans were acquired from 10 – 60^0 with a step of 0.03^0 and 1s dwell time per point.

4.3.4 Fourier Transform Infrared Spectroscopy (FTIR)

FTIR spectra were collected on a Varian Inc. FTS3000 Excalibur FTIR spectrometer equipped with a Deuterated Triglycine Sulfate (DTGS) detector and KBr beam splitter. The spectra were recorded at resolution of $4cm^{-1}$ in transmission mode.

4.3.5 Mechanical Properties

The mechanical properties of the scaffolds were tested using the Instron 5564 Table Mounted Materials Testing System and Merlin Series IX software (Instron, Norwood, MA). Hydrated CTS-GP and CTS-HA-GP scaffolds were cut into strips of 22.7 ± 2.3 mm x 5.4 ± 0.7 mm (n = 28). Samples were prepared by either waterproofing CTS-HA-GP scaffolds and then washing 5 times in 1X PBS or by waterproofing followed by crosslinking in 0.1% GP for 24 hours and then washing 5 times with 1X PBS. All samples were stored in 100 mm petri dishes containing 1X PBS until testing. To simulate a “biologic” environment, samples were tested under wet conditions immediately upon removal from the PBS. A gauge length of 10 mm was used for all samples. The strain rate was set at 1 mm/min. The Young’s modulus was calculated from the linear portion of stress-strain curves. The ultimate tensile strength (UTS) was determined by calculating

the stress at break normalized to the cross-sectional area of the scaffold. The measured average thickness of the scaffolds was 25.3 ± 16.2 μm (n = 28).

4.4 Osteocompatibility

4.4.1 Cell Culture

Murine 7F2 osteoblast-like cells were obtained from ATCC and cultured in alpha modification of Minimum Essential Medium (α-MEM) containing 1 g/L glucose, 10% fetal bovine serum (FBS), 2 mM L-glutamine, 1% (v/v) penicillin-streptomycin. Cells were placed in T-25 cell culture flasks in an incubator set to 37ºC and 5% carbon dioxide. The medium was changed every second day. The cells were passaged at a 1:3 ratio and expanded three times by trypsinization prior to seeding onto the scaffolds, as described below.

4.4.2 Seeding of 7F2 cells on scaffolds

Circular scaffolds with a diameter of 10.3 mm, cut from either the CTS-HA-GP (1.0% HA) or CTS-GP electrospun sheets, were placed in 24 well plates, secured with a Viton O-ring [78], stabilized, and crosslinked with 0.1% GP, as described above. The samples were sterilized with UV light for one hour and pre-treated by soaking in complete medium overnight. 7F2 cells were seeded in aliquots of 50 μl containing 10,000 cells by carefully pipetting onto the center of the scaffold. The cell–seeded scaffolds were then placed into an incubator for one hour. After this time period, 450 μL of medium consisting of low glucose (1 g/L) α-MEM, 10% FBS, 2mM L-glutamine and 1% (v/v) penicillin-streptomycin was added to each well. The cells were cultured for up to 21 days

during which time the medium was changed every other day. Cells were also cultured in a similar manner on tissue culture polystyrene (TCP) as a negative control.

4.4.3 Cell Morphology

To evaluate the morphology of cells growing on the scaffolds, samples were fixed on days 7, 14 or 21 post-seeding, as above, and serially dehydrated in ethanol and hexamethyldisilazane (HMDS) for 10 minutes in each concentration as previously described [79]. The samples were left to air dry in a chemical fume hood overnight at room temperature, sputter coated with carbon, and observed under SEM, as described above. Attempts at critical point drying the samples were abandoned, since CPD significantly reduced the sizes of the scaffold to a point that they were unusable.

4.4.4 Cell Viability and Proliferation

Cell viability and proliferation were continually monitored over a 21 day period using the continual alamarBlue™ (AB) assay on days 0, 3, 7, 14 and 21 as previously described [80]. In brief, 7F2 cells were seeded in 24 well plates onto TCP as well as onto circular CTS-GP and CTS-HA-GP scaffolds at a density of 3.5×10^4 cells/well. At the time points stated above, AB was added at 10% (v/v) in triplicate to each well. The plates were then returned to the incubator for three hours. For zero control, AB was also either added to wells containing only medium or scaffolds and media. After 3 hours, 200 µl aliquots of the supernatant were pipetted in triplicate into 96 well plates and the AB fluorescence was read in a Synergy 4 microplate reader (Biotek, Winooski, VT) at an excitation wavelength of 545 nm and an emission wavelength of 590 nm. The data were analyzed using Gen5 software (Biotek) and samples were normalized to their respective zero

controls. The cells were re-fed with fresh medium and placed in the incubator to be analyzed at the next time point.

4.4.5 Alkaline Phosphatase (ALP) assay

ALP is an early marker for differentiation towards the osteocytic phenotype [60]. Murine 7F2 osteoblast-like cells were seeded, on TCP, CTS-GP and CTS-HA-GP scaffolds in 24 well plates at a density of 3.5×10^4 cells/well. ALP activity was measured colorimetrically on days 0, 7, 14 and 21 using a commercial kit (Abcam, ab83369). At each time point, three cell-seeded scaffolds were homogenized in a glass tube homogenizer containing 300 μL of lysis buffer (kit component). The supernatant was collected and centrifuged at 1350 rpm for 3 minutes to remove all insoluble debris. 30 μL aliquots of the resultant samples were added to a 96 well plate followed by 50 μL of assay buffer and 50 μL of *para*-Nitrophenylphosphate (pNPP) solution. Following incubation for one hour at room temperature, 20 μL of stop buffer was added to the samples and the absorbance was read in the microplate reader at 420 nm, as described above. To assess the ALP activity of control cells growing on TCP, the wells were rinsed with 300 μL of 1X PBS, followed by addition of 1X lysis buffer for 10 minutes. After that, the supernatant was collected and cell remnants were scraped with a cell scraper for manual lysis. The protocol for analyzing ALP activity was then followed, as above.

4.4.6 RNA Isolation and quantitative real time RT-PCR

7F2 cells were trypsinized after 7, 14 or 21 days of culture on TCP, CTS-GP and CTS-HA-GP scaffolds. The cells were pelleted by centrifugation at 800 RPM for 5 minutes. After a 1X PBS wash, the resulting pellet was stored at -80 °C prior to RNA

isolation. A Qiagen RNeasy Mini Kit was used to isolate RNA by columnar centrifugation and DNase digestion, as per the manufacturer's instructions. RNA integrity was initially determined by electrophoresis on 1.0% agarose gels. Quantitative real-time reverse transcription polymerase chain reaction (qRT-PCR) was performed with a Qiagen One-Step Kit combined with TaqMan expression assays according to the manufacturer's instructions. qRT-PCR was performed using a Realplex II thermal cycler (Eppendorf, Hamburg, Germany) using the following Taqman primers (from Applied Biosystems, Carlsbad, CA): Spock (Osteonectin, Mm00486393_m1), Alkaline Phosphatase (Mm01187115_m1), Spp1 (Osteopontin, Mm00436767_m1). GAPDH (Hs99999905_m1) was used as an internal 'housekeeping' control. Primer efficiency was determined by linear regression of a dilution series. Cycle threshold (CT) results were analyzed by the Pfaffl Method. The results were normalized to TCP and GAPDH prior to logarithmic transformation [81]. Each experimental condition and gene primer was analyzed in triplicate.

4.5 Osteoinductive Capacity of Scaffolds

4.5.1 Cell Culture

Murine (mouse) Mesenchymal Stem Cells (moMSCs) were obtained from the University of Texas A&M Health Science Center College of Medicine Institute for Regenerative Medicine headed by Dr. Darwin Prokop. This facility was recently given NIH funding to provide high quality human, mouse and rat mesenchymal stromal cells to researchers (See: http://medicine.tamhsc.edu/irm/msc-distribution.html). These cells were expanded in Iscove's Modified Dulbecco's Medium (IMDM) containing 1g/L

glucose and supplemented with 10% FBS + 10% horse serum (HS), 2mM L-glutamine and 2% antibiotic-antimitotic (ABAM). Cells were placed in T-25 cell culture flasks in an incubator set to 37ºC and 5% carbon dioxide. The medium was changed every third day. The cells were passaged three times by trypsinization prior to seeding on the scaffolds.

4.5.2 Seeding of moMSC on Scaffolds

Circular scaffolds with a diameter of 10.3 mm, cut from either the CTS-HA-GP (1.0% HA) or CTS-GP electrospun sheets, were placed in 24 well plates, secured with a Viton O-ring [78], stabilized, and crosslinked with 0.1% GP, as described above. The samples were sterilized using 10% ABAM overnight and then subsequently washed 3 times with DI water. The scaffolds were acclimated with medium by soaking in complete IMDM overnight. The moMSC were seeded in aliquots of 50 µl containing either 100,000 cells (low density) or 500,000 cells (high density) by carefully pipetting onto the center of the scaffold. The cell–seeded scaffolds were then placed into an incubator for one hour. After this time period, 450 µL of complete IMDM or osteogenic medium, which was complete IMDM medium containing 100nM dexamethasone, 200µM ascorbate-2-phosphate and 10mM β-glycerophosphate was added to each well in accordance to experimental conditions. The cells were cultured for up to 21 days during which time the medium was changed every third day. Cells were also cultured in a similar manner on tissue culture polystyrene (TCP) as a negative control.

4.5.3 Stem Cell Viability, Metabolic Activity and Proliferation

Viability and metabolic activity indicating proliferation of moMSCs was maintained using AB assays at days 1, 4, 7, 14 and 21 according to the same protocol as stated previously in section 2.5.4. The moMSC were seeded at densities of 500,000 cells per well on TCP, 10mm CTS-GP scaffolds and 10mm CTS-HA-GP scaffolds and cultured for the said time points in either IMDM or osteogenic medium. Fluorescent readings were recorded using the Syngergy4 microplate reader.

4.5.4 Cell Morphology

Cell morphology was observed using fluorescent microscope imaging DAPI/phalloidin staining at days 7, 14 and 21 to show cell survival over the 3 week time period and observe cellular morphology of moMSC grown on CTS-GP and CTS-HA-GP scaffolds and compared to moMSC cultured on TCP. Briefly, scaffolds were fixed in 10% formalin at the above mentioned time points for 20 minutes followed by subsequent washing with DI water and 60mM glycine to remove excess aldehyde groups. The fixed cells were permeabilized in 0.5% Triton-X 100 for 20 minutes and then washed in 3 washes of immunofluorescent (IF) wash containing 130mM NaCl, 7mM Na_2HPO_4, 3.5mM $Na_2H_2PO_4$, 7.7mM NaN_3, 0.1% bovine serum albumin (BSA), 0.2% Triton-X 100 and 0.05% Tween-20 in DI water for 10 minutes each. This was followed by blocking in IF wash + 10% goat serum (primary blocker) for 1 hour. Finally, cells were washed with a secondary blocker containing primary blocker + 1:100 dilution of antigen binding fragment 2 [$F(Ab)_2$] containing 5μg/mL DAPI and a 1:1000 dilution of green phalloidin. Although immuno-washes are generally not required for simple nuclear/cytoskeletal staining, genipin has a very high autofluorescent property and this wash reduced this and

enhanced imaging. Cells fluoresced blue nuclei (DAPI) and green cytoskeleton (phalloidin).

MSC-scaffold interaction was observed at days 7, 14 and 21 also via SEM to observe cell attachment and cell spreading characteristics on scaffold surfaces. SEM images were taken according to the same protocol as discussed above in section 2.5.3.

4.5.5 Alkaline Phosphatase Activity

ALP activity was observed in the moMSC cultured on CTS-GP and CTS-HA-GP scaffolds on days 7, 14 and 21. Scaffolds were collected from samples cultured in IMDM and in osteogenic medium, ALP activity was assayed as described above (see section 4.4.5).

4.6 Osteoconductive Capacity

4.6.1 Scaffold Preparation for In Vivo Implantation

CTS-GP and CTS-HA-GP scaffolds were cut into 10mm circular scaffolds and fitted into 24 well plates using Viton O-rings. The scaffolds were sterilized in 10% ABAM overnight and subsequently washed three times with DI water and acclimated with IMDM medium overnight.

GFPmoMSC were provided by the University of Texas A&M. GFP tagged cells are useful for tracking cells during *in vivo* implants during the surgery to observe cell viability in the body. The cells were cultured in complete IMDM in T-cell culture flasks and expanded 2 passages. They were then seeded onto the prepared scaffolds at a seeding density of 100,000 cells/scaffold. Scaffolds were then prepared for implantation

and divided into sub-groups of CTS-GP without moMSCs, CTS-GP with moMSCs, CTS-HA-GP without moMSCs and CTS-HA-GP with moMSCs. Scaffolds that were seeded with cells were seeded 3 days prior to implanting to allow appropriate cell attachment and initial cell interaction with the scaffold. From the designated samples above, 2.5mm circular specimens were cut from each sample and used as the implant scaffolds.

4.6.2 Animal Model and Scaffold Implantation

CD1 female mice weighing about 30g were obtained from Jackson Laboratories as the appropriate model for observing bone regeneration in a calvarial defect. Mice were housed in cages containing an adequate food and water supply, monitored daily and at a population of no more than 5 mice per cage. Cages were cleaned daily and changed out once a week. All caretaking, surgical procedures and post-operative care were in accordance with an IACUC-approved protocol. All mice were allowed to become acclimatize with their new environments before any surgical procedures were performed.

For implantation, scaffolds were cut from the 10mm scaffolds into 2.5mm samples. Each sample was removed from a separate scaffold of its sub-type (noted above) to obtain results from individual scaffolds for all time points. Scaffolds not seeded with cells were placed into a Petri dish containing 1X PBS with calcium and magnesium and brought into the surgical room. Scaffolds with cells were placed into individual petri dishes and stored in the incubator until right until the surgical procedures. In between mice, a new scaffold would be retrieved and brought into the surgical room.

Before beginning surgery, mice were placed into an isofluorane chamber for 15 minutes for initial anesthesia preparation. After, the mice were fitted into a stereotaxic

setup fitted with a surgical gas mask pumping isofluorane to maintain proper anesthesia. A tooth bar was used to position the mouse's head straight while the gas mask was fitted. Ear bars were then inserted into the zygomatic arch of each ear to maintain stereotaxic stability throughout the duration of the surgery. 0.25mL of ketoprofen was given as a subcutaneous shot as an anti-inflammatory prior to surgery as well as 24 hours post-surgery. Optical lube was used to maintain moisture in the eyes and avoid cataract formation due to over-drying of the eyes during surgery. The top of the cranium was shaved and swabbed with betadine to prevent outside infection during surgery. An incision was made in the proximal to distal direction across the surface of the cranium and hemostat clamps were used to peel the skin laterally to expose the calvaria. Sterile saline solution was used to keep the skull moist while exposed and also to reduce the burning effect the drill may have on bone tissue. A 2.1mm trephine equipped to a drill controlled by a foot petal was used to remove two sections from either lateral side of the midline of the skull. One of these holes was left empty as a blank control while the other was fitted with one of the scaffold sub-sets mentioned above in section 4.6.1. A small amount (the dab of a pin) of Vetbond (3M, St. Paul, MN) surgical glue was used to secure the scaffold in place. The incision was then stitched closed using 6-0 surgical sutures and further secured using Vetbond. The Vetbond also acted as a barrier between the mice's grooming of the wound and the scaffold, prominently prevent scaffold destruction due to repeated scratching. Upon completion of the surgery, each mouse was removed from the stereotaxic equipment and placed back into the cage. Scaffolds were retrieved at 1 month, 2 months and 3 months from individual mice (n= 4 for each group) to assess calvarial regeneration over the course of time.

4.6.3 Harvesting of Tissue

At the predetermined time points mice were euthanized using 0.1ml of Beuthanasia solution via IP injection. The mice were placed into an isofluorane chamber, anesthetized and then given the IP injection. Euthanasia was considered complete once the mouse stopped breathing. The mice were decapitated with sheers and skulls were harvested by complete removal of the skin from the head. Harvested skulls were placed in 10% formalin in 4^{o}C overnight for fixation and then stored in 1X PBS until analysis.

4.6.4 MicroCT Imaging and Fracture Area Measurements

MicroCT imaging was used to observe new bone formation and to determine the density of new tissue formed. Samples for imaging were prepared at the specified time points of 1, 2 and 3 months. The animals were euthanized by IP injection of a 0.25mL Beauthanasia following 10 minutes in an isofluorane chamber. After euthanasia, the animals head was immediately removed, skinned and placed into a 10% formalin solution overnight. After, the remaining soft tissue, including remaining skin and muscle, tongue, brain and eyes are completely removed, leaving just the skull. A μCT-50 scanner (Scanco Medical, Wayne, PA) housed at the University of Pennsylvania was used for imaging the samples. The scanner was operated at an X-ray energy/intensity of 70kVp, 114μA and 8W with a medium resolution. A scout view reading from 0 – 145mm and angle of 90^{o} as a rough scan of the whole skull to determine the appropriate region of interest (ROI). A field of view (FOV) diameter of 38.9mm and a voxel size of 38μm with an integration time of 200ms were used as typical scanning parameters. The number of scans (slices) was 211/8.02mm. Along with imaging, fracture area measurements were recorded. By selecting the specific ROI where the bone scaffold was implanted, a

measurement of the area of calcified tissue was obtained and analyzed using Axiovision Imaging Software. The area of all sample sub-sets was analyzed and recorded as a percentage relative to defect without scaffold and compared between CTS-GP, CTS-HA-GP and defects with no scaffold.

4.6.5 Histological Staining for Bone Formation

The organization of new bone tissue formation can be evaluated histologically, using hematoxylin and eosin (H&E) and Masson's Trichrome staining. After taking the MicroCT images, fixed samples were decalcified in a decalcification solution containing 90% water, 10% HCl and trace amounts of sodium tartrate dehydrate, potassium sodium tartrate tetrahydrate, and EDTA (Protocol Decalcification Solution B, Fisher Scientific, Pittsburgh, PA) for 10 days until samples bone loses its rigid texture and becomes softer and more pliable. After decalcification, the calvaria, or top portion of the skull, was removed from the rest of the skull by cutting with scissors, serially dehydrated using ethanol dilutions (30-100%) followed by xylene dilutions (50:50 xylene ethanol then twice in 100% xylene) for 15 minutes each and finally embedded in paraffin. Once embedded, samples are put in the freezer overnight. Frozen samples are then sectioned using a Leica microtome into 5μm thick slices. Slices were placed in a warm water bath and then mounted onto lysine coated microscope slides and allowed to dry overnight.

For routine H&E staining tissue sections were deparaffinized and rehydrated through a serial xylene/ethanol/water rehydration procedure and then stained with hematoxylin for 4 minutes, dipped in water until there was no more hematoxylin bleeding off, rinsed

in 1% acid alcohol, stained with eosin for 2 minutes, washed in water, quickly dehydrated and mounted using Permount.

Masson's Trichrome staining is used to illustrate the organization of newly formed tissue around the injury site. Briefly, rehydrated tissue sections were fixed in Bouin's solution for 1h at 56ºC. After fixation, sections were washed with running tap water for 5min and stained in Weigert's hematoxylin working solution for 10min. This is followed by washing in running tap water for 10min and then 2 washes of distilled water. Next, samples are stained in Biebrich Scarlet-acid fuchin for 10min and then washed in distilled water until the bleeding stops. Then, the samples are differentiated in phopshomolybolic-phosphotungstic acid solution for 12min and then analine blue solution for 5min. Finally, samples are rinsed two times in distilled tap water, differentiated in 1% acetic acid solution, washed twice in distilled water and quickly dehydrated through an ethanol/xylene serial dilution and mounted with Permount. The ingredients for Masson's Trichrome Staining can be seen below in Table 1.

Table 1. List of solution for Masson's Trichrome staining protocol.

Solution	Ingredients
Bouin's Solution	75mL picric acid, 25mL formaldehyde, 5mL glacial acetic acid
Weigert's Iron Hematoxylin Solution A	1g hematoxylin, 10mL 95% ethanol
Weigert's Iron Hematoxylin Solution B	4mL 29% ferric chloride, 95mL distilled water, 1mL concentrated HCl
Weigert's Iron Hematoxylin Working Solution	Equal Parts solution A and solution B
Biebrich Scarlet – Acid Fuchin Solution	90mL Biebrich Scarlet, 10mL acid fuchin, 1mL glacial acetic acid
Phosphomolybolic-Phosphotungstic Acid Solution	25mL 5% phosphopolymolic acid, 25mL 5% phosphotungstic acid
Aniline Blue Solution	2.5g aniline blue, 2mL glacial acetic acid, 100mL distilled water
1% Acetic Acid Solution	1mL glacial acetic acid, 99mL distilled water

4.7 Enhanced Porosity of Electrospun Scaffolding Material

4.7.1 Fabrication of Dual Electrospun PLGA/Gelatin Scaffolds

PLGA scaffolds were electrospun from a solution of 10% PLGA dissolved in HFP. Gelatin solutions were prepared at 5%, 15% and 20% gelatin dissolved in a 3:2:1 ratio of acetic acid, ethyl acetate and water respectively. A homemade dual spinning system was set up by placing a rotating aluminum collector in between 2 syringe pumps (One pump was the KDS200 and the other was Chemyx Fusion 100 syringe pump [Chemyx, Stafford, TX]). The KDS200 has a metal casing, which proved to interfere substantially with gelatin, attracting most of the fibers to the wall of the pump rather than allowing

appropriate collection on the collector. This was not seen to have as high an effect on the PLGA solutions, so the PLGA was loaded into the KDS200 while the gelatin into the Fusion 100, which has a plastic casing. Two high voltage supplies were used to generate the field between each pump and the collector. The collector was attached to a Series 2224 Faulhaber DC-micromotor fitted with a Series 22E Faulhaber gearhead (MicroMo, Clearwater, FL) with a 19:1 differential ratio. The collector was rotated at ~30RPM when a voltage of 6V was applied. The spinning parameters for PLGA were 1.0mL/h, 15kV and 12cm and for gelatin were 1.0mL/h, 15kV and 15cm and a 1:1 ratio of each solution was used, i.e. 5mL of each solution. Scaffolds were removed from the collector by cutting one side with a razor and pealing the material off of the collector. Pure PLGA scaffolds were collected as-spun and prepared for tests accordingly. The composite PLGA/gelatin scaffolds containing 5%, 15% or 20% gelatin were then soaked in 3 washes of water for 5 minutes each to ensure removal of gelatin from the scaffolds. Once removed, scaffolds were prepared for tests accordingly.

4.7.2 Analysis of Fiber Removal and Fiber Morphology

While preparing the solutions as stated in section 4.7.1, the two lipophilic carbocyanine dyes 3,3'-Dioctadecyloxacarbocyanine Perchlorate ($DiOC_{18}$) and 1,1'-Dioctadecyl-3,3,3',3'-Tetramethylindocarbocyanine Perchlorate ($DiIC_{18}$) [69] were added at a volume of 10μg/mL to gelatin and PLGA solutions respectively. These lipophilic membrane dyes are often used to stain cell membranes and are lightly fluorescent in solution, but enhanced fluorescence is observed when bound to a cell membrane. However, previous studies have shown that these dyes are also capable of binding fibers as well [69]. So, these dyes were used to generate green (DiO) fluorescent gelatin fibers

and red (DiI) fluorescent PLGA fibers, which then could be distinguished in a fluorescent microscope. Images were obtained using an Olympus FSX100 microscopy system. Images were obtained prior to removing gelatin fibers, after removing gelatin fibers and of PLGA scaffolds not containing gelatin.

Further, SEM analysis was used to observe the morphology of fibers before and after gelatin removal. The procedure for SEM analysis can be found above in section 4.3.1. Since these samples were required to soak in water to remove gelatin, a dehydration of these scaffolds was necessary for imaging. The dehydration procedure can be found above in section 4.4.3. For pure PLGA scaffolds, no dehydration was necessary. For both fluorescent microscopy and SEM analysis, samples containing 0%, 5%, 15% and 20% gelatin were observed.

4.7.3 Mechanical Testing

Mechanical testing of the scaffolds was performed using the Bose Electroforce material testing system (MTS) and the Wintest 7 software from Bose (Eden Prairie, MN). Samples of PLGA scaffolds containing 0%, 5%, 15% and 20% gelatin were prepared by cutting 20×5mm strips with thicknesses of 54±31μm measured using manual calipers. Strips were then soaked in 3 washes of water for 5 minutes each to remove gelatin. All samples were then stored wet in small amounts of water in petri dishes. Strips were loaded into the Bose grips while wet and were subject to tensile testing at a strain rate of 0.5mm/sec until failure. The load cell had a sensitivity of 22N. From the data obtained, stress strain curves were generated and the elastic region was used to determine the Young's moduli and ultimate tensile strength of the samples.

4.7.4 Modeling Cell Proliferation on Porous Electrospun Scaffolds

Predictive modeling can be used to show how cells should penetrate a scaffold based on different pore sizes induced by different concentrations of gelatin incorporation. The detailed model can be found in Chapter 7. MatLab software was used to generate descriptive code to create a mathematical model depicting behavior in a scaffold in terms of cell proliferation, ECM production and available space in the scaffold, as the cells proliferate and deposit their ECM.

To validate the model, cells were seeded on scaffolds according to the procedure in section 2.7.4. Cell viability and proliferation were monitored using the alamar blue assays over a 1 week period at days 1, 2, 3, 4 and 7. The detailed procedure for AB assays can be found above in section 4.4.4. A calibration curve of cell proliferation was generated by seeding cells on all subsets of the PLGA scaffolds at densities of 10,000; 50,000; 100,000; 500,000; 1,000,000; and 2,000,000 cells/well and AB reading taken after overnight incubation (assuming no cell proliferation on day 0/1) . Experimental results were fitted to this calibration curve to determine cell numbers/densities over 1 week period and then these values were fitted to the MatLab curve to compare predictive modeling vs. experimental data.

For cell seeding, moMSCs were seeded onto PLGA scaffolds containing different gelatin concentrations at a density of 200,000 cells/well and allowed to attach to scaffolds for 1 hour prior to complete medium addition. Cells were cultured in IMDM supplemented with 10% FBS, 2% ABAM and 200mM L-Glutamine where medium was changed every 3 days. Cells were cultured for 7 days.

4.8 Statistics

Unless indicated otherwise, scaffold all characterization and mechanical tests were repeated independently at least 3 times with triplicate samples each. All cell culture experiments were ran in triplicate and repeated three times. Animal experiments were performed at n=4 per experimental group. All statistical significance was determined using a two-way ANOVA with Tukey test with $p < 0.05$ (*) and $p < 0.01$ (**).

Chapter 5. Optimization and Characterization of Electrospun Chitosan/Hydroxyapatite/Genipin Scaffolds

5.1 Morphology of Genipin crosslinked chitosan/hydroxyapatite nanofibers

Optimization of the electrospinning process for generating pure chitosan (CTS) and chitosan-hydroxyapatite (CTS-HA) fibers was required because most current processes use fiber-forming high molecular weight additives, such as poly(ethylene oxide) (PEO), which can inhibit multi-layer growth of cells [82]. Initial optimization included systematically adjusting the solute concentration, flow rate, working distance and voltage of the electrospinning platform, as previously described [76, 83-85], to yield electrospun fibers that were continuous, uniform in shape and without beading. The measured thickness of a typical, optimized, electrospun nanofibrous scaffold mat, such as shown in Figure 10A, was 25.3 ± 16.2 μm (n = 28, Figure 10B). The diameters of the individual non-crosslinked fibers in the mat, as evaluated by SEM, were on the average 227.8± 154.3nm (n=10 independent samples, analyzing ~50 fibers/sample, Figure 12A). Crosslinking and hydration caused an increase in the diameter of the fibers to 334.7 ± 119.1 nm (n=10 independent samples, analyzing ~ 50 fibers/sample (Figure 11). In contrast to the smooth surface of CTS-GP fibers (Figure 12A), CTS-HA-GP fibers contained nanoparticles dispersed on the surface (Figure 12B).

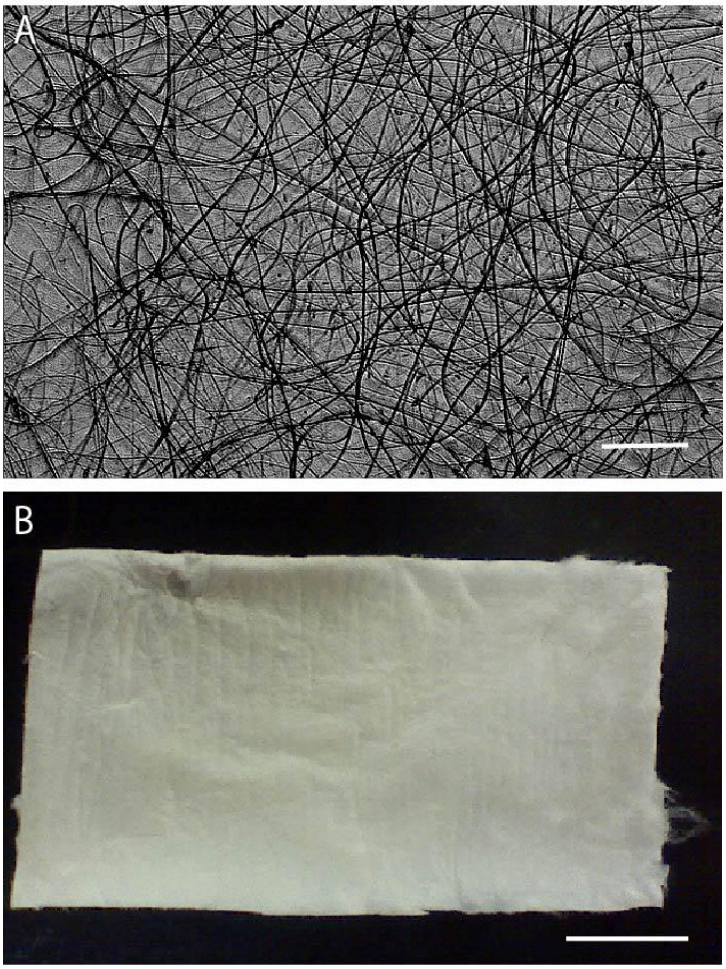

Figure 10. Macro/microscopic images of electrospun CTS fibers. Examples of electrospun chitosan microfibers (A) and of a fibrous mat (B). Scale bar for (A) is 200μm and for (B) is 1cm.

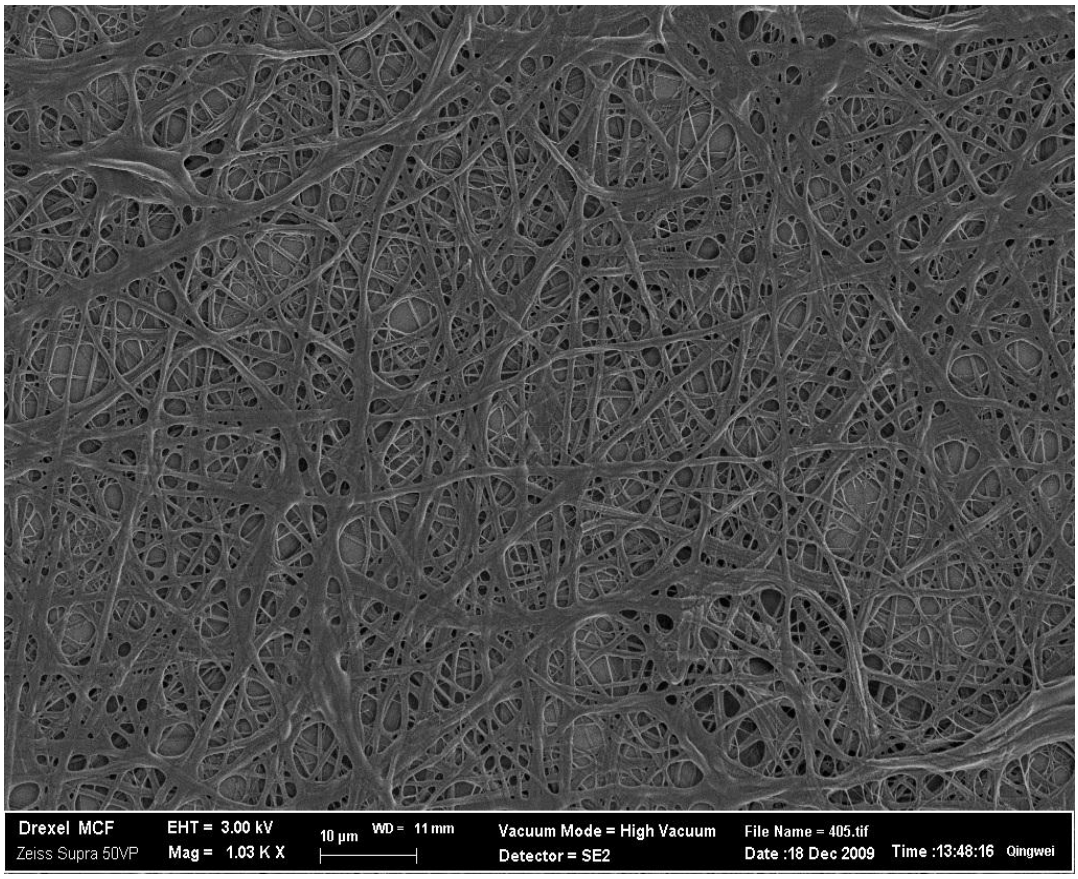

Figure11. Electrospun CTS fibers crosslinked for 24hours with an aqueous 0.1% genipin solution. Fiber diameter was observed to increase from 227.8± 154.3nm to 334.7 ± 119.1 nm (n=10 independent samples, analyzing ~ 50 fibers/sample. It can be seen that fibers obtain a flatter morphology and begin to swell after hydration, which can attribute to the increase in fiber diameter.

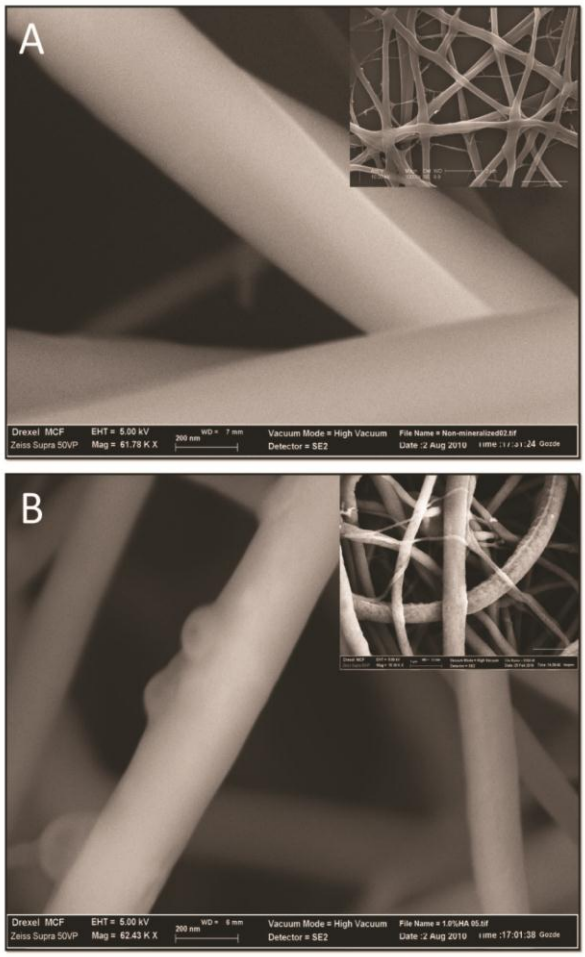

Figure12. The morphology of electrospun scaffolds evaluated by scanning electron. SEM micrographs of 0.1% genipin crosslinked CTS-GP (A) and 0.1% genipin crosslinked 1.0% HA-containing (B) chitosan nanofibers. Scale bars are 200nm. Inserts: Typical morphologies of nanofibers at lower magnification (scale bar for insert in A is 2µm and in B is 1µm). Small nano-size projections were observed on the surface of the HA-containing scaffolds. These were perceived to indicate the presence of HA along the surface of CTS-GP nanofibers, which is mimetic to the natural architecture of bone ECM.

5.2 Evaluation of Nanoparticle Deposits on CTS-HA-GP nanofibers

Three independent approaches, X-ray diffraction (XRD), Fourier transform infrared spectroscopy (FTIR) and energy dispersive X-ray spectroscopy (EDS), were employed to further characterize the chitosan scaffolds, specifically the nanoparticle deposits observed on the surface of the CTS-HA-GP nanofibers [86]. XRD spectroscopy shows the characteristic, highly crystalline structure for the pure HA powder, while the spectrum of CTS-GP scaffolds resembled that of amorphous electrospun CTS (Figure 13A and B).

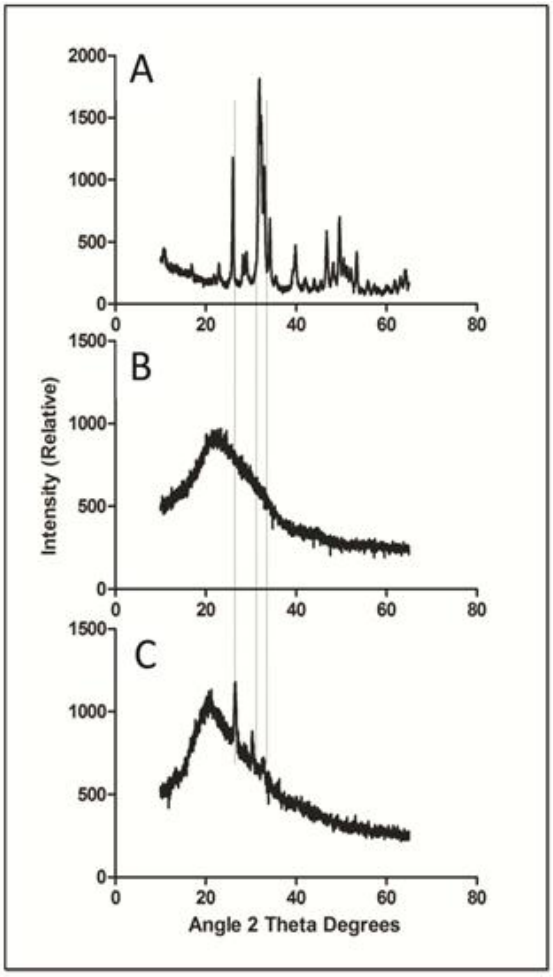

Figure13. X-ray diffraction spectra of hydroxyapatite (A), 0.1% genipin crosslinked 7% chitosan nanofibers (B) and 1.0% HA-containing 0.1% genipin crosslinked 7% chitosan nanofibers (C). The alignment of the peaks is indicated by the dashed lines. Due to its highly crystalline structure, HA spectra have very defined peaks indicative of the diffraction of x-rays off of the crystal lattice (A). Electrospun CTS-GP scaffolds have an amorphous structure, which is indicated by the non-specific spectra observed (B). The composite HA-containing CTS-GP scaffolds obtain both of these properties having a non-specific amorphous characteristic containing the crystalline peaks observed in HA (C).

The spectra for the CTS-HA-GP composite fibers containing nanoparticles revealed three distinct peaks at 26.21, 30.24 and 32.41 degrees corresponding to HA. These new peaks indicate introduction of crystalline properties into the amorphous nanostructure of the CTS-GP scaffolds due to the presence of HA and, therefore, indicate the formation of a biocomposite material (Figure 13C). The phosphate groups in pure HA showed characteristic FTIR bands between 900-1100cm^{-1} and 500-600cm^{-1}(Figure 14A) indicative of phosphate bending and stretching respectively [86]. FTIR Spectra of the CTS-HA-GP bio-composites revealed bands at 500-600cm^{-1} that did not appear in the

CTS-GP scaffold spectra (Figures 14B and C), which can be attributed to the molecular interactions of HA and CTS. Additionally, there was a broadening of the band around 950cm^{-1} and 1085cm^{-1} that appeared on the CTS-HA-GP spectra, which has been attributed to the interaction of HA and CTS as well (Figure 14C) [86]. Finally, EDS was used to determine the elemental composition of the individual nanofibers. CTS-GP scaffolds showed large peaks for carbon and oxygen and a small peak for nitrogen, indicating three of the main components of chitosan (Figure 15A). Fibers containing1.0% HA, additionally contained small amounts of calcium and phosphorus (insert in Figure 15A). The peaks for 0.8% HA containing fibers were somewhat smaller, indicating that less HA had been incorporated, while at 2.0% HA the peaks were similar to those at 1.0%, indicating saturation (data not shown). Elemental analysis of the EDS intensity maps showed the distribution of carbon (Figure 15B) and oxygen (Figure 15C) as the main organic components of the fibers, while inorganic calcium (Figure 15D) and phosphate were found (Figure 15E) in the form of HA nanoparticles on each fiber (Figure 15B, C, D, and E, respectively).

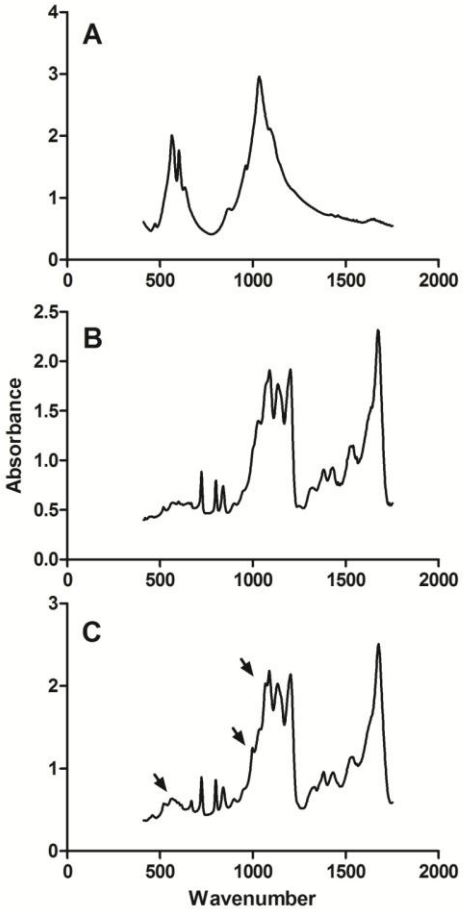

Figure14. Fourier transform infrared spectra of hydroxyapatite (A), 0.1% genipin crosslinked 7% chitosan nanofibers (B) and 1.0% HA-containing 0.1% genipin crosslinked 7% chitosan nanofibers (C). Peaks of interests are designated by arrows. FTIR bands between 900-1100cm^{-1} and 500-600cm^{-1}(A) indicative of phosphate bending and stretching respectively. FTIR Spectra of the CTS-HA-GP bio-composites revealed bands at 500-600cm^{-1} that did not appear in the CTS-GP scaffold spectra (B and C), which can be attributed to the molecular interactions of HA and CTS. Additionally, there was a broadening of the band around 950cm^{-1} and 1085cm^{-1} that appeared on the CTS-HA-GP spectra, which has been attributed to the interaction of HA and CTS as well (C).

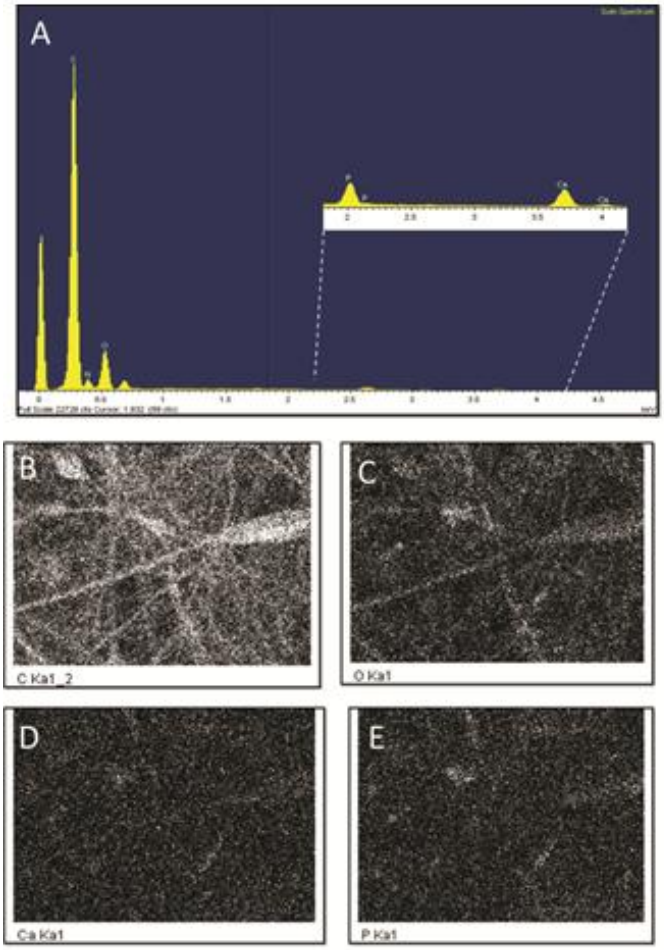

Figure15. Electron dispersion spectroscopy of CTS-GP and CTS-HA-GP bio-composite nanofibers. Spectral analyses comparing the elemental compositions of 0.1% genipin crosslinked chitosan nanofibers (A). Insert: 1.0% HA-containing 0.1% genipin crosslinked 7% chitosan nanofibers show new peaks for calcium and phosphorous due to the presence of hydroxyapatite nanoparticles. Dot-analyses representing the elemental topographical distribution of carbon (B), oxygen (C), calcium (D) and phosphorous (E) of the HA-containing nanofibers.

5.3 Mechanical Properties of CTS-HA-GP nanofibers

The effect of HA on the mechanical properties of genipin crosslinked scaffolds was tested using three different concentrations of HA. As seen in Figure 16A, crosslinking with genipin increased the ultimate tensile strength (UTS), as determined by the stress at break normalized to the cross-sectional area of the scaffold, by approximately 50% when compared to the non-crosslinked scaffolds, however there was no significant difference between the UTS values, when the concentration of HA was increased from 0.8% - 2.0%. Increasing the HA concentration from 0.8%, 1.0%, and 2.0% increased the Young's moduli of non-crosslinked CTS-HA scaffolds significantly from 0.8% to 1.0% ($p < 0.05$),

with no increase when the HA concentration was raised from 1.0% to 2.0% (Figure 16B). Crosslinking with GP resulted in a significant increase in the Young's moduli to 77.2±8.6 to 142.5±12.5 and 147.4±21.7 MPa for samples containing 0.8%, 1.0% and 2.0% HA, respectively. These measurements indicate a 4-5-fold increase ($p < 0.01$) in stiffness for all crosslinked samples over that of non-crosslinked samples (Figure 16B, $n = 6$ scaffolds per condition). Like in the case of the UTS, there was a significant increase in the stiffness when the HA concentration was raised from 0.8% to 1.0% after crosslinking ($p < 0.01$) with no further increase when increasing the HA =concentration to 2.0%. These results are comparable to the EDS results, indicating a saturation of HA on the scaffolds at 1.0%.

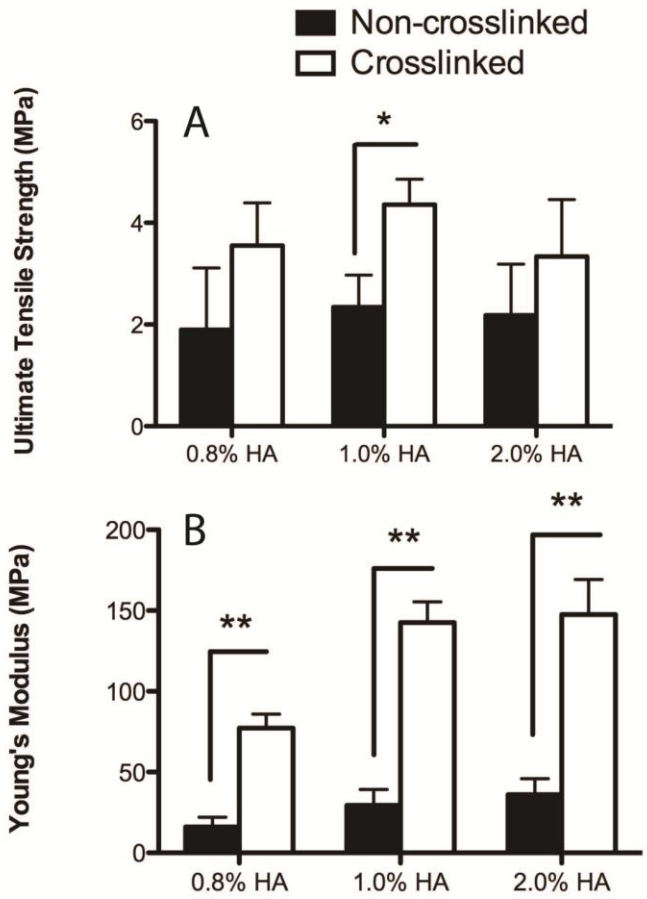

Figure16. Ultimate Tensile Strength (A) and Young's moduli (B) of non-crosslinked (black bars 0.1% genipin and crosslinked (white bars) 7% chitosan nanofibers at different concentrations of hydroxyapatite. While ultimate tensile strength remained relatively unchanged upon crosslinking, a significant change was observed when genipin crosslinking was performed. These results indicate that genipin only increases the stiffness of a the material while relatively maintaining the tensile strength. ** indicates statistical significance at p<0.01 by one way ANOVA with Tukey test.

5.4 Morphology of 7F2 osteoblasts on CTS-HA-GP Scaffolds

The morphology of the cells cultured on CTS-GP and CTS-HA-GP nanofibers was evaluated by SEM. At seven days post-seeding, cells formed extensive cell-scaffold and cell-cell interactions indicative of cellular proliferation/migration (Figure 17A and C) and cell-cell and cell-scaffold interactions, as inferred from the well-defined filopodia

extending from the lamellipodia and “grabbing” the nanofibers on both CTS-GP and CTS-HA-GP scaffolds (Figure 17B and D). The cells were observed for up to 21 days. By day 14, much more confluent monolayers were spread on the both scaffold types, indicating continued proliferation (Figure 17E – H). Noticeable on day 14 was the presence of a rougher texture on the CTS-HA-GP scaffolds (Figure 17E and F) then on the CTS-GP scaffolds (Figure 17G and H), indicating an enhanced maturation of 7F2 cells by the presence of a mineralized ECM deposition. This morphology was maintained on CTS-HA-GP scaffolds up to 21 days and the rough texture was also observed on CTS-GP scaffolds on day 21, indicating the eventual maturation and mineralized ECM deposition (Figure 17I – L).

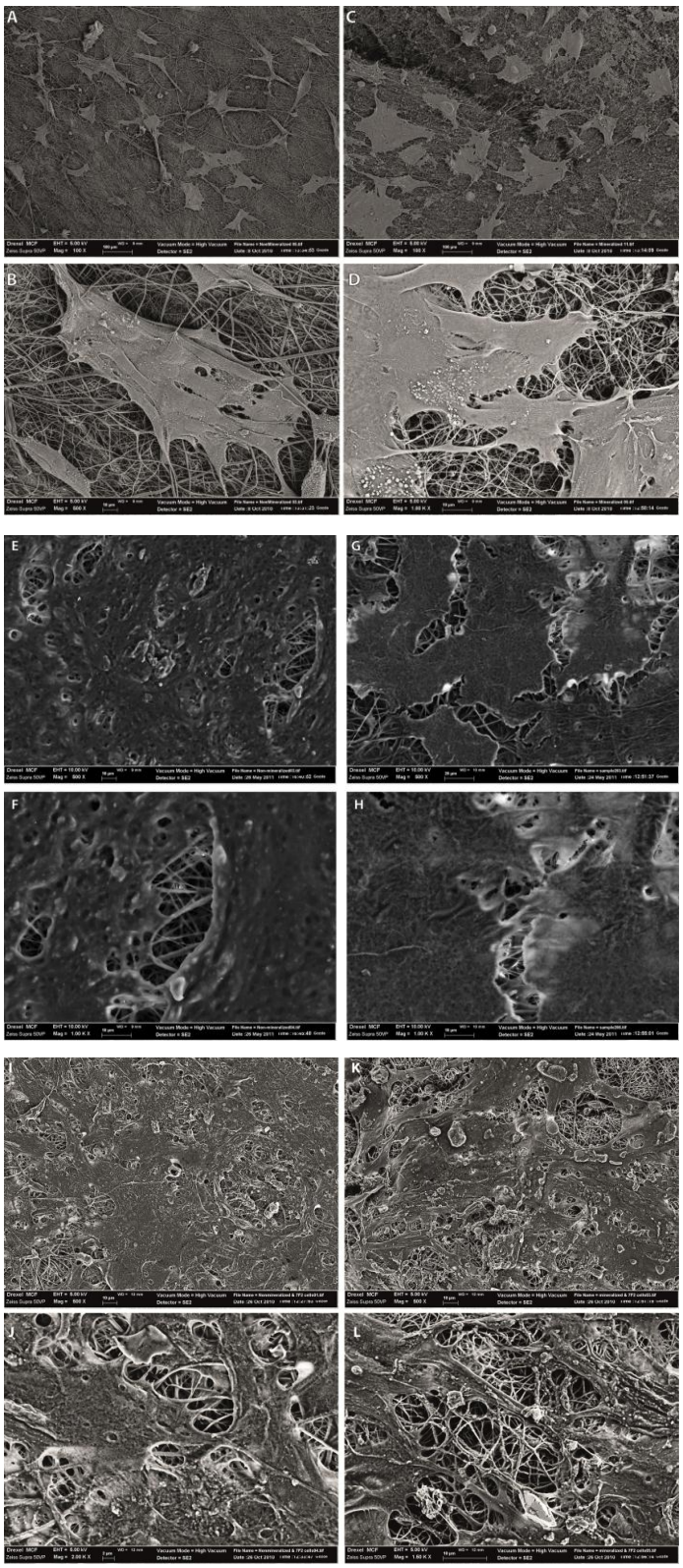

Figure 17. SEM imaging of 7F2 osteoblasts on CTS-GP and CTS-HA-GP nanofibers. SEM micrographs of 7F2 cells at day 7 on CTS-HA-GP scaffolds (A 500X and B 1000X) and CTS-GP scaffolds (C 500X and D 1000X), at day 14 on CTS-HA-GP scaffolds (E 500X and F 1000X) and CTS-GP scaffolds (G 500X and H 1000X) and at day 21 on CTS-HA-GP scaffolds (I 500X and J 1000X) and CTS-GP scaffolds (K 500X and L 1000X).

5.5 Capacity of CTS-HA-GP Scaffolds to Induce Osteogenic Maturation In Vitro

Upon osteogenic differentiation, 7F2 pre-osteoblastic cells, secrete alkaline phosphatase (ALP) and mineralize their own matrix [87]. The osteoinductive potential of the scaffolds was determined by measuring the activity of ALP, an early osteogenic marker, using a colorimetric pNPP assay on days 7, 14, and 21 post-seeding (Figure 18A). When grown on tissue culture plastic (TCP), 7F2 cells had low ALP activity that remained stable over a 21-day period and was consistently lower than when grown on the cross-linked CTS-GP scaffolds ($p< 0.01$). By day 14, ALP activity in cells growing on the CTS-HA-GP bio-composite scaffolds was 2.4 fold higher than on CTS-GP scaffolds ($p < 0.01$). Expression of this early osteogenic marker decreased on both scaffolds by day 21 as differentiation continued and cells matured. Cell metabolic activity was assessed continually using the alamarBlue^{TM} (AB) assay. As seen in Figure 18B, the metabolic activity increased in all samples after 3 days. On TCP, AB fluorescence continued to increase over 21 days, while CTS-GP samples remained stable and CTS-HA-GP bio-composite samples decreased (Figure 18B). Cells cultured on TCP had the highest AB fluorescence at all time points, indicating maximal metabolic activity and, presumably, a minimal degree of differentiation. After an initial increase, the AB fluorescence of cells on CTS-HA scaffolds remained relatively stable over the experimental time course, suggesting a decrease in metabolic activity compared to TCP. This AB stability may also indicate that the cells are undergoing differentiation. Lastly, AB fluorescence on CTS-HA-GP composite nanofibers decreased over time, which may indicate enhanced differentiation in comparison to the CTS-HA scaffolds.

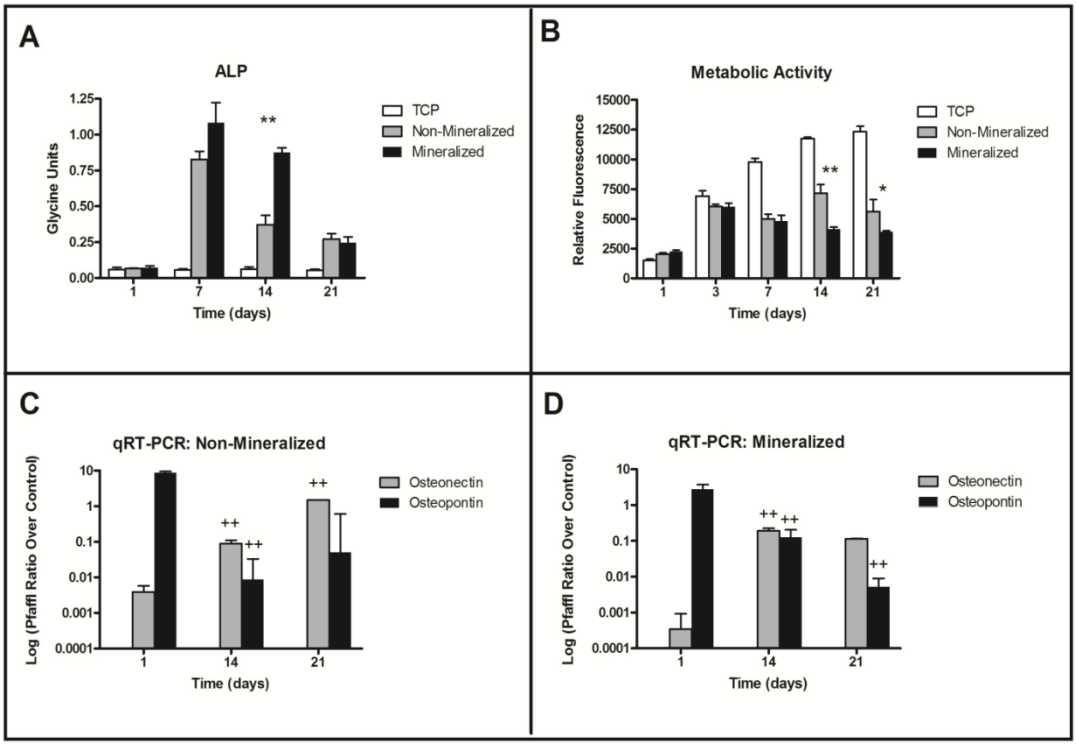

Figure18. Metabolic activity, alkaline phosphatase expression and osteogenic marker expression of 7F2 osteoblasts on CTS-GP and CTS-HA-GP composite nanofibers. Alkaline phosphatase expression of 7F2 osteoblasts on days 1, 7, 14 and 21 (A), metabolic activity of 7F2 osteoblasts measured by alamar blue on days 1, 3, 7, 14 and 21 and mRNA expression of osteopontin and osteonectin of 7F2 osteoblasts on days 1, 14 and 21 on CTS-GP (C) and CTS-HA-GP (D) 0.1% genipin crosslinked chitosan nanofibers. * and ** indicate a significant difference ($p < 0.05$ and $p < 0.01$ respectively) between CTS-GP and CTS-HA-GP scaffolds at the same time point; ++ indicates a significant difference ($p < 0.01$) of the specified scaffold compared to the same scaffolds at the earlier time point.

Early and late markers of osteogenic differentiation were assessed by qRT-PCR, measuring RNA expression of osteopontin (OP) and osteonectin (ON), respectively. As seen in Figures 18C and D, the expression of OP, an early marker of osteogenic differentiation is highest 24 hours after cell seeding and then decreases progressively at days 14 and 21 on both the CTS-GP and CTS-HA-GP composite scaffolds. By contrast, the mRNA expression of ON, which is a late marker of osteogenic maturation, was at its lowest levels at 24 hours and increased on days 14 and 21 in cells growing on the CTS-

GP. However, on the CTS-HA-GP scaffolds, a significantly larger increase (by ~2 orders of magnitude) in ON expression, a marker of late osteogenic differentiation, between 24 hours and day 14 (with a subsequent plateau at day 21) was noticed when compared to the CTS-GP scaffolds. These data indicate that the presence of HA accelerated/enhanced osteogenic differentiation/maturation of 7F2 cells. This was further clarified by a similar trend in the decrease of OP, a marker of early osteogenic differentiation, on the mineralized scaffolds between 24 hours and 14 days on the CTS-HA-GP scaffolds with respect to CTS-GP scaffolds.

5.6 Discussion

Repair of large bone defects remains a challenge in clinical practice and has spurned considerable reconstructive efforts by bone tissue engineering. The relative success of autografts in the repair of craniofacial defects has been ascribed to the recruitment of stem cells by functional periosteum [23]. Periosteum, the thin fibrous layer surrounding bone, harbors mesenchymal progenitor cells whose recruitment, activation, and osteogenic differentiation is essential for bone graft integration, healing and remodeling [88]. By blocking fibrotic infiltration, the periosteum can beneficially promote the movement of osteoblasts across an allograft's surface while inducing their differentiation and proliferation [8]. Unlike autografts, however, allografts and other bone substitutes transplanted without this layer are, at best, osteoconductive. Our aim was to generate an allogeneic template scaffold that has the potential to act as a "bridge" on the periosteal interface of non-load bearing bone defects to induce osteogenic migration and self-regeneration. In this study, we evaluated the physicochemical characteristics of such

scaffolds as well as their ability to promote adhesion, proliferation and osteogenic differentiation of osteoblast-like 7F2 cells.

Ideally, an engineered allogenic bone scaffold will architecturally resemble bone matrix and have mechanical properties suitable for non-weight bearing, such as the repair of calvaria or similar craniofacial bones. Several two-step electrospinning processes have been described in the past for the formation of hydroxyapatite (HA) containing nanofibers by co- precipitating an HA solution and a polymer of interest, such as chitosan [60, 89]. In this study we developed a simpler, one-step solution, in which we dissolved chitosan (CTS) and dispersed HA in trifluoroacetic acid (TFA) to create a homogenous, electrospinnable solution/dispersion. While CTS completely dissolved in TFA, HA did not, as inferred from the turbid appearance of the solution containing HA versus the clear solution without it. However, the homogenous dispersion of HA nanoparticles in TFA did permit the formation of CTS fibers which incorporated HA nanoparticles on the surface of composite fibers (Figure 12). Furthermore, by increasing the concentration of CTS from 2.7% to 7%, we were able to increase the previously reported thickness of the scaffolds by ~2 fold, from 10.1 ± 5.8 μm to 25.3 ± 16.2 μm [90].

As another innovation, , we were able to electrospin CTS nanofibers without the use of a fiber-forming agents (FFAs), such as ultrahigh molecular weight polyethylene oxide (UHMWPEO) which is often used to enhance chain entanglement of materials that do not have high electrospinnability [91] [60]. Past studies have indicated a need for FFAs, such PEO, in the case of electrospun soy-protein-isolate (SPI) solutions that could not form continuous fibrous meshes without an FFA [92]. SPI is a new “green” material derived from the soy plant that is currently being evaluated as a potential scaffold for wound

dressings [92]. As a caveat, it has been reported that inclusion of FFAs into a scaffold may delay or reduce cell adhesion, proliferation and/or differentiation due to their inherent nature in inhibiting protein adsorption [54].

It was also discussed that optimization of the solution was required in order to achieve smooth, non-beaded fibers for evaluation. Although a number of papers discuss electrospun CTS fibers [43, 75, 90, 93, 94], there are many factors that play into electrospinning CTS. It can be observed in different literature selections many different concentrations of CTS, different solvents used and different spinning parameters. These variations, we believe, are due to the stringent requirements for electrospinning CTS including humidity, temperature and % deacetylation. In our study, we were able to obtain the best fibers in lower humidity, ~30% humidity as opposed to 50-60% and at lower temperatures, around 20^{o} – 22^{o}C as opposed to 27^{o} – 30^{o}C. Our degree of deacetylation was 75%-85% which, along with humidity and temperature conditions, proved to produce smooth and continuous fibers without beads at a concentration of 7% CTS in TFA.

To evaluate the topography, structure, and fiber composition of HA containing electrospun scaffolds, we used 4 independent material characterization techniques (SEM, XRD, FTIR, and EDS). By using multiple independent techniques, we were able to create a diverse, representative characterization as to where the HA nanoparticles were situated in accordance to the fibers/mats, the crystalline properties introduced to an otherwise amorphous scaffold, the molecular interactions that represent the presence of HA and an elemental analysis indicative of both CTS (organic) and HA (inorganic). Analysis of SEM micrographs (Figure 11), revealed a mean fiber diameter of 335±119 nm for CTS-

GP scaffolds. This large variability and heterogeneity in the size of electrospun CTS nanofibers has been described before and may be due to inhomogeneity of the solution [68, 95, 96]. CTS has an extremely high surface tension and requires harsh solvents, such as TFA for appropriate fiber formation upon electrospinning [90]. We surmise that the large variability in fiber diameter we observed may be caused by the harsh solvents and/or conditions required to electrospin chitosan without and FFA.

EDS characterization ascertained that the nanofibers electrospun from the CTS containing 1.0% HA solution contained small amounts of calcium and phosphorous. The EDS peaks seen in Figure 15A show the presence of the main elemental components of chitosan: carbon, oxygen and nitrogen. Additionally, smaller phosphorous and calcium peaks are detected in the CTS-HA-GP scaffolds (Figure 15A, insert). To confirm the identities of the nanoparticles seen on the fibers, elemental analysis was performed. Carbon and oxygen (Figs. 15B and C), represented as white dots, make up the main components of the nanofibers, while smaller amounts of calcium and phosphorous (Figures 15D and E) are dispersed amongst the carbon and oxygen. Heinemann et. al. (2008) used qualitative EDS to determine the presence of calcium and phosphorous on collagen-coated chitosan scaffolds after seeding with 7F2 cells and concluded that the presence of these elements indicated mineralized matrix deposition from the 7F2 cells [97].

The XRD spectra of the bio-composite HA/chitosan scaffolds show distinct peaks that specifically match those found in pure HA samples (Figure 13). The peaks in the CTS-HA-GP spectra are an indication of semi-crystalline HA structures present in the composites as opposed to the completely amorphous nature of CTS-GP scaffolds. As

additional evidence for the presence of HA in composite scaffolds, molecular interactions and vibrations in the CTS-HA-GP scaffolds were analyzed by FTIR. While calcium is vibrationally "undetectable," some small bands between 1000-1100cm^{-1} and 500-600cm^{-1} were noted on the HA-containing scaffold (Figure 14). These bands reportedly correspond to the presence of PO_4 in the scaffold after HA mineralization [86, 98]. Broadening of the peak at 950 cm^{-1} and superposition of 1085cm^{-1} peaks (see Figure 14) have also been attributed to the interaction of HA and chitosan [98].

Successfully engineered tissue constructs will physicochemically and structurally mimic the native tissue and its unique mechanical properties. While electrospun scaffolds morphologically resemble the fibrous structure of the ECM, the mechanical properties of fibrous scaffolds make them less suitable for use as bone analogs. Crosslinking can enhance the mechanical properties of the constructs and fine-tune them to approximate the fibrous tensile properties of bone ECM. Here we used genipin (GP) as a natural, increasingly popular non-toxic crosslinker [68, 72, 74]. Genipin has recently been shown to increase the mechanics of electrospun chitosan fibers and was observed via a suture pullout strength test [44]. Although there was a 48% increase in pullout strength when 10mM genipin was added to the chitosan solution, this strength was still 51% less than the clinically excepted glutaraldehyde crosslinked collagen product Biomend Extend [44]. While the complete mechanism of how genipin crosslinks chitosan is still under investigation, but is described to be a spontaneous reaction between genipin and the NH_2 subunits on the chitosan chain [43]. . This stabilization in turn causes an increase in the scaffold stiffness: the Young's modulus of our scaffolds increased significantly upon cross-linking, while the ultimate tensile strength was only marginally increased (Figures

16A and B). Since the mechanical properties of our scaffolds increased with HA concentrations up to 1.0% but not beyond that, we focused on 1.0% HA as a working concentration for other subsequent studies. In this study we tested our scaffolds while wet to mimic the aqueous environment of the human body. Upon crosslinking with GP, the Young's modulus of these scaffolds increased about 4-fold to 142±13 MPa, which approximates the modulus of non-weight-bearing bone.

Our findings contrast those of Zhang et al. (2010), who recently reported that incorporation of HA reduces the mechanical strength of their electrospun chitosan/collagen scaffolds [60]. The Young's modulus of their non-crosslinked chitosan/UHMWPEO scaffolds was 92.2 ± 19.1MPa and decreased to 57.3 ± 15.5 MPa and 48.2 ± 8.3 MPa upon incorporation of HA and HA/collagen respectively. In our experiments, the Young's' modulus of 1.0% HA-containing, non-crosslinked, waterproofed chitosan scaffolds was 25.2±9.2MPa (Figure 16B). The lower values for our scaffolds may reflect the absence of UHMWPEO or, alternatively, be due to a dispersion of the HA nanoparticles on/near the surface of the nanofibers rather than an incorporation into the molecular structure of the polymer solution. If the HA particles are in fact incorporated into the molecular structure, than they will disrupt molecular chains and therefore decrease its mechanical strength. This decrease would not occur if HA is simply dispersed on or near the surface of the scaffolds. Another explanation is the substantial reduction in the amount of HA we used as compared to Zhang et. al. 2010. Our w/w% of HA and chitosan in solution is 14% HA nanoparticles with 86% CTS, whereas Zhang et. al. used 27.8% HA nanoparticles, 7.2% collagen and 57.8% CTS. This incorporation of double the amount of HA we used may have caused further

disruption in the formation of stable CTS, nanofibers, causing a significant decrease in the Young' modulus. Finally, as yet another explanation, the difference in mechanical properties of the scaffolds may also be due to the fact that Zhang et al. used collagen, which is more elastic than chitosan.

In terms of functional tissue engineering, our aim was to fabricate a scaffold with structural and mechanical properties similar to those of non-load bearing bone containing the regenerative capacity of periosteum. Specifically, our goal was to generate a bioactive scaffold capable of inducing/accelerating osteogenic differentiation similar to what occurs when osteoprogenitor cells from the periosteum migrate to damaged bone tissue. The periosteum plays a central role in the health of bone tissue, as it is the source and site for the recruitment of osteoprogenitor cells responsible for initial repair and regeneration at sites of injury [23, 27, 28]. In comparing the effects of ablating different sources of osteoprogenitor cells, recent studies showed that removal of progenitor cells from the bone marrow had minimal effect of osteogenesis, while removal of the periosteum caused a 73% decrease in new bone formation, indicating the crucial role of periosteum in regeneration [27, 28]. The osteogenic properties of our CTS-GP and CTS-HA-GP fibrous scaffolds were assessed *in vitro* using 7F2 mouse osteoblast like cells. As seen in Figure 17, the cells attach to the scaffolds, proliferate and over a 14-day period cover the scaffold in a multilayered fashion. At the same time, the metabolic activity (as inferred from AB fluorescence) decreased over time in cells cultured on HA-containing scaffolds (Figure 18B). Cells undergoing differentiation cease proliferation leads to a decrease in their metabolic activity [99]. Hence, the decrease in AB fluorescence in our study is likely due to differentiation of cells, and corresponds to the increase in ALP activity seen

in Figure 18A. AB fluorescence is commonly used, upon calibration, to measure cell proliferation; a decrease in AB fluorescence is often interpreted as decreases in cell numbers [100]. However, in combination with the SEM images of proliferating cells in Figures 21A-D we surmise that decrease in AB fluorescence genuinely reflect a decrease in the metabolic activity of cells, which plateaued before reaching confluence on CTS-GP and declined on CTS-HA-GP scaffolds. We believe that this decrease is not due to cell death, but rather is a result of the cells undergoing enhanced differentiation in response to the osteogenic cues of the scaffolds (Figures 17 and 18). More recently, Venugopal et. al. (2011) showed that the presence of HA in chitosan scaffolds caused a significant increase in matrix mineralization [101], further supporting our conclusion that decreased AB activity might reflect enhanced osteoblast differentiation.

In line with previous studies, ALP activity at days 7 and 14 was significantly higher ($p < 0.05$, see Figure 18A), when the cells were cultured on HA-containing bio-composite scaffolds, as compared to both CTS-GP scaffolds and TCP [54, 60]. These data suggest that both the surface topography of the substrate and the innate biochemical cues in the scaffolds may play important roles in the osteogenic maturation process. The decrease in ALP activity by day 21 may be attributed to the further maturation of the 7F2 cells. ALP expression is reportedly higher at early stages of osteoblast differentiation peaking around days 14 or 15 [54, 60, 102]. In line with this notion, our study showed a decrease in ALP expression at day 21, indicating that maturation has progressed as also inferred from the upregulation in the expression of some of the later markers, such as osteopontin (OP), an extracellular structural protein responsible for mineralization of the ECM that is highly expressed in osteoblasts as they mineralize the ECM and also deters the migration

of osteoclasts into the site to avoid negating the mineralizing effects due to resorption, and osteonectin (ON), a post-proliferative glycoprotein responsible for binding differentiated osteoblasts to the calcium found in the fully mineralized ECM, [103]. As seen in Figures 18C and D, while both CTS-GP and CTS-HA-GP scaffolds promote 7F2 cell maturation and differentiation, the cells cultured on the HA-containing scaffolds matured at a faster rate, evident by a sharp increase in ON and sharp decrease in OP mRNA from day 1 to day 14 on CTS-HA-GP scaffolds, as compared to the more gradual and linear increase on CTS-GP scaffolds ($p < 0.01$). Our data are in line with previous studies demonstrating that chitosan scaffolds support osteogenesis of pre-mature osteoblasts and the osteogenic differentiation of human bone marrow derived mesenchymal stem cells (MSC) [104-107]. For example, chitosan nanofibers -reinforced poly(butylene succinate) microfibers induced osteogenic differentiation of human bone marrow derived MSC, as assessed by the increased gene expression of ALP, OP, bone sialoprotein, osteocalcin, Runx2 and Osterix [57]. Similarly, chitosan containing poly(caprolactone) nanofibers promoted osteogenic maturation of MC3T3 mouse pre-osteoblasts over a 14 day period, as assessed from the enhanced gene expression of collagen 1 and OP in the presence of chitosan when compared to TCP and PCL alone [59]. In adding to this body of evidence for the usefulness of chitosan as base material for bone scaffolds, our study is the first to show that the presence of HA and crosslinking with GP significantly enhances the mechanical strength of electrospun CTS based nanofibrous scaffolds and their capacity to induce osteogenic differentiation of osteoprogenitor cells.

Chapter 6. **Evaluation of the Osteoinductive and Osteoconductive Properties of Electrospun CTS-HA-GP Scaffolds**

6.1 Osteogenic Differentiation of Mouse Mesenchymal Stem Cells

Osteoinduction is defined as the ability of an agent to induce osteogenic differentiation. Osteoinductive agents include growth factors, biomolecules or materials. The next aim in this project was to show the capacity of these scaffolds to induce osteogenic differentiation of mouse mesenchymal stem cells. The previous chapter discussed the ability of these scaffolds to support the growth and maturation of 7F2 mouse osteoblast-like cells. These cells are already committed towards an osteogenic lineage, unlike MSCs that are multipotent, with the potential to differentiate towards osteogenic, adipogenic or chondrogenic lineages, respectively. Guiding MSCs towards an osteogenic lineage would prove the true osteoinductive-potential of these scaffolds.

To demonstrate this, scaffolds were seeded with moMSCs and monitored over a 21 day period. The increase in cell numbers and cell spreading were initially observed by staining with DAPI and phalloidin and fluorescently imaging the scaffolds at weeks 1 and 3 at a density of 100,000 cells/well and 500,000 cells/well. When seeded at lower densities on the scaffolds, moMSCs show a reduced proliferative and do not achieve confluent monolayers with and without the presence of HA (Figure 19). After 1 week, the cells were at a very low confluency and sparsely spread out on the scaffold. By week 3, the cells were still at a very low density, with limited cell-cell contact. When seeded at the higher density cells establish confluent monolayers and almost completely cover the scaffold after 7 days (Figure 20). Based on these preliminary results, we monitored the

osteogenic properties using a high seeding density. A 3D rendering of the cells seeded at a higher density, indicated a 3 fold increase in the thickness of cell layer at weeks 2 as compared to week1 (Figure 21). In order to show the additive effect of using an osteogenic medium on the cells cultured on the osteogenic scaffold, we compared cell proliferation and differentiation in standard and osteogenic growth media.

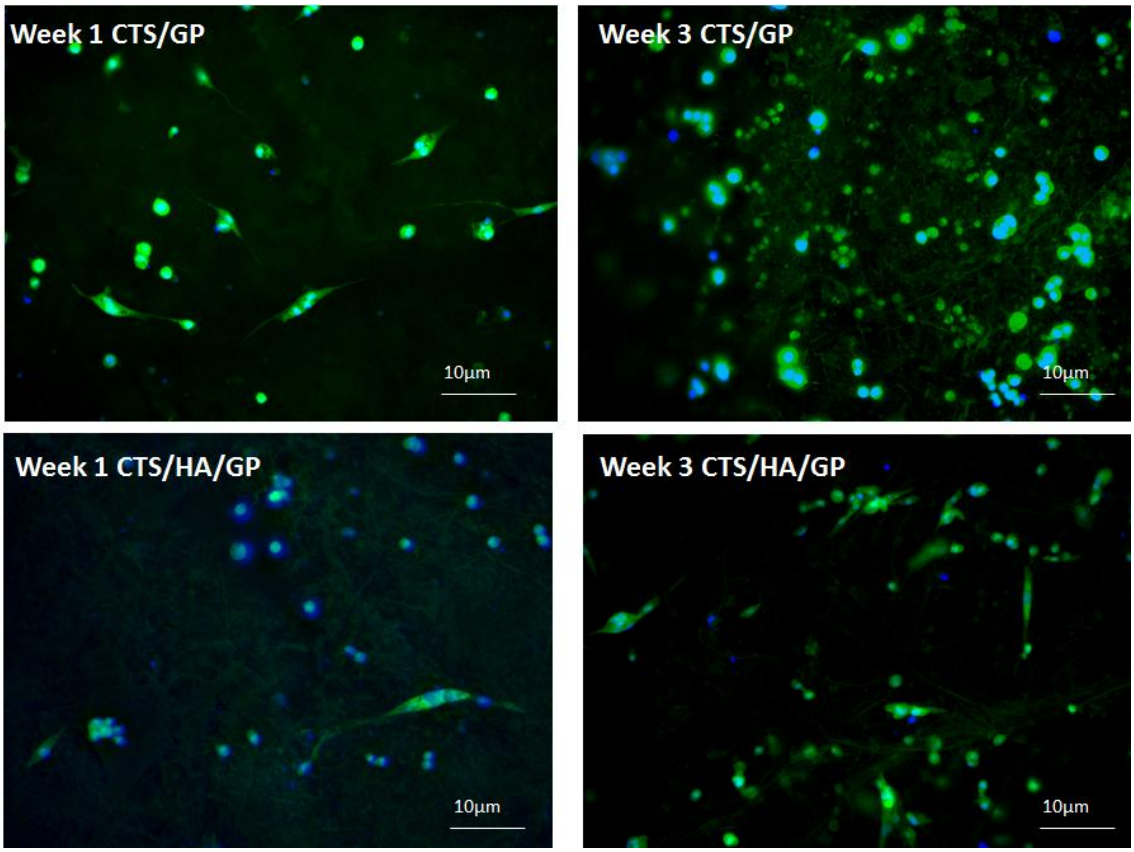

Figure19. moMSC seeded on chitosan scaffolds at low density. 100,000 cells were seeded per scaffold type. It is observed that cells do not proliferate when not in contact with each other and that the presence of HA in the CTS-GP scaffolds does not induce proliferation either. Magnification is at 10X.

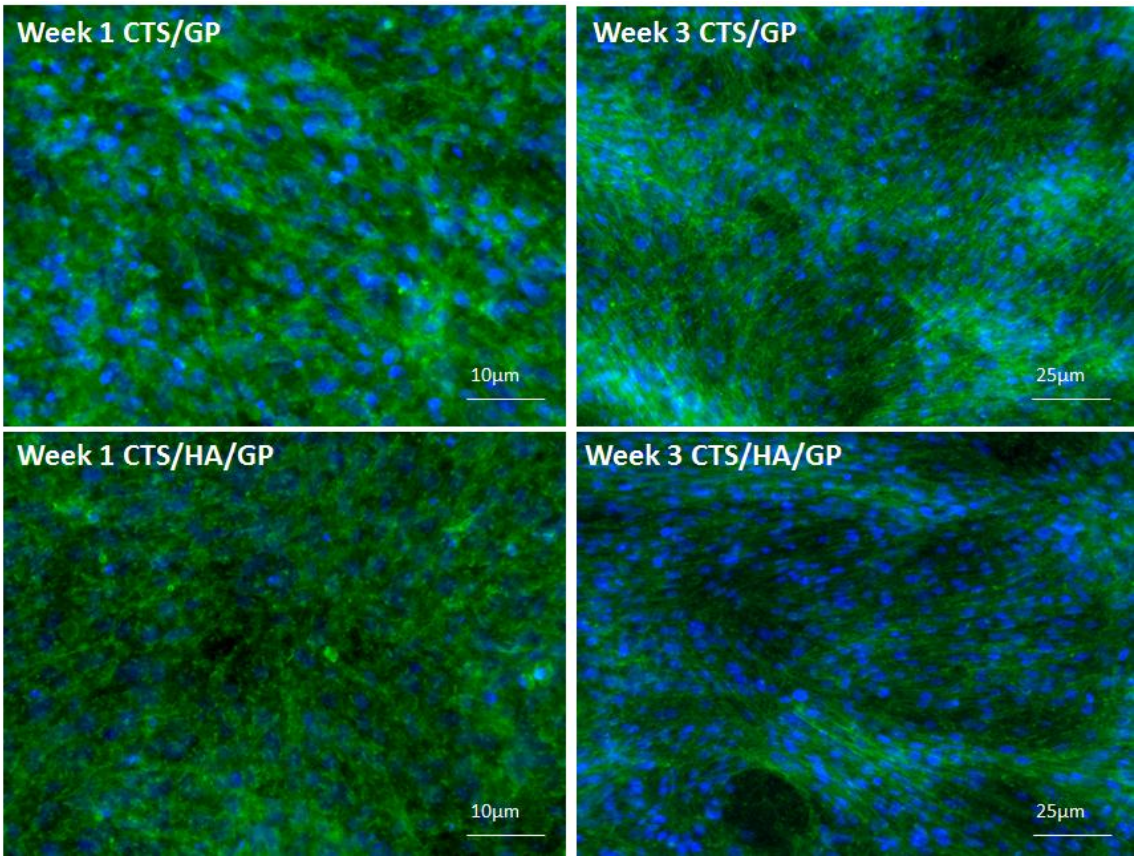

Figure 20. moMSC seeded at high density on chitosan scaffolds. 500,000 cells per scaffold showed sufficient cell sheet formation after 3 weeks as well as patterned cytoskeleton indicative of osteoblast cytoskeletal arrangement. Week 1 images taken at 20X and Week 3 at 10X

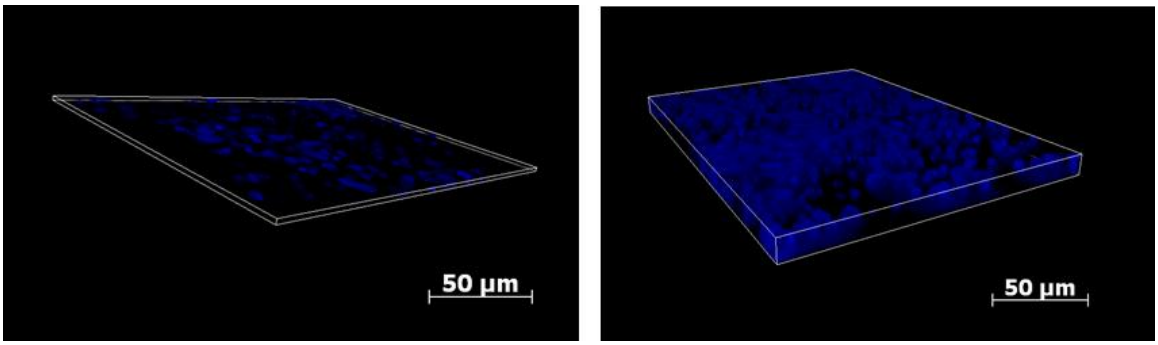

Figure21. 3D rendering of the cells seeded on CTS-HA-GP scaffolds at 1 week (left) and 2 weeks (right), showing a thickness of 8µm at 1 week and of 24µm at 2 weeks. This thickness was maintained through 3 weeks (not shown). These findings can lead to the conclusion that cells are forming multi-layer cell sheets on top of the scaffolds, indicative of the early stages of tissue formation.

As mentioned in chapter 5, Alamar blue can be used to observe the metabolic activity of viable cells. Metabolic activity can be used to determine whether or not cells are in the proliferative stage or the differentiation stage [50]. As seen in Figure 22A, the cells are highly metabolically active throughout the first week. Metabolic activity decreased significantly day 10 on all scaffold and medium types and plateaued at days 14 and 21. This decrease in AB activity is not due to the cell apoptosis, as indicated by the persistence of cell proliferation throughout 2 weeks as shown in Figure 21 and by the continued confluence for up to 3 weeks as shown in Figures 20.

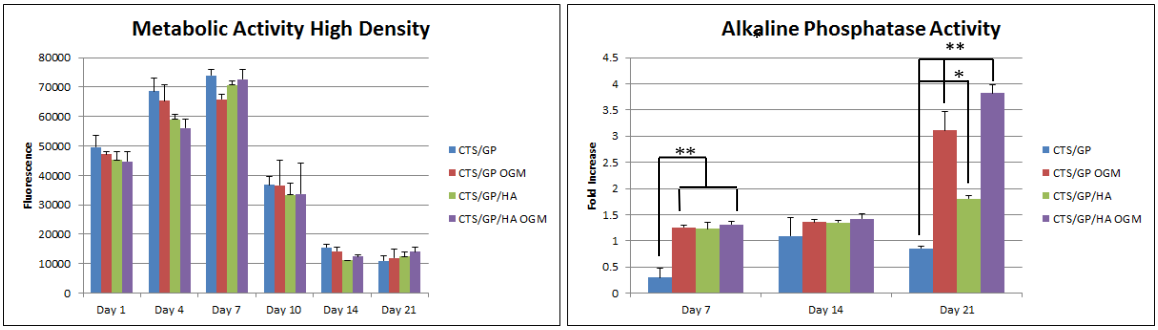

Figure22. Metabolic activity (left) and ALP activity (right) indicating that metabolic activity decreases by day 21 10 while ALP activity increases, indicating that cells are leaving the proliferation stage and entering the differentiating stage by day 21 on CTS-GP (CTS/GP) and CTS-HA-GP (CTS/GP/HA) scaffolds with and without the addition of an osteogenic growth medium (OGM). ALP activity showed a 2 fold increase on HA-containing scaffolds, a 4.5 fold increase when cultured in the presence of an osteogenic medium, and a 6 fold increase when containing HA and cultured in osteogenic medium when compared to CTS-GP scaffolds alone. This 6 fold increase indicates a cooperative/additive effect of the physicochemical cues, i.e. the presence of HA and the contents of the osteogenic medium. * indicates statistical significance with $p<0.05$ and ** indicates statistical significance with $p<0.01$ with n = 4 specimens per group.

In order to test whether this decrease in metabolic activity may be related to osteogenic differentiation, we measured ALP activity. As seen in Figure 22B there was no change in the basal levels of ALP activity in moMSC on both CTS-GP and CTS-HA-GP scaffolds through the first 14 days in both growth medium and osteogenic medium

However, by day 21, cells seeded on CTS-HA-GP scaffolds and in the presence of osteogenic medium showed a significant increase in ALP activity. An additive effect in the presence of HA and osteogenic medium on CTS-GP scaffolds was also observed.

6.2 Osseointegrative Capacity of CTS-HA-GP Scaffolds to Induce In Vivo Bone Growth

An important property of all bioactive scaffolds is the ability to allow natural tissue of the host to grow into the scaffold, also known as osseointegration in bone tissue Here, we used a calvarial defect in female CD1 mice to demonstrate *in vivo* the osteoconductive properties of our scaffolds.

As describe in Materials Methods (4.6.2), scaffolds were implanted into calvarial defects induced in mice using a 2.1mm diameter trephine. Two defects were created on either side of the midline suture down the center of the brain. The experimental procedures were all performed under isofluorane anesthesia and using a suitable stereotaxic set up (Figure 23).

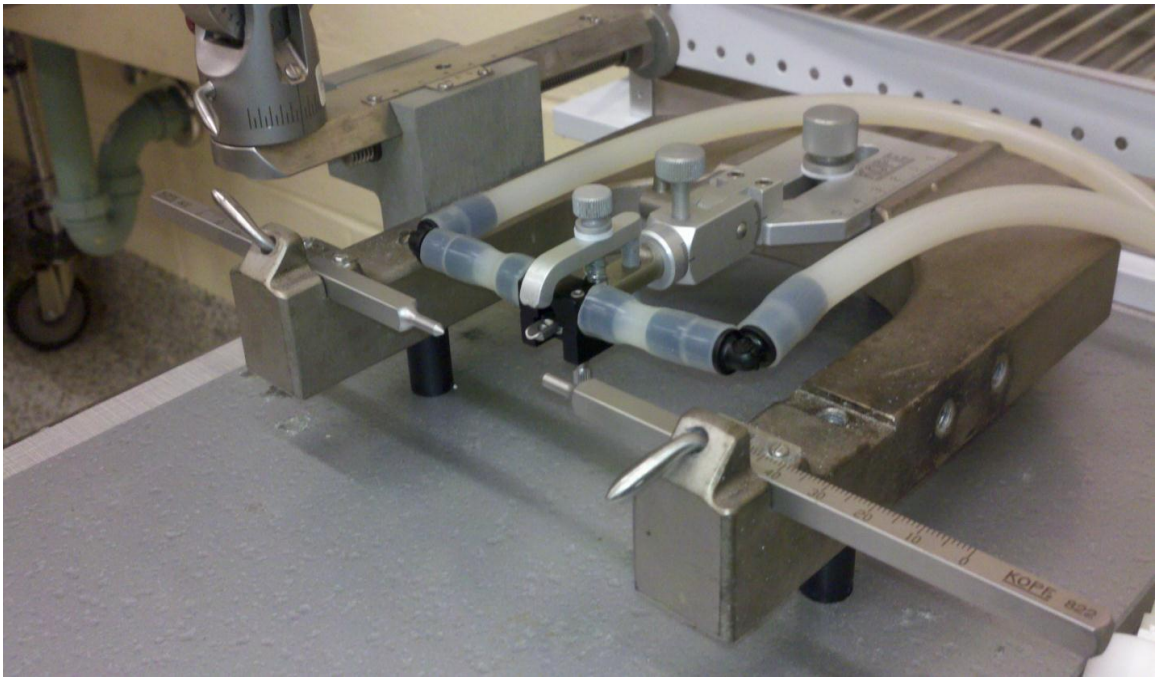

Figure23. Stereotaxic setup to maintain anesthesia and skull stability in mouse surgeries. The ear bars enter the ear canals and lock into the zygomatic arch in order to maintain stability in the x and y directions while drilling. The face mask maintains a constant flow of isofluorane to the mouse and allows the surgery to be completed without pain. The tooth bar is used to stabilize the head in the z direction while drilling.

All surgeries were performed aseptically, The surgical procedure is depicted in Figure 24 and is discussed in detail in Section 4.6.2.

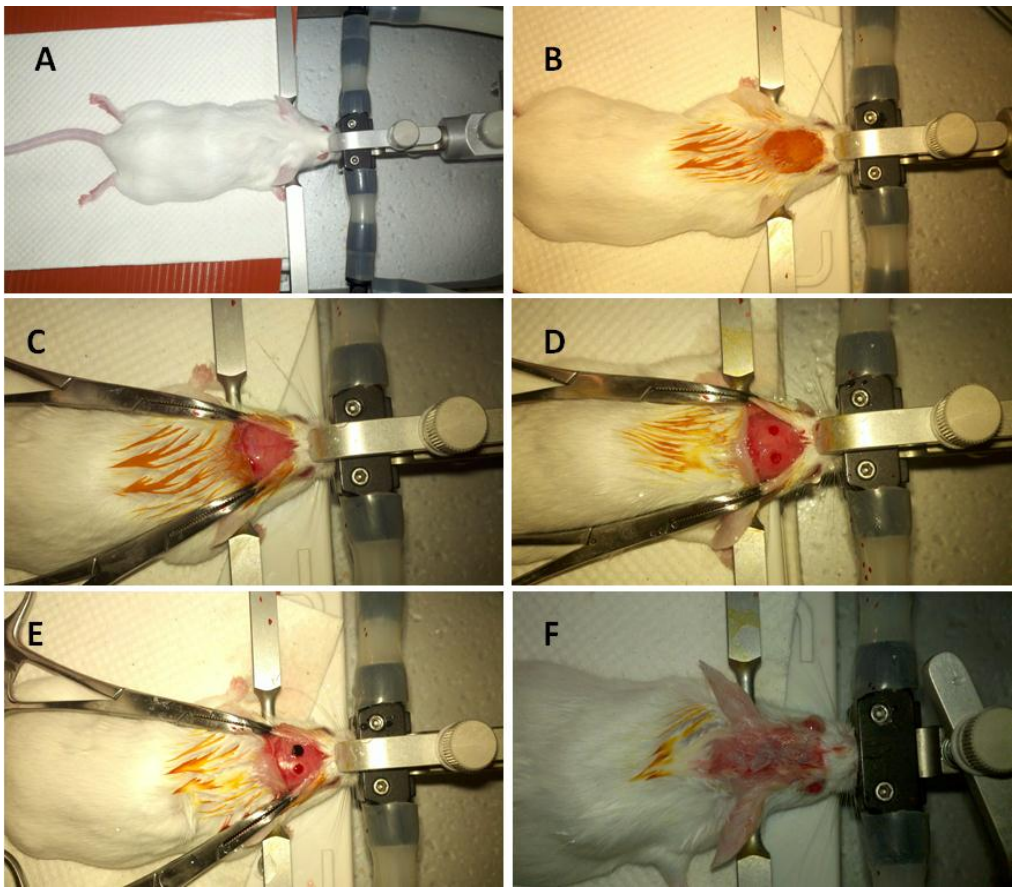

Figure24. Surgical procedure for implanted CTS-GP and CTS-HA-GP scaffolds. The mice were secured in the stereotaxic set up and hooked up to isofluorane anesthesia (A) and prepped for surgery by shaving and applying betadine to the surgery area (B). The incision was made down the midline of the entire skull and hemostats were used to to keep the skin removed from the surgery site (C). The defects were drilled on either side of the midline suture (D) and the scaffold was implanted to one of the defects (E). Finally, the skin was sutured and Vetbond bioglue was used to prevent the mouse from removing the stitches or dislodging the scaffold while grooming (F).

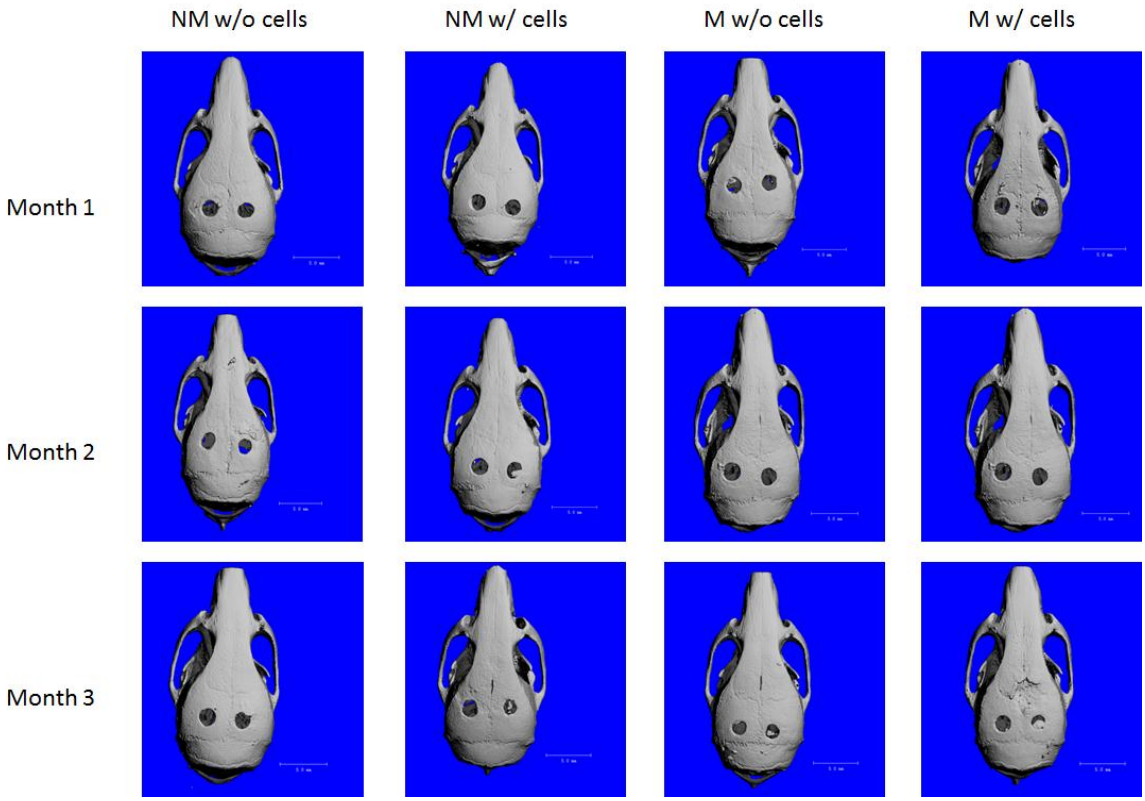

Figure 25. 3D rendered images of MicroCT x-ray data. The labels at the top of the schematic represent the different groups that were implanted as CTS-GP scaffolds without MSCs (NM w/o cells), CTS-GP scaffolds with MSCs (NM w/ cells), CTS-HA-GP scaffolds without MSCs (M w/o cells) and CTS-HA-GP with MSCs (M w/ cells) and the labels to the left of the schematic indicate the time points at wich animals were euthanized and analyzed. It wass observed that the presence of HA on the scaffolds induces significantly enhanced bone regeneration and the presence of cells even further enhances bone regeneration, which can be seen by the formation of new calcified tissue present on the bottom row and the column furthest right.

Harvested specimens were observed under MicroCT imaging to see new bone formation. As can be seen in Figure 25, 3D reconstructions of the x-ray data show that both the incorporation of MSCs onto the scaffolds and the presence of HA in the mineralized scaffolds induces and enhances tissue regeneration at the injury site. As seen in the top row of Figure 25, no new tissue formation had occurred in any of the groups after 1 month. However, by the second month, the presence of moMSCs on both CTS-

GP (NM with cells) and CTS-HA-GP (M with cells) caused a shrinkage in the total area of the wound size (see Figure 26 for quantification). Finally, by the third month, new tissue formation could be observed on all scaffold types except for the CTS-GP scaffolds without cells (NM without cells). The presence of HA and moMSCs caused the defects to become smaller in size and small areas of calcified tissue could be observed in the last row of Figure 25. This new tissue formation was quantified by measuring the area of the defects on each side of the cranium to see how much of the bone was regenerated due to the presence of the scaffolds. The % of healing was determined by taking the area of the defect covered by the mineralized new tissue and normalizing it to the control defect without scaffold. Figure 26 shows that the presence of HA in the CTS-GP scaffolds causes ~6 fold increase in the initiation of wound healing after 1 month (Table 2). By month 2, we began to see the initiation of wound healing on the CTS-GP scaffolds with and without cells (~ a 4 fold increase then was previously observed at 1 month) and the development of improved wound healing with the presence of HA, which showed a 2 fold increase without cells and a 4 fold increase with cells (Table 2). By 3 months, CTS-GP scaffolds without cells show a 2 fold increase from month 2, while the presence of cells on these scaffolds shows an 8 fold increase. In the presence of HA, scaffolds continue to demonstrate improved healing, observed by ~4 fold increase without cells and ~2 fold increase with cells. The final closure sites due to the different scaffold types can be observed in Table 2 and show that CTS-HA-GP scaffolds with moMSCs showed to have the highest wound healing effects. It is also noted that the presence of HA was substantial in initiating wound healing and added greatly to the wound healing process (Table 2).

Table 2. Osteoconductive Properties of CTS-GP with and without HA and cells relative to control holes with scaffolds. The values obtained for each sample are recorded as a percentage of new calcified tissue formation relative to area of the control hole from defects without scaffold implantation. It is observed the significant increase in the presence of HA and further significant increase when cells are present on the scaffolds. A synergistic effect between HA and MSCs is also observed.

Time (months)	CTS-GP without cells (% tissue formation relative to control defect)	CTS-GP with cells (% tissue formation relative to control defect)	CTS-HA-GP without cells (% tissue formation relative to control defect)	CTS-HA-GP with cells (% tissue formation relative to control defect)
1	1.08±0.28	1.89±1.13	5.5±0.73	6.46±0.7
2	4.77±0.8	4.83±1.18	10.79±4.7	23.44±8.4
3	9.98±2.9	32.63±12.16	37.12±4.45	45.55±4.43

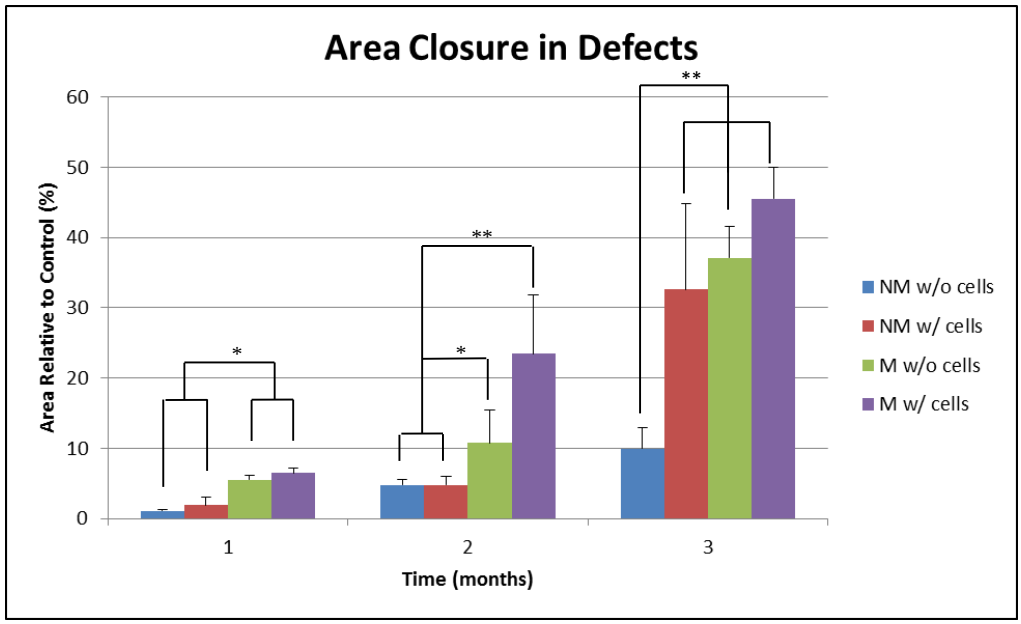

Figure 26. Axiovision software was used to measure the % defect closure due to the presence of the scaffold relative to the control hole in each sample at different time points. It is shown that by the third week, the presence of cells and HA greatly enhance the osteoconductive properties of the CTS-GP scaffolds. * indicates statistical significance with $p<0.05$ and ** indicates statistical significance with $p<0.01$ and n = 4 specimens per group.

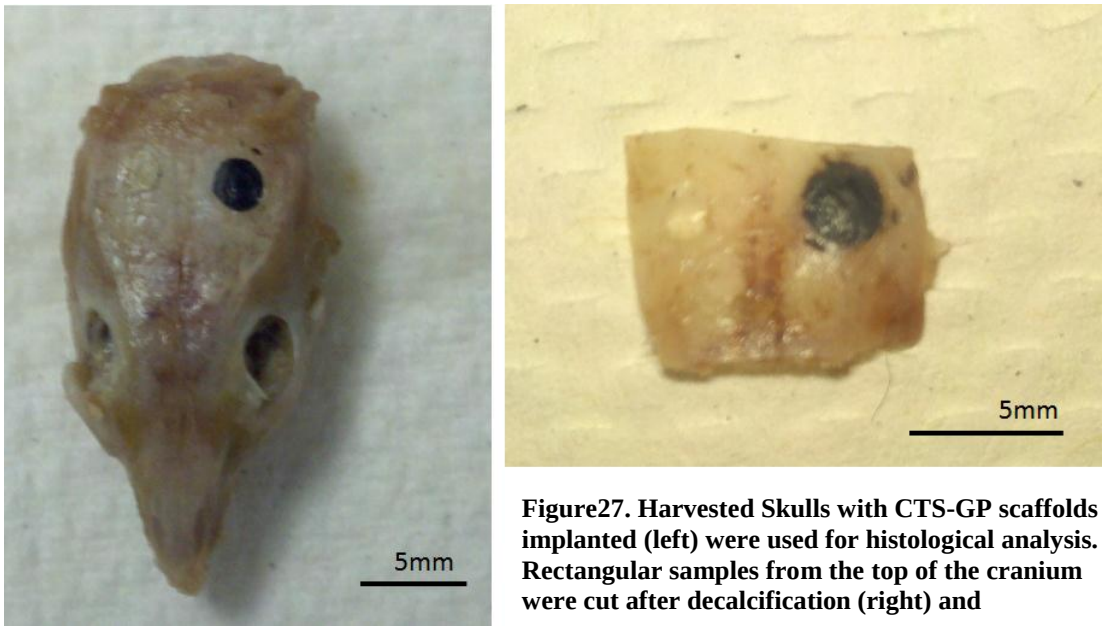

Figure27. Harvested Skulls with CTS-GP scaffolds implanted (left) were used for histological analysis. Rectangular samples from the top of the cranium were cut after decalcification (right) and

To assess osseointegration, i.e. the incorporation of the implanted scaffolds into the host tissue, we used H&E and Masson's Trichrome stains. The microCT data was able to show new bone formation using x-ray imaging which indicates mineralized dense tissue, however, staining allowed us to see how the scaffolds interacted with the tissue at the cellular level and see whether they were truly osteoconductive. Samples (Figure 27 Left panel) were prepared by removing the top of the cranium from the remainder of the skull to yield a square shaped piece of tissue where both wounds were present (Figure 27 Right panel). Shown in Figure 28 is the histology of normal bone tissue as stained by H&E and Masson's trichrome. H&E staining revealed that the scaffolds were in fact interacting with the host tissue with a very minimal amount of immune rejection, as inferred from the lack of infiltrating immune cells and the absence of disorganized fibrous tissue formation at the host/scaffold site (Figure 29A). Control holes where no scaffold was present showed minimal tissue growth, as inferred from the very thin layer of fibrous

tissue grown between the edges of the defect (Figure 29B). Masson's Trichrome staining confirms osseointegration of the, demonstrated by the presence of new tissue (red and blue colors) surrounding remnants of the scaffold (black colors) (Figure 30A). Of note, this tissue forming around the scaffold appeared to be organized tissue, indicative of healthy new tissue rather than the disorganized appearance of fibrous tissue and was devoid of nucleated large cells, indicative of lymphocytes and immune cells due to inflammation and immune rejection. Importantly, in the case of cell-seeded CTS-HA-GP scaffolds, the regions adjacent to the host bone/scaffold junction indicated the presence of endochondral tissue (Figure 30B). Again, the stains also showed that without the scaffold, only a minimal, thin layer of fibrous tissue forms in the defect with no new bone formation (Figure 30C).

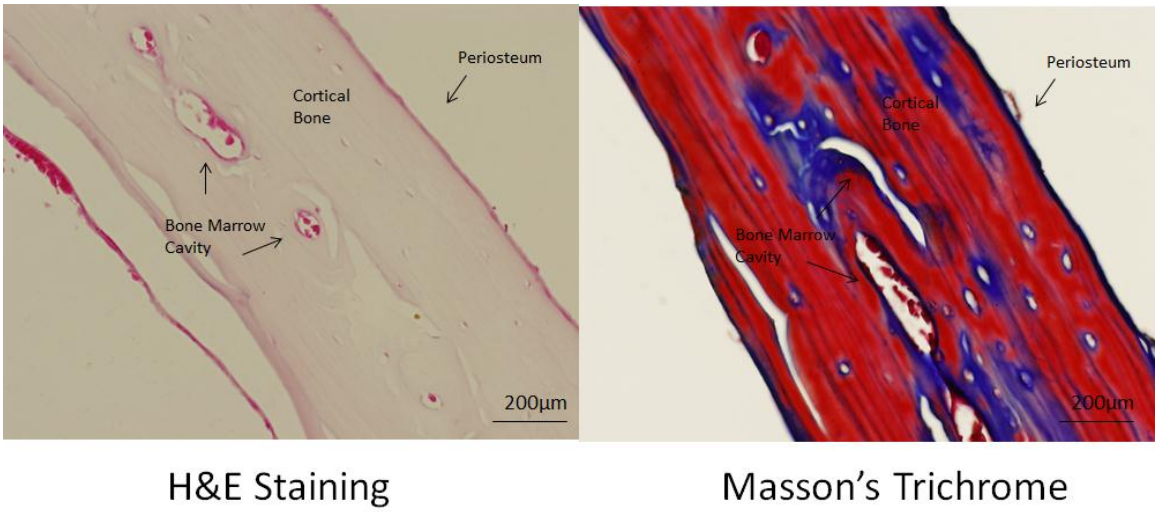

Figure 28. A comparison of H&E staining and Masson's trichrome staining of normal bone tissue. The bone marrow cavities, cortical bone and periosteum are labeled to indicate what these look like in normal tissue for comparison to regenerating tissue areas. Images were taken from non-defective areas of the animal specimens to illustrate normal tissue. Images were taken at taken at 20X.

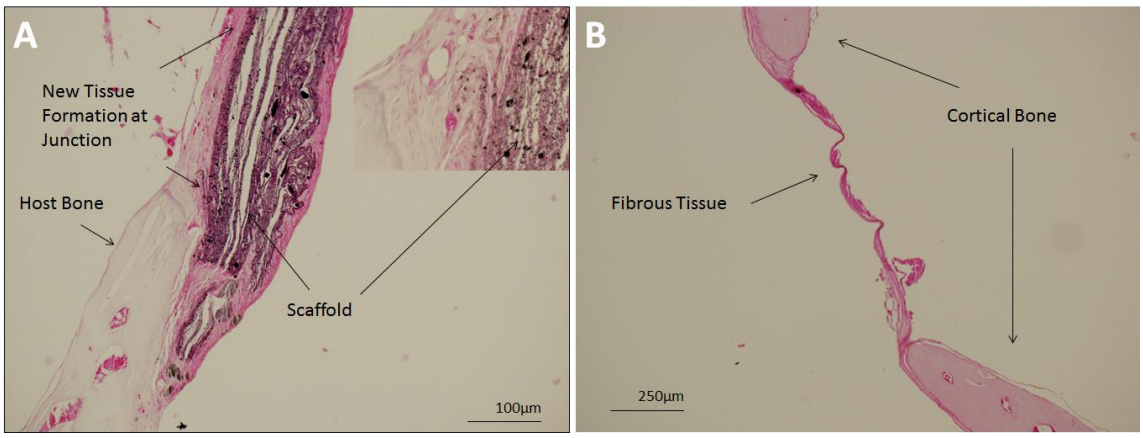

Figure 29. H&E stains show the enhanced tissue formation around CTS-HA-GP scaffolds over control defects. Scaffold/host interactions (A) show good tissue integration and no immunorejection. New tissue formation can be show on the scaffold and the scaffold appears to form a tight junction with the host bone. Fragments of the scaffold can be seen throughout new tissue networks (insert in A) surrounded by regular matrix indicative of new bone formation. Control holes without scaffold (B), show only a minimal amount of fibrous tissue growing in the wound area, indicating that no bone regeneration is occurring. The magnification for the images are 10X (A) and 20X (B).

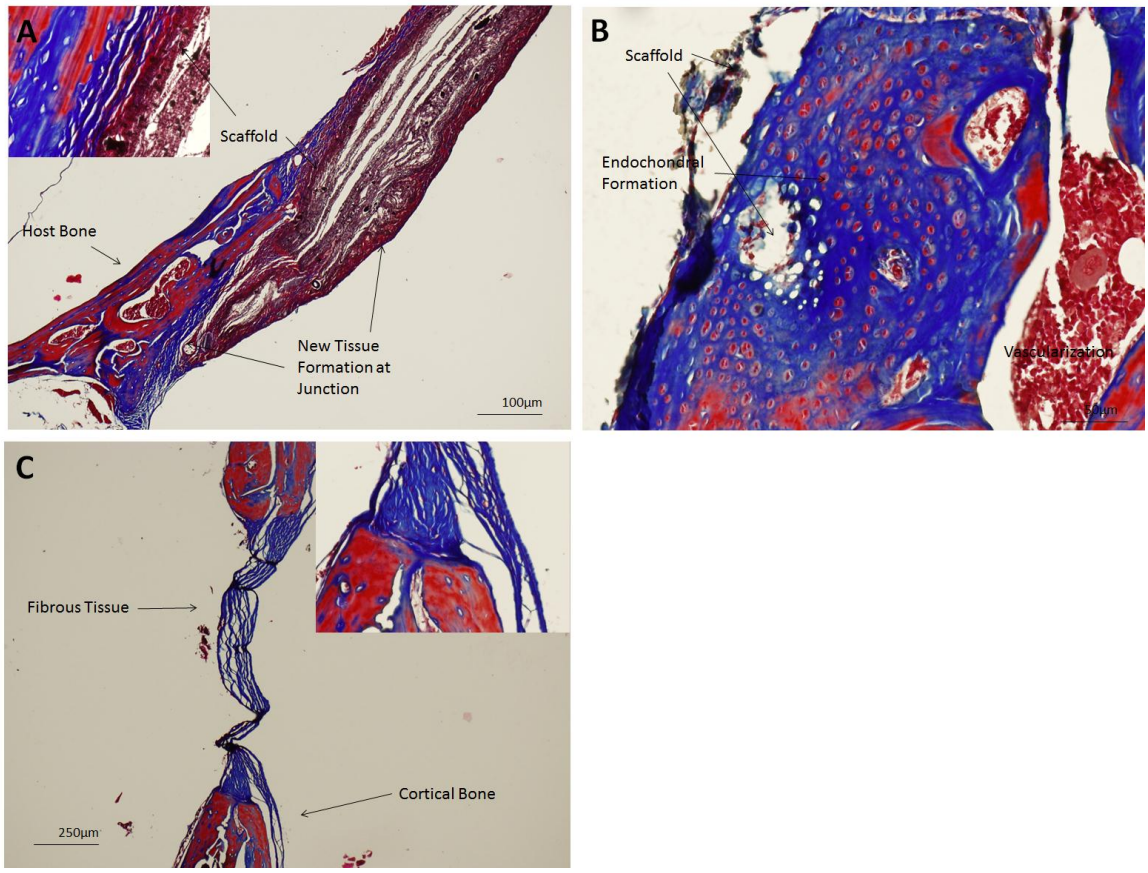

Figure 30. Masson's trichrome stains were used to further characterize the tissue/host interaction. It shows good integration between host tissue and scaffold material (A). Host bone is stained blue (collagen I) and red as normal bone tissue appears. The junction of the tissue and scaffold shows no immunorejection and good integration. New tissue is seen growing along the scaffold edges, indicating that the scaffold is conductive. In the presence of MSCs seeded on the scaffold, endochondral ossification and angiogenesis is observed along where the scaffold surface met the host tissue (B). Remnants of scaffold material can be seen around the endochondral tissue as black fragments. The control defect shows poor tissue formation and just the presence of a small fibrous layer of tissue growing in the defect (C).

6.3 Discussion

Scaffolds developed for tissue engineering should be appropriately tuned in order to closely mimic the native tissue and incorporate specific biological, physical, and chemical cues capable of aiding in the repair and/or regeneration of the target tissue. One of the aims of this thesis was to demonstrate the capacity of electrospun CTS-HA-GP scaffolds, scaffolds to efficiently induce osteogenic differentiation of human

mesenchymal stem cells (MSCs) by combining the inherent biological cues with mimicking the mineralized fibril structure of natural bone tissue and further combining that with the presence of an OGM to introduce chemical induction cues as well. MSCs are lineage-restricted multipotent cells that are derived from the bone marrow, umbilical cord blood or adipose and have the potential to differentiate into bone, cartilage and adipose [108]. Due to technical and ethical issues of embryonic stem cells (ESCs), MSCs are preferentially used for bone tissue engineering [109]. Osteogenic differentiation in early passaged MSCs can be observed based on the cuboidal morphology of the cells, increased ALP activity and the deposition and mineralization of ECM proteins, such as collagen I and HA [110]. Osteogenic growth media supplements include dexamethasone, β-glycerophosphate and ascorbic acid, which have been shown to induce osteogenic differentiation of MSCs via the mitogen activated protein kinase pathway (MAPK) via temporal activation of downstream signaling molecules ERK (upregulation between days 7-11 after induction) and JNK (upregulation 13-17 days after induction) [111] Staining for specific markers, such as STRO-1, CD44 and CD124 indicate that mesenchymal stem cells have not differentiated [112]. The therapeutic effects of MSC for bone deformation can be seen in cases where direct injections of MSC into the bone marrow have induced the production of osteoblasts in order to combat osteogenesis imperfecta [113].

The first major concern with using biomaterials for cell culture and eventual regenerative scaffolds is that they will promote attachment viability and differentiation of different cells types. We showed in chapter 5 that 7F2 cells were capable of proliferating on these scaffolds by seeding at a low density and reaching confluency by week 3. In contrast to this, MSCs seeded at low density on both CTS-GP and CTS-HA-GP scaffolds

did not proliferate well on the scaffolds (Figure 19). We believe that this is attributed to the fact that at low densities, MSC proliferation and migration is stunted due to limited cell-cell contact, which inhibits the cells from spreading and instead allows them to become quiescent. This conclusion is drawn because cell attachment was observed on the scaffolds seeded at low density, but little cell spreading occurred and essentially no cell division. It has been shown that MSCs require cell-cell interactions in order to promote their functionality, whether it is enhancing proliferation or differentiation [114, 115]. In line with this notion, when cells were seeded at higher density, we observed continual cell growth. After 1 week, the cultures essentially reached confluency which was maintained for 3 weeks. The thickness of 3D reconstructions of the cell sheets on the scaffold was 3-fold times higher after 2 weeks when compared to 1 week (Figure 21) and did not increase further at week 3 (not shown). This can either be attributed to cells penetrating into the scaffolds or to cells forming multi-layer sheets on the surface of the scaffolds. Current literature indicates only limited potential for cell penetration into electrospun nanofibrous scaffolds due to the tight packing of the nanofibers during the electrospinning process [116]. Although it is unlikely that the cells are penetrating deep into these scaffolds, the multi-layer stacking indicates that these scaffolds are capable of supporting multi-layer cell sheet formation, which can lead to tissue formation. Studies have also shown that differentiation can also be enhanced by high seeding density. Erickson et. al. (2012) showed that seeding MSCs at high densities into hyaluronic acid gels lead to enhanced chondrogenesis [115]. Another observation at 3 weeks is that the cytoskeleton stained with phalloidin becomes aligned and organized, as opposed to the disorganized arrangement of cytoskeleton seen at 1 week (Figure 20), indicative for

differentiated osteoblasts, which exhibit aligned cytoskeleton organization [117], unlike the irregular arrangement observed in adipocytes. This finding can be taken as another, yet indirect, evidence for the notion that CTS-GP scaffolds may be promoting the differentiation of MSCs towards an osteogenic lineage.

A few previous studies have explored that chitosan nanofibers have the potential to support MSC viability and promote the differentiation of MSCs by creating composite scaffolds containing chitosan and other materials, such as collagen and PLGA [104, 118] but, to our knowledge, no studies have focused on electrospun CTS-HA-GP scaffolds and their effects on MSC viability and osteogenic differentiation. As mentioned in chapter 5, the AB assay can be used to assess metabolic activity of cells growing in culture. Decreases in metabolic activity can be due to loss of cell viability / decrease in cell numbers or to the enhancement of differentiation in culture due to decreased metabolic activity as differentiation increases [50]. By day 10, AB fluorescence shows significant decrease (Figure 22) and plateaus after day 14. As indicated by Figure 20, the cell numbers are not decreasing, so this decrease in metabolic activity is most probably due to the cells starting to transition into a differentiative state. This data is also corroborated by the results shown in Figure 21, where the 3D image showing the formation of multi-layered cell sheets on the scaffolds remains constant from weeks 2 to 3. The notion of enhanced differentiation, ALP activity was further confirmed by measuring ALP activity as an indicator of initial osteogenic differentiation [50]. Our data indicates an enhanced ALP expression at day 21 (Figure 22), which, in conjunction with our AB data, indicates that MSCs are differentiating towards an osteogenic lineage. ALP activity is further enhanced in the presence of an osteogenic medium, indicating that there is an additive

effect between the chemical cues in the differentiation medium and the architectural properties of the electrospun scaffolds. By taking these three independent observations of a) maintenance of confluent, multi-layered cell sheets between 2 and 3 weeks, b) plateauing of AB fluorescence between weeks 2 and 3 and c) indication of an additive effect between the physical structure of electrospun scaffolds, the biochemical effect from the presence of HA and the chemical cues initiated by the OGM, we have shown that CTS-HA-GP scaffolds promote cell adherence and viability and that they can help to stimulate osteogenic differentiation. Without initiation into a differentiative state, MSCs will become quiescent if allowed to reach complete confluence [119]. We surmise that without the biochemical differentiative cue from HA nanoparticles or the chemical cues from the osteogenic medium, MSCs grown on CTS-GP scaffolds will not undergo substantial differentiation and will most likely become quiescent. However, when osteogenic medium or HA are present, the cells differentiate towards the osteogenic lineage, as shown by the enhanced activity of ALP. Further, an additive effect was noted when the two were used together.

The physical and mechanical properties of biomaterials are important factors when dealing with osteogenic differentiation and integration. The topographical properties of micro and nanoscale grooves and pits as well as the incorporation of hydroxyapatite, zinc and other naturally occurring inorganics in the body lead to enhanced spreading and production of osteoblasts [120]. Similarly, osteopontin expression is upregulated during mechanotransduction of scaffold-cell interactions, indicating that stiffness and strength can be used to promote osteoblasts to deposit mineralized matrix and begin remodeling. This occurs via a decrease in DNA methylation at the osteopontin promoter binding site

leading to an increase in osteopontin and osteogenic expression [121]. The progression of the osteogenic differentiation process can also be monitored temporally, given that many factors involved in cell-ECM signaling during differentiation are present at different stages and involved in mineral deposition. For example, ALP, a cell-surface glycoprotein that is crucial for the initiation of mineralization, is present early on; its upregulation signals the initiation of matrix mineralization. Osteopontin is secreted and bound to an integrin receptor to regulate mineralization during maturation. Osteocalcin regulates the activity of osteoclasts and is a post-proliferative marker of osteoblast differentiation [122].

Along with osteoinduction, it is also important to demonstrate the ability of our biomaterials to induce osseointegration. Generally, osteogenic materials will also be osteoconductive and promote not only the migration of host cells into the construct, but also initiate the processes of bone development and regeneration at sites where it would otherwise not occur. *In vivo* regeneration of critical size defects requires the use of autografts, allografts or bioactive synthetic materials that can initiate substantial bone regrowth. Autografts are limited in supply and require a secondary operative site that is usually linked with donor site morbidity and chronic pain [123] . Allografts often fail to induce bony ingrowth due to the lack of functional cell-allograft interaction and the absence of a periosteal layer containing osteoprogenitor cells. Synthetic materials also tend to be only osteoconductive because of the lack of a biological component [23]. This has been shown in a number of studies where the inclusion of growth factors or a cellular population is required to see sufficient bone growth in animal models [124-128]. Hence there is an unmet clinical need for a new, viable bone substitute material that is

marketable as an off-the shelf- product and which is osteoinductive as well as osteoconductive.

An appropriate tissue scaffold will demonstrate two distinct properties: 1) the ability to induce host tissue migration and 2) a minimal amount of immune rejection from the host. As mentioned in chapter 2, the crucial induction of bone tissue regeneration and healing is attributed to osteoprogenitor cell migration from the periosteum [21, 23, 26, 28]. Critical size defects in bone injuries do not effectively heal because there is no tissue in the defect area for the osteoprogenitor cells to migrate onto in order to begin depositing matrix and initiate healing [23]. Biomaterials can be used to bridge this gap and provide a template to allow for the healing process to begin. Electrospun scaffolds offer a high surface-area-to-volume ratio to promote migration from the periosteum and induce osteogenesis.

To test the osteoconductive and osseointegrative properties of our biomaterial, calvarial defects were surgically created in mice and treated with CTS-GP and CTS-HA-GP scaffolds either with MSCs seeded onto the scaffold prior to implant or without cells. Scaffolds containing cells were seeded 2 days prior to implantation with naïve MSCs that remained undifferentiated at the time of implant. This has certain advantages to seeding with osteoblasts. While osteoblasts are responsible for depositing the new matrix during wound healing, naive MSCs release factors that promote cell proliferation and migration in other cell types, e.g., as observed by the enhanced chondrocyte proliferation in the presence of MSCs [114], or by the increase in cartilage formation in the presence of undifferentiated MSCs *in vivo* [115]. No studies have observed the effects of osteoprogenitor cell migration into allograft scaffolds with undifferentiated MSCs to

date. Critical size defects of 2.1mm were drilled to ensure no spontaneous bone regrowth in untreated wounds [8]. At each specific time point, host/scaffold interactions were observed using histology and calcified tissue formation was observed using microCT imaging. On untreated wounds, fibrous tissue growth was observed, which is due to adverse immune response and exhibits an irregular matrix formation and the characteristic presence of numerous inflammatory cells [129, 130]. The tissue growing on and in the scaffold here is shown to have oriented matrix formation and is stained blue in the masson's trichrome stain, which is indicative of collagen I, the main ECM component of newly forming bone tissue (Figures 29 and 30) [131]. This newly assembled tissue is growing around remnants of the scaffold that are indicated by the black amorphous fragments in Figure 30. To our knowledge, this is the first study to demonstrate the ability of CTS-GP scaffolds to induce tissue ingrowth around a bone injury model.

The main developmental process for bone tissue formation in the skull is intramembranous ossification [19, 20, 132]. In this process, osteoblasts form numerous ossification centers, which spread out to form the calcified bone tissue of the skull. As seen in Figure 30B, implantation of our cell seeded scaffolds seems to reproduce a different developmental process in that endochondral tissue formation can be observed by the third month following implantation. However, this is in contrast to the normal process of bone formation in the skull and may have some interesting implications. We speculate that the implanted MSCs are recruiting osteoprogenitor cells from the surrounding periosteal tissue and induce chondrogenic differentiation via cell-cell signaling from the host tissue as observed by the formation of endochondral tissue

(Figure 30B). Given that the cells residing in the periosteum are multipotent and can differentiate towards osteogenic or chondrogenic lineages [21] and that undifferentiated MSCs have the potential to enhance both chondrogenesis and osteogenesis [114, 115], signals from the host tissue may be inducing the earlier stages of chondrogenesis either in the cells seeded on the scaffold prior to implantation or in the host cells recruited to the implant site This may lead to a new way of generating cranial tissue, via endochondral ossification rather than intramembranous ossification. Recent studies have indicated that endochondral ossification can be seen between implanted PLGA/PCL wet-electrospun fibers and host bone junctions as an improved method of bone regeneration over the normal intramembranous ossification process [133] indicating that electrospun CTS-GP scaffolds may act as a promising template to promote endochondral ossification in cranial regeneration.

The occurrence of de novo tissue formation around the scaffold (Figures 29 and 30) is a positive indication that these scaffolds are permissive and promote proper host integration without immune rejection and also show that there is sufficient tissue growing into the scaffold, as also confirmed by MicroCT, indicating presence of mineralized tissue and the initiation of osteogenic regeneration. While tissue integration and immunosuppression are of upmost concern, the end goal is to have a scaffold that is osteoconductive. Our MicroCT results suggest that the presence of cells and the presence of HA greatly enhances the osteogenic capacity of these scaffolds and leads to mineralized tissue formation by month 3. Quantitatively there is up to a 5 fold increase in ”healing” over CTS-GP scaffolds without HA and MSCs (Figure 29). Combined with the findings of endochondral tissue formation on CTS-HA-GP scaffolds after 3 months of

implantation, we can conclude that this de novo generated tissue is in the early stages of endochondral ossification and that mineralized ECM is beginning to replace cartilage tissue.

The presence of MSCs or other permissive biological components, such as HA, will greatly enhance the osteogenic capacity of an implanted scaffold due to the signals secreted by cells or the endogenous factors that promote cellular responses *in vivo* [2, 129, 134, 135]. Current treatments for osteogenic injuries or disabilities use bone cements, metal or inert implantable replacement materials or autografts [23, 88]. While the latter is preferable due to the functional periosteal layer which can induce osteogenic healing, the former two lack cellular components and do not induce regeneration. For this study, we were able to show that the presence of HA causes a significant increase in osteogenic capacity over CTS-GP scaffolds that lack HA, indicating its inductive properties and biochemical cues are of upmost importance for osteogenesis. We hypothesize that osteoprogenitor cells in the periosteum come in contact with the surface of this material when it is placed over top of the defect and respond to the biomimetic propensities of this scaffold including it mechanical properties and the presence of HA [50, 64, 136]. The presence of MSCs induces endochondral tissue formation leading to osteogenesis with time and further enhances mineralized tissue formation.

Chitosan has been used in a variety of biomedical applications for its beneficial properties, including its innate ability to suppress immunorejection [5, 72, 75, 137-139]. Here, we have demonstrated not only the ability to act as a biocompatible material, but also its ability to induce osteogenesis. In the past, chitosan has been incorporated into bone replacement materials in order to enhance the cell attachment on less adhesive

materials [5, 135, 138, 140], but such materials still act as replacement scaffolds and not regenerative materials. Although replacement is one short-term remedy for bone fracture and defect, many of these materials have long-term complications and fail ultimately. The shift of tissue engineering over the past decade has gone from replacement to regeneration, encouraging the development and use of f regenerative materials such as CTS-HA-GP scaffolds fabricated via electrospinning. Not only have many studies shown the *in vitro* capacity of electrospun scaffolds to be osteoinductive ([36, 50, 88, 141]), but we have now demonstrated the potential of such scaffolds to bridge the gap in critical size bone defect in a mouse model of craniofacial injury.

Chapter 7. **A Proof of Concept Study: Fabrication and Evaluation of Electrospun PLGA Scaffolds with Enhanced Porosity from Sacrificial Fiber Removal**

7.1 **Fabrication of Porous PLGA Scaffolds**

To fabricate porous electrospun scaffolds, a sacrificial material was concomitantly electrospun with PLGA and subsequently removed. The set up can be seen in Figure 31. Briefly, the two solutions were loaded into two different syringe pumps and simultaneously electrospun onto the rotating collector at a 1:1 ratio with varying concentrations of gelatin. PLGA fibers were stained with DiI and fluoresce red. Gelatin fibers were stained with DiO and fluoresce green, which can be seen at different concentrations in Figure 32 A, B and C.

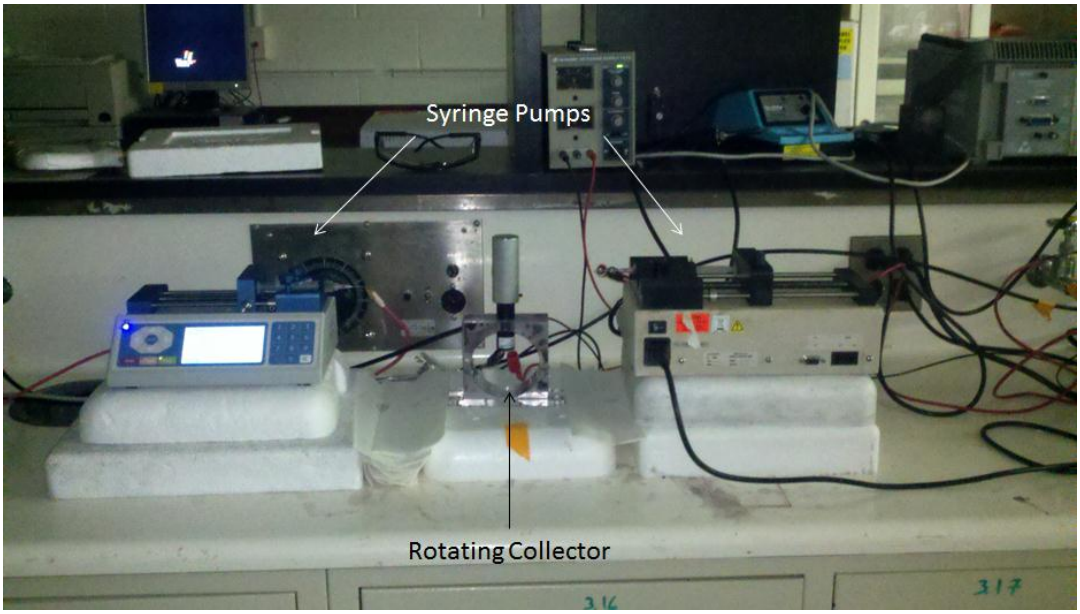

Figure31. A dual electrospinning set up was put together to synthesize scaffolds containing two different materials. The syringe pumps were placed on either end of a rotating collector and loaded with their respective polymer solutions. The collector was rotated at ~20RPM to evenly collect fibers from both materials simultaneously.

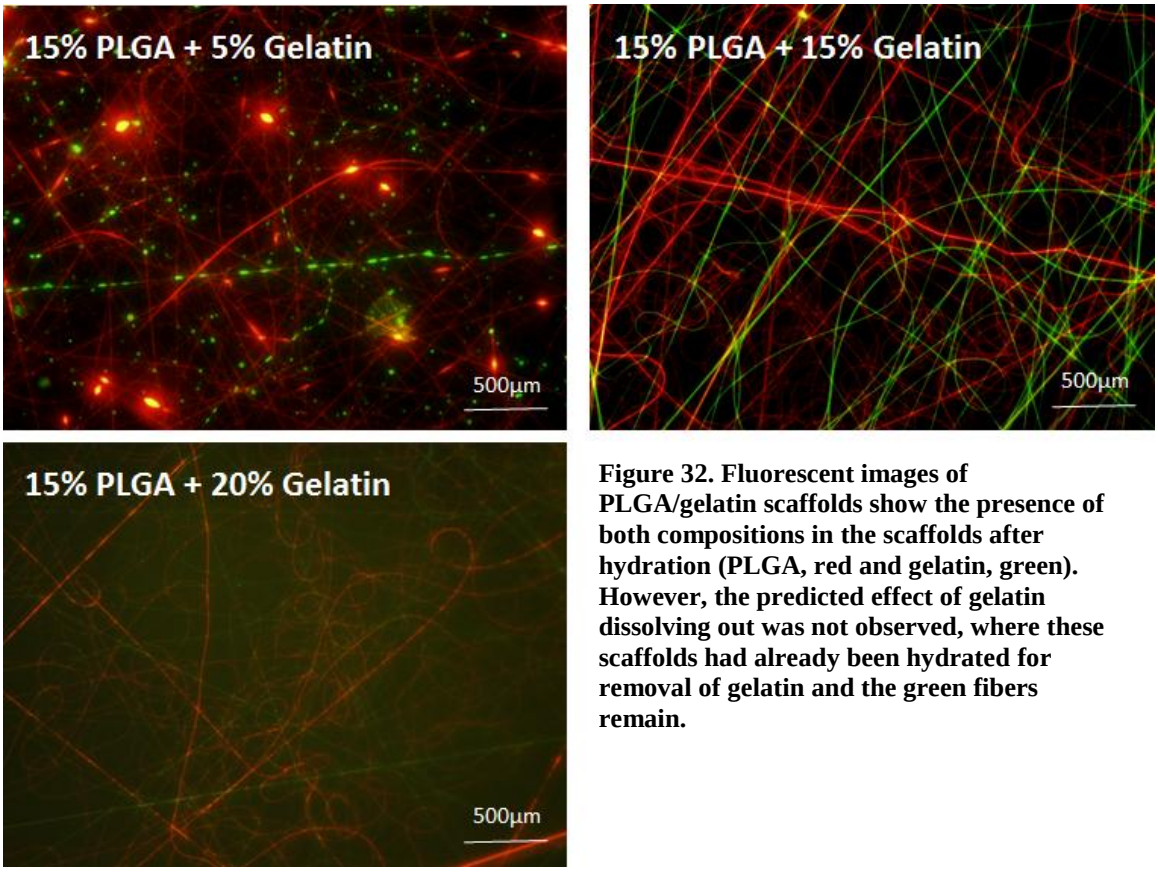

Figure 32. Fluorescent images of PLGA/gelatin scaffolds show the presence of both compositions in the scaffolds after hydration (PLGA, red and gelatin, green). However, the predicted effect of gelatin dissolving out was not observed, where these scaffolds had already been hydrated for removal of gelatin and the green fibers remain.

An optimal scaffold for a tissue like bone needs to not only have ideal porosity, but also needs to have ideal mechanical properties. We performed tensile testing with pure PLGA scaffolds as well as with scaffolds generated from 1:1 ratio working solutions of 15% PLGA and 5%, 15% or 20% gelatin after removal of the water-soluble gelatin by immersion into a water bath and calculated the Young's moduli and UTS from each different type of scaffold. The results indicate that mechanical properties are greatly affected by the presence of gelatin in a logarithmic trend. The young's moduli and ultimate tensile strength of different scaffold conditions can be seen below in

Table 3.

Table 3. Mechanical Properties of varying concentrations of gelatin in PLGA scaffolds.

Scaffold Conditions	Young's Modulus (MPa)	Ultimate Tensile Strength (N)
15% PLGA	2101.57±702.98	36.81±11.05
15% PLGA + 5% Gelatin	113.95±22.45	6.71±1.52
15% PLGA + 15% Gelatin	3.19±1.11	0.43±0.06
15% PLGA + 20% Gelatin	56.12±16.8	3.93±0.47

7.2 Cell Infiltration Into the Porous Scaffolds

We hypothesized that rhe removal of gelatin will increase the porosity and internal surface area of the scaffolds by inducing larger pores and allowing cell growth in three dimensions rather than just on the surface of the scaffolds. One important method of looking at biological patterns like cell growth is by using mathematical models to predict the behavior. In order to model cell growth on our scaffolds, we adapted a model from

Lemon et. al. in which they modeled MSC proliferation on porous scaffolds as a function of ECM deposition and oxygen tension [142]. The model is derived as follows:

$$\frac{dv_{stem'}}{dt} = k_{s's'}\, v_{ecm} v_{stem'}\, v_{void} - k_{s's''}\, v_{stem'} \quad (1)$$

describes the rate of change of undifferentiated MSC where $v_{stem'}$ is the volume fraction of undifferentiated MSCs, $k_{s's'}$ is a rate constant for MSC proliferation, v_{ecm} is the volume fraction of ECM deposited by MSCs, v_{void} is the volume fraction of uninhabited space in pores and $k_{s's''}$ is a rate constant for ECM production. The next part of the system is

$$\frac{dv_{stem''}}{dt} = k_{s''s''}\, v_{ecm} v_{stem''}\, v_{void} + k_{s's''}\, v_{stem'} \quad (2)$$

which describes the rate of change of differentiated MSC where $v_{stem''}$ is the volume fraction of differentiated MSCs and $k_{s''s''}$ is a rate constant for MSC differentiation. The final part of the system is

$$\frac{dv_{ecm}}{dt} = \left(k_{es'}\, v_{stem'} + k_{es''}\, v_{stem''}\right) v_{void} \quad (3)$$

where v_{ecm} describes the rate of change of ECM.

The first terms on the right hand side of the first equations 1 and 2 represent cell proliferation while the second terms represent differentiation. The rate of proliferation is taken to be proportional to v_{ecm} to model the stimulation of MSC proliferation by the AB assay. The right hand side of the third equation has both differentiated and undifferentiated cells contributing to ECM synthesis. To model a contact inhibition effect whereby growth of the tissue ceases once the pores have been filled, the rate of cell

proliferation and ECM synthesis is taken to be proportional to v_{void}, this being the volume fraction of free space inside the scaffold pores. Thus equation 4 is derived as follows,

$$v_{void} = 1 - \left(v_{scaff} + v_{stem'} + v_{stem''} + v_{ecm}\right) \tag{4}$$

where v_{scaff} is the volume fraction of the scaffold and is related to the scaffold porosity by

$$v_{scaff} = 1 - \frac{p}{100} \tag{5}$$

where p is porosity.

According to Grayson et. al. cells tend to stop proliferating well before pores are filled, indicating that there is some sort of inhibitory effect that is currently unclear [143]. However, being that this is observed, a factor for effective carrying capacity of the scaffold must be employed and can be expressed a

$$v_{void} = v_{eff} - \left(v_{stem'} + v_{stem'}, + v_{ecm}\right) \tag{6}$$

where $v_{eff} \leq 1 - v_{scaff}$ and v_{eff} is the effective carry capacity, which takes into account the free space in the pores of the scaffold. This parameter of carrying capacity is related to cell proliferation due to the observation by Grayson et. al. stated above as well as to the fact that pores are empty voids in the scaffold. Cells can only grow on the inner surface of these pores, but not in the free space accounting for the center of the pore with no surface contact for cells. This equation gives a more adequate representation of cell growth rather than just accumulating for the complete presence and size of pores in the scaffold.

The initial three equations for undifferentiated, differentiated stem cells and ECM are to be expected at the initial conditions with $v_{stem'} = v_{stem',0}$, $v_{stem''} = v_{stem'',0}$ and $v_{ecm} = 0$ at $t = 0$. By making the assumptions that differentiation causes no change to cell properties such as size, proliferation rate or viability (simplifying to an easily workable model for prediction), we simplify as follows with $k_{s's'} = k_{s''s''} = k_s$ and $k_{es'} = k_{es''} = k_{es}$ and by adding $v_{stem'} + v_{stem''} = v_{stem}$ we can obtain the system of equation:

$$\frac{dv_{stem}}{dt} = k_s v_{ecm} v_{stem}\left(v_{eff} - v_{stem} - v_{ecm}\right) \tag{7}$$

$$\frac{dv_{ecm}}{dt} = k_{es} v_{stem}\left(v_{eff} - v_{stem} - v_{ecm}\right) \tag{8}$$

We can solve these equations by setting the initial conditions $v_{stem} = v_{stem',0} + v_{stem'',0} = v_{stem,0}$ and $v_{ecm} = 0$ at $t = 0$.

Applying the chain rule to these 2 equations yields the differential equation

$$\frac{dv_{stem}}{dv_{ecm}} = \frac{k_s v_{ecm}}{k_{es}} \tag{9}$$

which is integrated to give

$$v_{stem} = v_{stem,0} + \alpha v_{ecm}^2 \tag{10}$$

where $\alpha = \frac{1}{2} k_s / k_{es}$ which can then be substituted into dv_{ecm} for

$$\frac{dv_{ecm}}{dt} = k_{es}\left(v_{stem,0} + \alpha v_{ecm}^2\right)\left(v_{eff} - v_{stem,0} - v_{ecm} - \alpha v_{ecm}^2\right) \tag{11}$$

which can be solved explicitly, for example, by the method of partial fractions giving:

$$t = \frac{1}{\alpha k_{es}}\left[f_1 log_e\left(\frac{C_1}{C_1+v_{ecm}}\right) + f_2 log_e\left(\frac{C_2}{C_2+v_{ecm}}\right) + f_3 log_e\left(\frac{C_3}{C_3+v_{ecm}^2}\right) + f_4 tan^{-1}\left(\frac{v_{ecm}}{\sqrt{C_3}}\right)\right] \quad (12)$$

where

$$C_1 = \frac{1}{2}\alpha^{-1}\left(1 - \sqrt{1 + 4\alpha\left(v_{eff} - v_{stem,0}\right)}\right) \quad (13)$$

$$C_2 = \frac{1}{2}\alpha^{-1}\left(1 - \sqrt{1 + 4\alpha\left(v_{eff} - v_{stem,0}\right)}\right) \quad (14)$$

$$C_3 = \alpha^{-1} v_{stem,0} \quad (15)$$

$$f_1 = -(C_3 + C_1^2)^{-1}(C_1 - C_2)^{-1} \quad (16)$$

$$f_2 = -(C_3 + C_2^2)^{-1}(C_1 - C_2)^{-1} \quad (17)$$

$$f_3 = -\frac{1}{2}(C_1 + C_2)(C_3 + C_1^2)^{-1}(C_3 - C_2^2)^{-1} \quad (18)$$

$$f_4 = -(C_1 C_2 - C_3)(C_3 + C_1^2)^{-1}(C_3 + C_2^2)^{-1} C_3^{-1/2} \quad (19)$$

With $f_{1\text{-}4}$ and $C_{1\text{-}2}$ are arbitrary constants for simplification and solution. The volume fractions of undifferentiated and differentiated cells can be determined as follows by combining $v_{stem'}$ and v_{stem} to give

$$\frac{1}{v_{stem'}}\frac{dv_{stem'}}{dt} = \frac{1}{v_{stem}}\frac{dv_{stem}}{dt} - k_{s's''} \quad (20)$$

which is integrated with respect to time using the initial conditions to give

$$v_{stem'} = \left(v_{stem',0}/v_{stem,0}\right) v_{stem} e^{\left(-k_{s's''}t\right)} \quad (21)$$

and using $v_{stem} = v_{stem'} + v_{stem''}$ it follows that

$$v_{stem''} = v_{stem}\left[1 - \left(v_{stem',0}/v_{stem,0}\right)e^{\left(-k_{s's''}t\right)}\right] \quad (22)$$

By solving for the system above, it can be shown that $dt/dv_{ecm} < 0$, thus given a particular value of t, there can be only one value of v_{ecm}. By substituting this solution into equation 10 gives the value of v_{stem} at that value of t. The equilibrium value for v_{ecm} denoted as $v_{ecm,ss}$ can be calculated by setting the right hand side of equation 11 to zero, yielding the quadratic equation

$$\alpha v_{ecm,ss}^2 + v_{ecm,ss} + v_{stem,0} - v_{eff} = 0 \quad (23)$$

whose positive solution using the quadratic formula is

$$v_{ecm,ss} = -C_1 = k_s/k_{es}\left(\sqrt{1 + 2k_s/k_{es}\left(v_{eff} - v_{stem,0}\right)} - 1\right) \quad (24)$$

The equilibrium for v_{stem} is then $v_{stem,ss} = v_{eff} - v_{ecm,ss} = v_{eff} -$

$$k_s/k_{es}\left(\sqrt{1 + 2k_s/k_{es}\left(v_{eff} - v_{stem,0}\right)} - 1\right) \quad (25)$$

Lemon et. al. observed the differences of cell migration into scaffolds as a function of different oxygen tensions. Here, we adapted their model to see the effect of varying gelatin concentrations in PLGA scaffolds on MSC migration [142]. Using MatLab code, we obtained the predictive model based on the data generated by Lemon et. al. and reproduced the volume fraction of ECM production in their scaffold (Figure 33), which then enabled us to predict the volume fraction of MSCs in our scaffold (Figure 33). These graphs were generated from the experimental values from the Lemon et. al. paper, where cell dimensions and scaffold parameters were taken from from Grayson et. al.

[144] Briefly, volume fraction of cells was calculated as the number of cells seeded times the volume of a typical MSC (spherical with a 20μm diameter, giving a volume of 4.18mm^3) divided by the volume of the scaffold. Using their equations and our consistent scaffold diameter of 10.3mm, we generated the volume fraction of cells for our scaffolds.

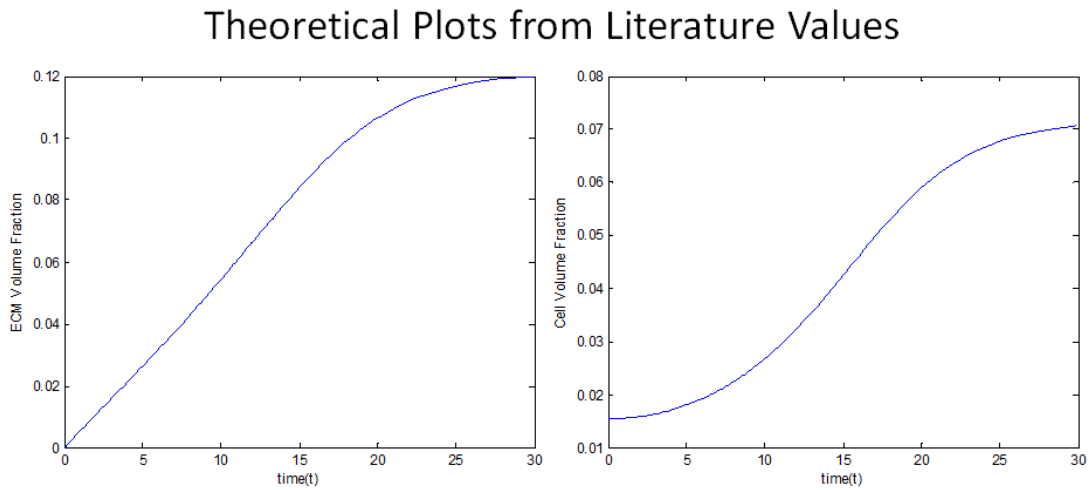

Figure 33. Theoretical curves of the volume fractions of ECM production and cells over time to illustrate a predictive model of cell proliferation and ECM production over time as a function of the total volume of a cellular scaffold construct.

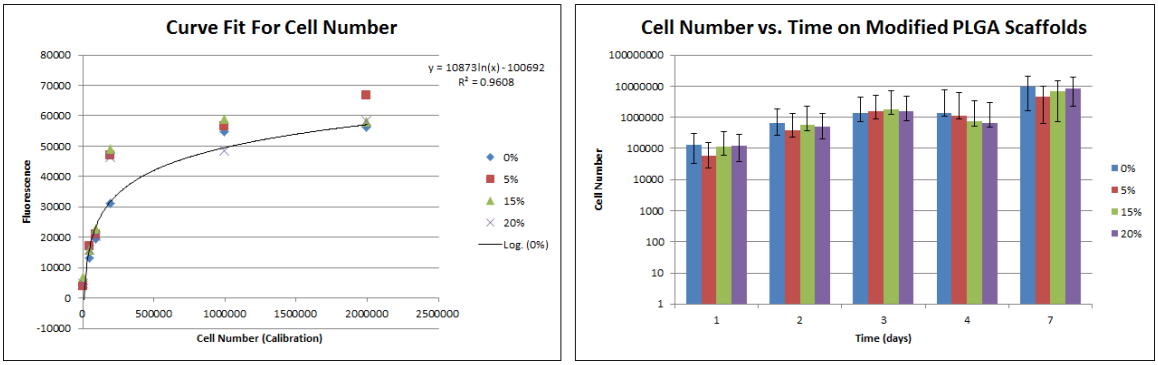

Figure 34. A logarithmic curve fit was used to determine the equation used to convert AB fluorescence to cell number. Cell number was then plotted vs. time to show the effects that gelatin had on growth rate of moMSCs.

To actually meansure how the cells proliferate on the porous scaffolds as compared to the model predictions, we monitored cell viability/cell numbers using AB assays on the different scaffold conditions over a 1-week period. A calibration curve was plotted so that fluorescence could be converted into cell number and compared to the model directly. Using an exponential curve fit (Figure 34, left panel), we could obtain cell numbers at the different scaffold contents over time. We then generated predictive curves using our obtained data and the lsqcurvefit function on MatLab and fitted our data to this function to generate the carrying capacity, cell volume fractions and the rates of ECM production and cell growth into the electrospun scaffolds (Figure 35, left panel). The data (Table 4) was highly variable, indicating that the volumetric curve fit was not appropriate for this model. We then fitted the data to a simpler logistic growth curve using $P(t) = \frac{kP_0e^{rt}}{k+P_0(e^{rt}-1)}$ and the cftool function in MatLab that would be indicative of cells growing on a 2D substrate, i.e. the surface of the scaffold. When fitting the data to this model (Figure 35, right panel) a much better fit was obtained and much more indicative values as well (Table 5).

Table 4. Specific values of carrying capacity and rates of ECM production and cell growth obtained by cell number data. These values were obtained by fitting to the porous scaffold model from Lemon et. al.

	Values Obtained When Fitting to the Porous Scaffold Model				
Gelatin	Resnorm (Noise Ratio)	Carrying Capacity (V_{eff})	Initial Volume Fraction ($V_{stem,0}$)	Rate of ECM Production (k_{es})	Rate of Cell Growth (k_{ss})
0%	0.1672	0.6833	0.0695	3.9226	4.5971
5%	0.2105	0.4821	0.0396	4.2417	24.864
15%	0.5104	0.4065	0.0552	3.8224	14.8577
20%	0.5853	0.7553	0.0579	4.4255	2.9395

Table 5. Carrying capcity and cell growth rate values obtained by fitting the cell number data to a logistics growth curve. These data proved to be a better representation of biological function.

Values Obtained When Fitting to the Logistic Growth Model			
	Carrying Capacity (k)	Initial Volume Fraction (P0)	Rate of Cell Growth ®
0%	0.199	0.044	0.846
5%	0.1799	0.01765	1.324
15%	0.1854	0.03971	0.9296
20%	0.1931	0.0493	0.7

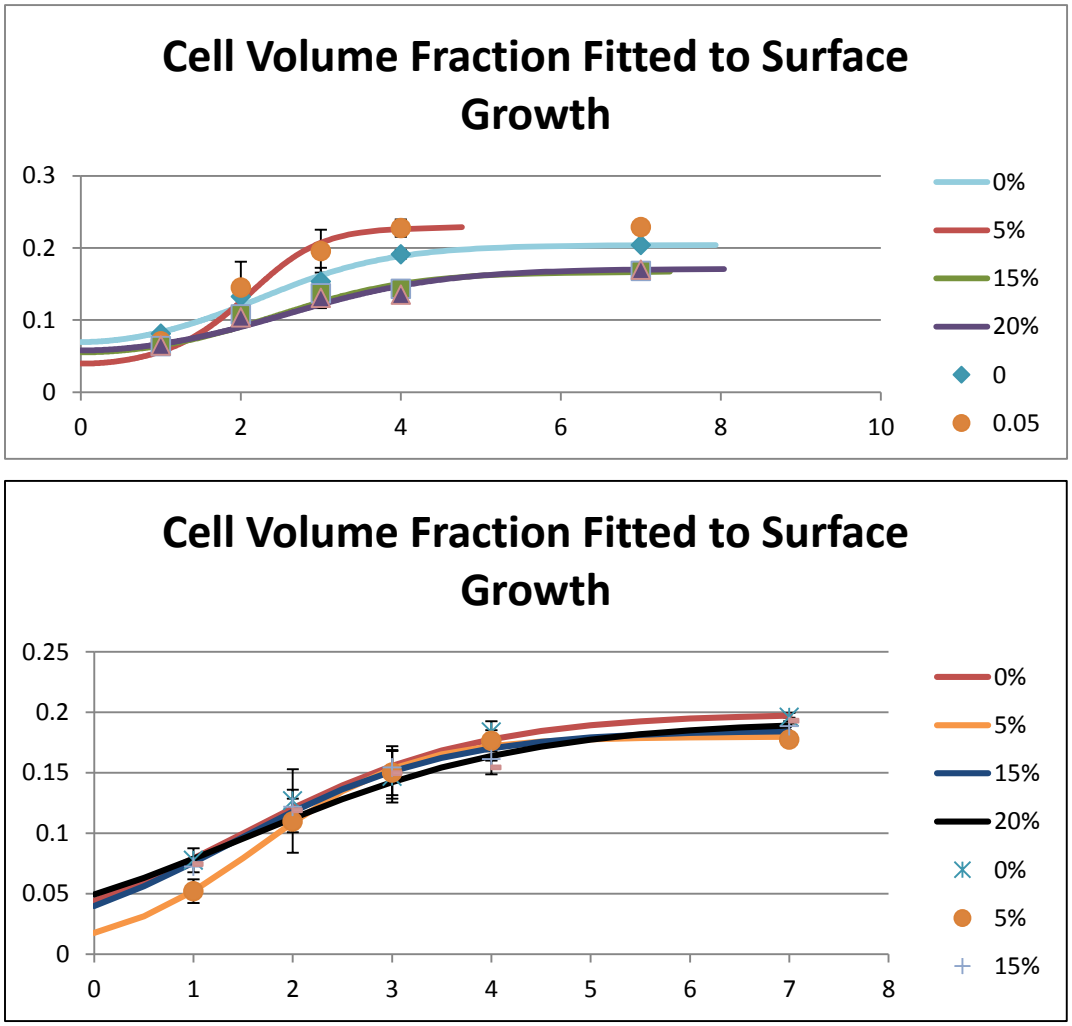

Figure 35. Using the model for cell volume fraction in the porous scaffolds derived from Lemon et. al. we were able to fit the data to a predictive curve (top panel). However, the interpreted data generated (Table 4) shows that the values for the effective carrying capacity and the rate of cell growth were not reliable or reproducible, indicating that this model did not accurately represent the data. To adjust, a logistic growth model was used to model how the cells would behave growing on the surface of the scaffold in 2D and fitted to the data (bottom panel). The values recorded for this fit (Table 4) were much more interpretative to the data, indicating that the cells are not infiltrating the scaffold and still remain growing on the surface.

In trying to understand why this porosity model did not apply to the cells, we evaluated the fiber morphology and the presence of newly formed pores due to gelatin removal using SEM (Figure 36A, B and C). As seen in these images the gelatin fibers do not appear to be completely removed, as also indicated by fluorescent microscopy. Macroscopic images indicate that the gelatin fibers are changing morphology and becoming more gel-like rather than maintaining their fibrous structure (Figure 37A, B and C). This is especially noticed at a concentration of 15% gelatin (Figure 37C) where the scaffold becomes translucent and forms a gel rather than an electrospun fibrous mat. At 5% and 20%, (Figure 37B and D respectively) the fibrous macrostructure is maintained, however the Youngs moduli and UTS display a significant decrease from those of PLGA alone (Table 3), indicating that the gelatin induces a substantial structural change and mechanical decrease after hydration. As the gelatin appears to remain in the scaffold after wetting, the introduction of water may allow for softer, gel-like structures to incorporate on/around the PLGA fibers.

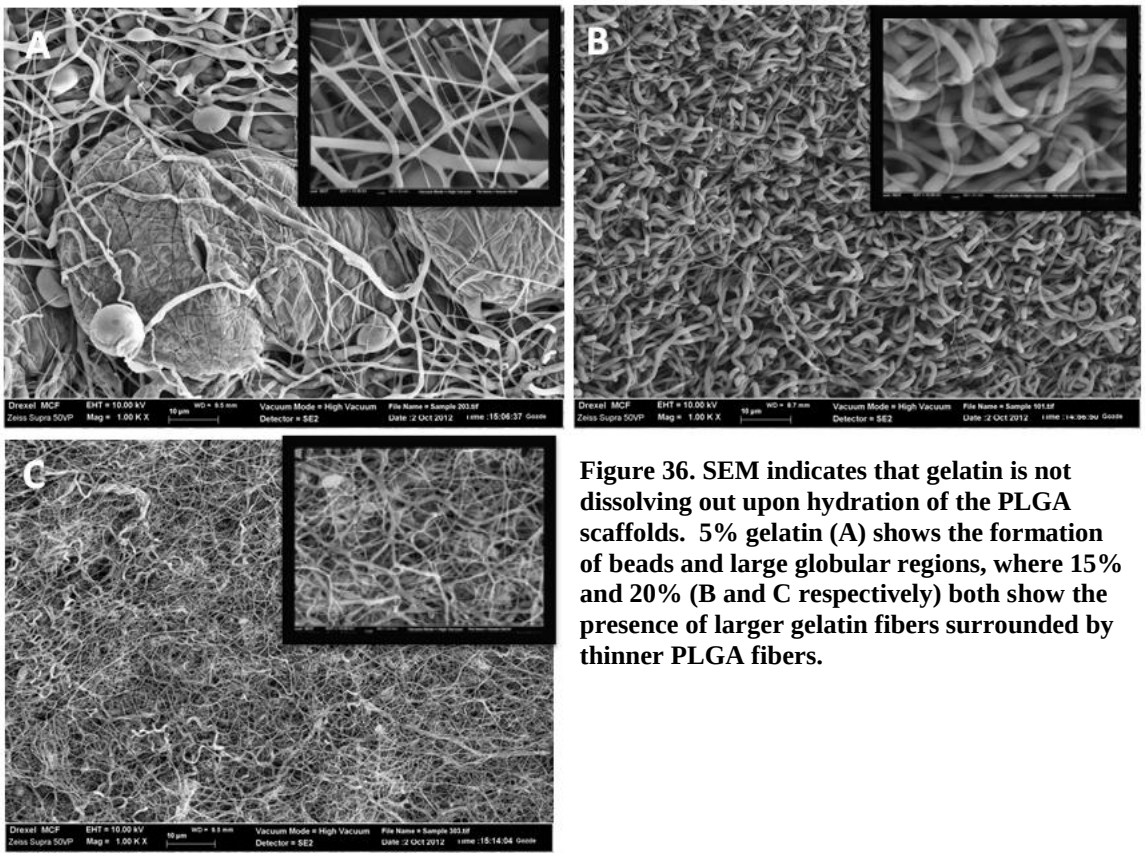

Figure 36. SEM indicates that gelatin is not dissolving out upon hydration of the PLGA scaffolds. 5% gelatin (A) shows the formation of beads and large globular regions, where 15% and 20% (B and C respectively) both show the presence of larger gelatin fibers surrounded by thinner PLGA fibers.

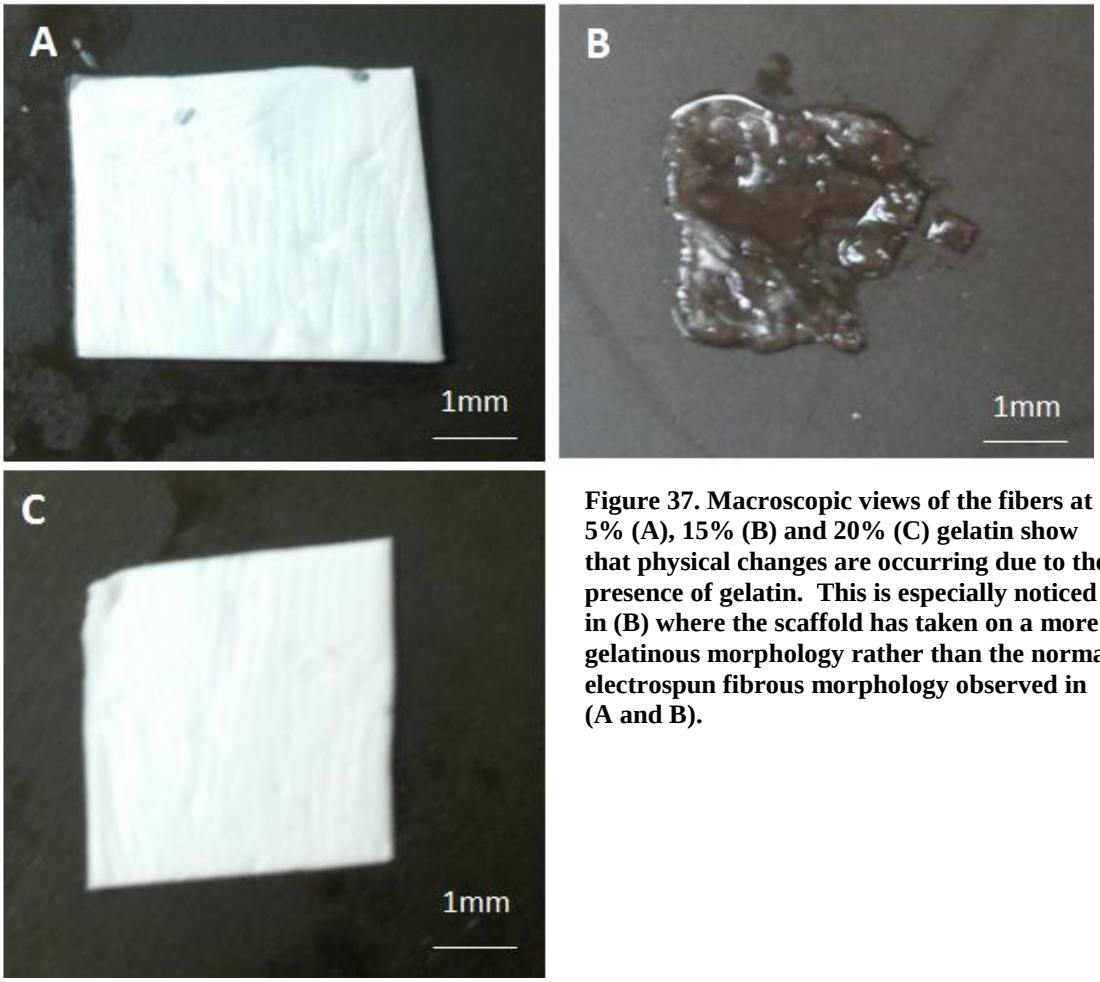

Figure 37. Macroscopic views of the fibers at 5% (A), 15% (B) and 20% (C) gelatin show that physical changes are occurring due to the presence of gelatin. This is especially noticed in (B) where the scaffold has taken on a more gelatinous morphology rather than the normal electrospun fibrous morphology observed in (A and B).

7.3 **Discussion**

A main challenge with electrospun scaffolds is the limited pore size that is generated due to the densely packing of the fibers during the electrospinning process. These scaffolds do contain interconnected pores throughout, which generate a relatively high porosity; however there is limited ability for the cells to infiltrate the scaffolds due the small size of the pores [69]. A number of methods have been employed to increase pore sizes in electrospun scaffolds. One promising technique is the incorporation of sacrificial fibers to be removed post-spinning [69-71], which enhances cell migration into the electrospun scaffolds via the creation of larger pore sizes *in vitro*. This can be used as a

potential conduit into the idea that this will also enhance tissue formation into bone scaffolds *in vivo*.

As a proof-of-concept model to this end, we aimed at synthesizing porous PLGA nanofibrous scaffolds by using gelatin as a sacrificial material with the possible end goal of applying this to chitosan scaffolds. Since chitosan is a more difficult material to work with, we first optimized the scaffold fabrication conditions using a simpler, more reproducible material, such as PLGA. By developing an electrospinning set up allowing for two materials to be collected on one rotating collector (Figure 32), we were able to obtain scaffolds containing varying w/w ratios of PLGA to gelatin to theoretically vary the pore size. We left the concentration of PLGA constant at 15% and varied the concentration of gelatin from 5% to 15% to 20%, obtaining theoretical "porosities" of 0%, 25%, 50% and 57%. Using these values, we were able to effectively change to carrying capacity of the theoretical scaffold by adjusting the scaffold volume relative to the inclusion of porosity developed from gelatin removal. We used this method to develop the graphs seen in Figure 34. Based on the model developed by Lemon et. al. we adjusted the theoretical growth of MSCs in terms of volume fraction on/in the PLGA scaffolds when the scaffolds were hydrated and morphologically changed. The data shows that we can generate predictive curves and fit the data to this model, however the values obtained did not show a good correlation to biological function. The lsqcurvefit function of MatLab takes the data obtained (cell growth via AB assay) and fits it to the equation generated by Lemon et. al. (Figure 36). The values should follow a similar trend, however, as seen in Table 4, this does not occur. The mathematics used to fit the data was substantially noisy and not a good model of what was occurring on the

scaffolds. This is also noticed by the extremely variable carrying capacity and cell volume fraction, which indicates that this was not a good representation of the biological function of these scaffolds.

To correct for this, we decided to fit the data to a logistics growth model, which is a good representation of modeling cell behavior in 2D, or in our case, growing on the surface of the scaffold rather than penetrating in. When we fit the data to these curves, which were generated using the cftool function in MatLab (a simpler curve fitting tool), we see a much better fit between data and model for both cell growth rate and the effective carrying capacity of the scaffolds (Figure 36) and conclude that the cells were remaining on the surface of the scaffold and not penetrating into the scaffold interior.

This would then lead us to our final conclusion, that the gelatin was not being removed and porosity was not being generated, as originally hypothesized. To validate this assumption, we observed the fibers under SEM and found that the water-soluble gelatin was indeed not being removed from the PLGA scaffolds by immersion into water, as predicted.. PLGA nanofibers can be seen to be surrounded by varying sizes of gelatin fibers in the scaffolds (Figure 37). At 5%, beads of gelatin were entangled by PLGA fibers, whereas at 15% and 20%, the gelatin and PLGA fibers can be seen to be intermingling with each other. However, (Table 3), there is a significant change in the stiffness of these scaffolds with gelatin incorporation after hydration. This would indicate that the physical properties of the scaffolds are different based on gelatin content making them tunable and versatile scaffolds applicable for many different tissue types.

Chapter 8. Future Work and Considerations

8.1 Modified CTS-HA-GP Scaffold Conditions for Enhanced Cell/Tissue Infiltration

As mentioned in chapter 7, PLGA/gelatin was used as a proof of concept model test the usefulness of using sacrificial fibers for enhanced porosity in electrospun scaffolds. Though the results were unexpected, we did observe mechanical and physical changes to the scaffold when gelatin was incorporated. Building on this data and idea, it would be feasible to attempt using a similar method to enhance the porosity of chitosan scaffolds. However, using the data obtained from the PLGA studies, appropriate changes can be made to improve the scaffold properties. Rather than using gelatin, a synthetic material that is water soluble, such as PEO, may prove easier to remove. Also, as important as mechanical properties are, the cellular integrative properties of the scaffold are of much more importance, such as having a scaffold that is capable of producing the right cues to induce host tissue osteoprogenitor cells to migrate into the tissue. Once we have shown that cells can migrate into the scaffolds, these cells can use the scaffold as a template to begin depositing their own mineralized matrix, which will develop into new functional bone.

Tissue infiltration was observed on the CTS-HA-GP scaffolds by histological analysis of *in vivo* experiments (Figure 30). Further enhancing the porosity might further enhance tissue infiltration and host cell migration into the scaffold. This could prove to be very useful in terms of biocompatibility and speeding up the development of bone tissue *in vivo*. Improved osteoinduction of CTS-HA-GP scaffolds

In this study we used ALP activity as an early marker of osteogenic differentiation. In order to complete this picture of osteogenesis, it would be important to further characterize this process using gene expression and protein synthesis of specific bone markers. For the scope of this project, where we wanted to show that these scaffolds were capable of inducing MSCs differentiation towards an osteogenic lineage, using an ALP assay to observe the onset of osteogenesis sufficed. However, osteogenic gene profiling could lead to mechanistic studies trying to understand how these scaffolds can induce osteogenic differentiation.

Cell attachment and integrin expression can carefully regulate genetic expression and cellular function, whether it be proliferation, migration or differentiation. To our knowledge, no studies have demonstrated the attachment mechanisms for chitosan nanofibers. Studying what cell-matrix adhesion proteins are upregulated upon seeding could give insight into how osteogenesis progresses on these scaffolds. Specific integrin binding is upregulated as the main ECM component of bone, collagen I, is deposited. By studying the upregulation of these integrins, we can determine the rate at which ECM production correlates to the time at which differentiation begins Lemon et. al. determined that ECM production is delayed as proliferation occurs [142], which may give an indication as to the effects that ECM production plays on differentiation vs. the effects the actual fibrous scaffold has on it.

Another cell-ECM molecule involved in osteogenic differentiation is syndecan-4, an intramembranous proteoglycan complex. Chitosan is a polysaccharide with a very similar structure to the natural GAGs found in native bone tissue. If syndecan-4 shows upregulation, it may be inferred that the molecular configuration of chitosan can mimic

these GAGs and lead to differentiation via the proteoglycan pathway rather than an integrin pathway. It may even be observed that these pathways act synergistically and both pathways are upregulated, speeding up osteogenesis.

To monitor osteogenic differentiation, it would be important to also formulate a complete profile of gene expression and protein synthesis over a time period of 3-5 weeks. Most experiments were carried out over three weeks, the normal amount of time allotted for differentiation, however these cells, as results from Figure 30 indicate, may be undergoing endochondral ossification. If this is, in fact, occurring, it would be important to extend the time of experimentation and observe for both chondrogenic and osteogenic markers of MSC differentiation. Chondrogenic markers such as transcription factor Runx1, aggrecan, collagen type II and Sox9 could be studied to see if MSCs are initially entering a chondrogenic phase. Then, specific genetic markers, such as transcriptions factors Runx2 and Osterix indicate the initiation of osteogenesis. Further, observing intracellular protein synthesis of osteopontin, osteonectin and osteocalcin all indicate osteogenesis is approaching the stage of mature osteoblasts. Finally, observing the production of bone specific ECM proteins, such as collagen type I and vitronectin as well as looking for mineralization would prove that mature osteoblasts are beginning to synthesize the important matrix required for mature bone tissue and regeneration.

Osteogenesis in our scaffolds was enhanced both by high seeding density and the used of an osteogenic growth medium. Although HA did significantly increase the osteogenic potential of the scaffolds, the use of OGM further increased ALP activity, indicating an additive effect between chemical and physical cues. By incorporating

specific factors, such as BMPs into the scaffold, a significant increase in osteogenesis may be observed.

8.2 Improved Methodology for In Vivo Analysis

One problem observed when the samples were harvested for the *in vivo* analysis was that some of the scaffolds had moved off of the wound site and were located elsewhere on the skull. We concluded that this was probably due to the mice grooming themselves or clawing at the irritated areas. This could be overcome by using a good, biological adhesive to hold the scaffold in place. Although vetbond was used to try and secure the scaffolds in spot, a very minimal amount was used in order to ensure that it was not causing any reaction between the scaffold/tissue junctions. Using a more biological fibrin glue may be a good alternative to this.

It would also be valuable to look deeper into the scaffold/tissue interactions by studying the specific immune responses (if any) that are being generated by the scaffold. This could be done by immunostaining for specific lymphocytes or other immune cells to be present or absent around the defect area.

Finally, mineralization on the scaffold would indicate that osteoprogenitor cells have migrated into the host tissue and began depositing the mineralized matrix required for bone regeneration. Using an alizarin red stain, it would be possible to observe and quantify this mineralization.

References

[1] Wegst UGK, Schecter M, Donius AE, Hunger PM. Biomaterials by freeze casting. Philos T R Soc A. 2010;368:2099-121.

[2] Rios CN, Skoracki RJ, Miller MJ, Satterfield WC, Mathur AB. In vivo bone formation in silk fibroin and chitosan blend scaffolds via ectopically grafted periosteum as a cell source: a pilot study. Tissue Eng Part A. 2009;15:2717-25.

[3] Zhou Y, Chen F, Ho ST, Woodruff MA, Lim TM, Hutmacher DW. Combined marrow stromal cell-sheet techniques and high-strength biodegradable composite scaffolds for engineered functional bone grafts. Biomaterials. 2007;28:814-24.

[4] Tsuji K, Bandyopadhyay A, Harfe BD, Cox K, Kakar S, Gerstenfeld L, et al. BMP2 activity, although dispensable for bone formation, is required for the initiation of fracture healing. Nature genetics. 2006;38:1424-9.

[5] Kumar MNVR. A Review of Chitin and Chitosan Applications. Reactive and Functional Polymers. 2000;46:1-27.

[6] Senagore AJ. The Gale encyclopedia of surgery : a guide for patients and caregivers. Detroit: Gale; 2004.

[7] (NIH) TNIoH. Cancer Statistics. In: (SEER) SEaER, editor.2009. p. Statistical figures on cancers affecting the oral cavity and pharynx, bone and joint, brain and other nervous tissue.

[8] Cooper GM, Mooney MP, Gosain AK, Campbell PG, Losee JE, Huard J. Testing the critical size in calvarial bone defects: revisiting the concept of a critical-size defect. Plast Reconstr Surg. 2010;125:1685-92.

[9] Laurie SW, Kaban LB, Mulliken JB, Murray JE. Donor-site morbidity after harvesting rib and iliac bone. Plast Reconstr Surg. 1984;73:933-8.

[10] Kurz LT, Garfin SR, Booth RE, Jr. Harvesting autogenous iliac bone grafts. A review of complications and techniques. Spine (Phila Pa 1976). 1989;14:1324-31.

[11] Smucker JD, Akhavan S, Furey C. Understanding bony safety zones in the posterior iliac crest: an anatomic study from the Hamann-Todd collection. Spine (Phila Pa 1976). 2010;35:725-9.

[12] Turner JA, Ersek M, Herron L, Haselkorn J, Kent D, Ciol MA, et al. Patient outcomes after lumbar spinal fusions. JAMA. 1992;268:907-11.

[13] Cooper LF. Biologic determinants of bone formation for osseointegration: clues for future clinical improvements. J Prosthet Dent. 1998;80:439-49.

[14] Ripamonti U. The induction of bone in osteogenic composites of bone matrix and porous hydroxyapatite replicas: an experimental study on the baboon (Papio ursinus). J Oral Maxillofac Surg. 1991;49:817-30.

[15] Lykins CL, Friedman CD, Costantino PD, Horioglu R. Hydroxyapatite cement in craniofacial skeletal reconstruction and its effects on the developing craniofacial skeleton. Arch Otolaryngol Head Neck Surg. 1998;124:153-9.

[16] Lee DW, Kim JY, Lew DH. Use of rapidly hardening hydroxyapatite cement for facial contouring surgery. J Craniofac Surg. 2010;21:1084-8.

[17] Kumaran ST, Arun KV, Sudarsan S, Talwar A, Srinivasan N. Osteoblast response to commercially available demineralized bone matrices--an in-vitro study. Indian J Dent Res. 2010;21:3-9.

[18] Steele DG, Bramblett CA. The anatomy and biology of the human skeleton. 1st ed. College Station: Texas A&M University Press; 1988.

[19] Clarke B. Normal Bone Anatomy and Physiology. Clin J Am Soc Nephro. 2008;3:S131-S9.

[20] Clark RK. Anatomy and physiology : understanding the human body. Sudbury, Mass.: Jones and Bartlett Publishers; 2005.

[21] Hutmacher DW, Sittinger M. Periosteal cells in bone tissue engineering. Tissue Eng. 2003;9 Suppl 1:S45-64.

[22] O'Driscoll SW, Fitzsimmons JS, Commisso CN. Role of oxygen tension during cartilage formation by periosteum. J Orthopaed Res. 1997;15:682-7.

[23] Zhang X, Awad HA, O'Keefe RJ, Guldberg RE, Schwarz EM. A perspective: engineering periosteum for structural bone graft healing. Clin Orthop Relat Res. 2008;466:1777-87.

[24] Bronner F, Farach-Carson MC, Roach HI. Bone and development. London: Springer-Verlag; 2010.

[25] Hall BK. Bones and cartilage : developmental and evolutionary skeletal biology. Australia ; San Diego, Calif.: Elsevier Academic Press; 2005.

[26] Allen MR, Hock JM, Burr DB. Periosteum: biology, regulation, and response to osteoporosis therapies. Bone. 2004;35:1003-12.

[27] Tiyapatanaputi P, Rubery PT, Carmouche J, Schwarz EM, O'Keefe R J, Zhang X. A novel murine segmental femoral graft model. J Orthop Res. 2004;22:1254-60.

[28] Zhang X, Xie C, Lin AS, Ito H, Awad H, Lieberman JR, et al. Periosteal progenitor cell fate in segmental cortical bone graft transplantations: implications for functional tissue engineering. J Bone Miner Res. 2005;20:2124-37.

[29] Bostrom MP, Lane JM, Berberian WS, Missri AA, Tomin E, Weiland A, et al. Immunolocalization and expression of bone morphogenetic proteins 2 and 4 in fracture healing. J Orthop Res. 1995;13:357-67.

[30] Kandziora F, Pflugmacher R, Scholz M, Knispel C, Hiller T, Schollmeier G, et al. Comparison of BMP-2 and combined IGF-I/TGF-ss1 application in a sheep cervical spine fusion model. European spine journal : official publication of the European Spine Society, the European Spinal Deformity Society, and the European Section of the Cervical Spine Research Society. 2002;11:482-93.

[31] Xie C, Reynolds D, Awad H, Rubery PT, Pelled G, Gazit D, et al. Structural bone allograft combined with genetically engineered mesenchymal stem cells as a novel platform for bone tissue engineering. Tissue Eng. 2007;13:435-45.

[32] Ouyang HW, Cao T, Zou XH, Heng BC, Wang LL, Song XH, et al. Mesenchymal stem cell sheets revitalize nonviable dense grafts: implications for repair of large-bone and tendon defects. Transplantation. 2006;82:170-4.

[33] Knothe Tate ML, Ritzman TF, Schneider E, Knothe UR. Testing of a new one-stage bone-transport surgical procedure exploiting the periosteum for the repair of long-bone defects. The Journal of bone and joint surgery American volume. 2007;89:307-16.

[34] Peng H, Wright V, Usas A, Gearhart B, Shen HC, Cummins J, et al. Synergistic enhancement of bone formation and healing by stem cell-expressed VEGF and bone morphogenetic protein-4. The Journal of clinical investigation. 2002;110:751-9.

[35] Rutherford RB, Moalli M, Franceschi RT, Wang D, Gu K, Krebsbach PH. Bone morphogenetic protein-transduced human fibroblasts convert to osteoblasts and form bone in vivo. Tissue Eng. 2002;8:441-52.

[36] Hee CK, Jonikas MA, Nicoll SB. Influence of three-dimensional scaffold on the expression of osteogenic differentiation markers by human dermal fibroblasts. Biomaterials. 2006;27:875-84.

[37] Kakar S, Einhorn TA, Vora S, Miara LJ, Hon G, Wigner NA, et al. Enhanced chondrogenesis and Wnt signaling in PTH-treated fractures. J Bone Miner Res. 2007;22:1903-12.

[38] Wei X, Zhang C, Gu Q. [Properties, products, and applications of chitosan]. Zhongguo xiu fu chong jian wai ke za zhi = Zhongguo xiufu chongjian waike zazhi = Chinese journal of reparative and reconstructive surgery. 2010;24:1265-70.

[39] Jayakumar R, Prabaharan M, Sudheesh Kumar PT, Nair SV, Tamura H. Biomaterials based on chitin and chitosan in wound dressing applications. Biotechnol Adv. 2011;29:322-37.

[40] Linden JC, Stoner RJ, Knutson KW, Gardner-Hughes CA. Organic disease control elicitors. Agro Food Ind Hi Tec. 2000;11:32-4.

[41] Shahidi F, Synowiecki J. Isolation and Characterization of Nutrients and Value-Added Products from Snow Crab (Chinoecetes-Opilio) and Shrimp (Pandalus-Borealis) Processing Discards. J Agr Food Chem. 1991;39:1527-32.

[42] Ghosh B, Urban MW. Self-Repairing Oxetane-Substituted Chitosan Polyurethane Networks. Science. 2009;323:1458-60.

[43] Austero MS, Donius AE, Wegst UG, Schauer CL. New crosslinkers for electrospun chitosan fibre mats. I. Chemical analysis. Journal of the Royal Society, Interface / the Royal Society. 2012.

[44] Norowski PA, Mishra S, Adatrow PC, Haggard WO, Bumgardner JD. Suture pullout strength and in vitro fibroblast and RAW 264.7 monocyte biocompatibility of genipin crosslinked nanofibrous chitosan mats for guided tissue regeneration. J Biomed Mater Res A. 2012.

[45] Suresh S, Gupta M, Kumar GA, Rao VK, Kumar O, Ghosal P. Synergic effect of multi-walled carbon nanotubes and gold nanoparticles towards immunosensing of ricin with carbon nanotube-gold nanoparticles-chitosan modified screen printed electrode. The Analyst. 2012;137:4086-92.

[46] Yan S, Rao S, Zhu J, Wang Z, Zhang Y, Duan Y, et al. Nanoporous multilayer poly(L-glutamic acid)/chitosan microcapsules for drug delivery. Int J Pharm. 2012;427:443-51.

[47] Rao RR, Jiao A, Kohn DH, Stegemann JP. Exogenous mineralization of cell-seeded and unseeded collagen-chitosan hydrogels using modified culture medium. Acta Biomater. 2012;8:1560-5.

[48] Lih E, Lee JS, Park KM, Park KD. Rapidly curable chitosan-PEG hydrogels as tissue adhesives for hemostasis and wound healing. Acta Biomater. 2012;8:3261-9.

[49] Pawar H, Douroumis D, Boateng JS. Preparation and optimization of PMAA-chitosan-PEG nanoparticles for oral drug delivery. Colloids Surf B Biointerfaces. 2012;90:102-8.

[50] Frohbergh ME, Katsman A, Botta GP, Lazarovici P, Schauer CL, Wegst UG, et al. Electrospun hydroxyapatite-containing chitosan nanofibers crosslinked with genipin for bone tissue engineering. Biomaterials. 2012.

[51] Tharanathan RN, Kittur FS. Chitin--the undisputed biomolecule of great potential. Critical reviews in food science and nutrition. 2003;43:61-87.

[52] Zhang Y, Xue C, Xue Y, Gao R, Zhang X. Determination of the degree of deacetylation of chitin and chitosan by X-ray powder diffraction. Carbohydrate research. 2005;340:1914-7.

[53] Huiskes R, Weinans H, Vanrietbergen B. The Relationship between Stress Shielding and Bone-Resorption around Total Hip Stems and the Effects of Flexible Materials. Clin Orthop Relat R. 1992:124-34.

[54] Zhang Y, Venugopal JR, El-Turki A, Ramakrishna S, Su B, Lim CT. Electrospun biomimetic nanocomposite nanofibers of hydroxyapatite/chitosan for bone tissue engineering. Biomaterials. 2008;29:4314-22.

[55] Pramanik N, Mishra D, Banerjee I, Maiti TK, Bhargava P, Pramanik P. Chemical synthesis, characterization, and biocompatibility study of hydroxyapatite/chitosan phosphate nanocomposite for bone tissue engineering applications. Int J Biomater. 2009;2009:512417.

[56] Li M, Mondrinos MJ, Gandhi MR, Ko FK, Weiss AS, Lelkes PI. Electrospun protein fibers as matrices for tissue engineering. Biomaterials. 2005;26:5999-6008.

[57] Wu L, Li H, Li S, Li X, Yuan X, Zhang Y. Composite fibrous membranes of PLGA and chitosan prepared by coelectrospinning and coaxial electrospinning. J Biomed Mater Res A. 2010;92:563-74.

[58] Zhang K, Qian Y, Wang H, Fan L, Huang C, Mo X. Electrospun Silk Fibroin-Hydroxybutyl Chitosan Nanofibrous Scaffolds to Biomimic Extracellular Matrix. J Biomater Sci Polym Ed. 2010.

[59] Thomas V, Dean DR, Jose MV, Mathew B, Chowdhury S, Vohra YK. Nanostructured biocomposite scaffolds based on collagen coelectrospun with nanohydroxyapatite. Biomacromolecules. 2007;8:631-7.

[60] Zhang Y, Reddy VJ, Wong SY, Li X, Su B, Ramakrishna S, et al. Enhanced biomineralization in osteoblasts on a novel electrospun biocomposite nanofibrous substrate of hydroxyapatite/collagen/chitosan. Tissue Eng Part A. 2010;16:1949-60.

[61] Venugopal J, Low S, Choon AT, Sampath Kumar TS, Ramakrishna S. Mineralization of osteoblasts with electrospun collagen/hydroxyapatite nanofibers. J Mater Sci Mater Med. 2008;19:2039-46.

[62] Teng SH, Lee EJ, Park CS, Choi WY, Shin DS, Kim HE. Bioactive nanocomposite coatings of collagen/hydroxyapatite on titanium substrates. J Mater Sci Mater Med. 2008;19:2453-61.

[63] FEPPD. Biomechanics in Dentisry. In: Technicians FoEaID, editor.

[64] Popowics TE, Zhu Z, Herring SW. Mechanical properties of the periosteum in the pig, Sus scrofa. Arch Oral Biol. 2002;47:733-41.

[65] Bat E, Kothman BH, Higuera GA, van Blitterswijk CA, Feijen J, Grijpma DW. Ultraviolet light crosslinking of poly(trimethylene carbonate) for elastomeric tissue engineering scaffolds. Biomaterials. 2010;31:8696-705.

[66] Chen RN, Ho HO, Sheu MT. Characterization of collagen matrices crosslinked using microbial transglutaminase. Biomaterials. 2005;26:4229-35.

[67] Fathima NN, Dhathathreyan A, Ramasami T, Kragel J, Miller R. Degree of crosslinking of collagen at interfaces: adhesion and shear rheological indicators. Int J Biol Macromol. 2011;48:67-73.

[68] Zhang K, Qian Y, Wang H, Fan L, Huang C, Yin A, et al. Genipin-crosslinked silk fibroin/hydroxybutyl chitosan nanofibrous scaffolds for tissue-engineering application. J Biomed Mater Res A. 2010;95:870-81.

[69] Phipps MC, Clem WC, Grunda JM, Clines GA, Bellis SL. Increasing the pore sizes of bone-mimetic electrospun scaffolds comprised of polycaprolactone, collagen I and hydroxyapatite to enhance cell infiltration. Biomaterials. 2012;33:524-34.

[70] Baker BM, Gee AO, Metter RB, Nathan AS, Marklein RA, Burdick JA, et al. The potential to improve cell infiltration in composite fiber-aligned electrospun scaffolds by the selective removal of sacrificial fibers. Biomaterials. 2008;29:2348-58.

[71] Skotak M, Ragusa J, Gonzalez D, Subramanian A. Improved cellular infiltration into nanofibrous electrospun cross-linked gelatin scaffolds templated with micrometer-sized polyethylene glycol fibers. Biomed Mater. 2011;6:055012.

[72] Bispo VM, Mansur AA, Barbosa-Stancioli EF, Mansur HS. Biocompatibility of nanostructured chitosan/ poly(vinyl alcohol) blends chemically crosslinked with genipin for biomedical applications. J Biomed Nanotechnol. 2010;6:166-75.

[73] Barbir A, Michalek AJ, Abbott RD, Iatridis JC. Effects of enzymatic digestion on compressive properties of rat intervertebral discs. J Biomech. 2010;43:1067-73.

[74] Solorio L, Zwolinski C, Lund AW, Farrell MJ, Stegemann JP. Gelatin microspheres crosslinked with genipin for local delivery of growth factors. J Tissue Eng Regen Med. 2010;4:514-23.

[75] Bhattarai N, Edmondson D, Veiseh O, Matsen FA, Zhang M. Electrospun chitosan-based nanofibers and their cellular compatibility. Biomaterials. 2005;26:6176-84.

[76] Li WJ, Laurencin CT, Caterson EJ, Tuan RS, Ko FK. Electrospun nanofibrous structure: a novel scaffold for tissue engineering. J Biomed Mater Res. 2002;60:613-21.

[77] Hsieh HJ, Hsieh CY, Tsai SP, Ho MH, Wang DM, Liu CE, et al. Analysis of freeze-gelation and cross-linking processes for preparing porous chitosan scaffolds. Carbohyd Polym. 2007;67:124-32.

[78] Lelkes PI, Samet MM, Christensen CW, Amrani DL. Factitious Angiogenesis: Endothelialization of Artificial Cardiovascular Prostheses. In: Maragoudakis ME, Gullino PM, Lelkes PI, editors. Angiogenesis in Health and Disease. New York: Plenum Press; 1992. p. 339-51.

[79] Raub CB, Suresh V, Krasieva T, Lyubovitsky J, Mih JD, Putnam AJ, et al. Noninvasive assessment of collagen gel microstructure and mechanics using multiphoton microscopy. Biophys J. 2007;92:2212-22.

[80] O'Brien J, Wilson I, Orton T, Pognan F. Investigation of the Alamar Blue (resazurin) fluorescent dye for the assessment of mammalian cell cytotoxicity. Eur J Biochem. 2000;267:5421-6.

[81] Hunt M. Real Time PCR. In: Medicine UoSCSo, editor. Microbiology and Immunology Online. Columbia: Board of Trustees of the University of South Carolina; 2010. p. Procedure for calculating mRNA expression and normalizing logarithmically to GAPDH and Tissue Culture Plastic Controls.

[82] Desai NP, Hubbell JA. Surface Physical Interpenetrating Networks of Poly(Ethylene-Terephthalate) and Poly(Ethylene Oxide) with Biomedical Applications. Macromolecules. 1992;25:226-32.

[83] Li M, Guo Y, Wei Y, MacDiarmid AG, Lelkes PI. Electrospinning polyaniline-contained gelatin nanofibers for tissue engineering applications. Biomaterials. 2006;27:2705-15.

[84] Han J, Lazarovici P, Pomerantz C, Chen X, Wei Y, Lelkes PI. Co-Electrospun Blends of PLGA, Gelatin, and Elastin as Potential Nonthrombogenic Scaffolds for Vascular Tissue Engineering. Biomacromolecules. 2010.

[85] Li M, Mondrinos MJ, Chen X, Lelkes PI. Electrospun blends of natural and synthetic polymers as scaffolds for tissue engineering. Conf Proc IEEE Eng Med Biol Soc. 2005;6:5858-61.

[86] Kumirska J, Czerwicka M, Kaczynski Z, Bychowska A, Brzozowski K, Thoming J, et al. Application of spectroscopic methods for structural analysis of chitin and chitosan. Mar Drugs. 2010;8:1567-636.

[87] Saad FA, Hofstaetter JG. Proteomic analysis of mineralising osteoblasts identifies novel genes related to bone matrix mineralisation. Int Orthop. 2011;35:447-51.

[88] Burchardt H. The biology of bone graft repair. Clin Orthop Relat Res. 1983:28-42.

[89] Catledge SA, Clem WC, Shrikishen N, Chowdhury S, Stanishevsky AV, Koopman M, et al. An electrospun triphasic nanofibrous scaffold for bone tissue engineering. Biomed Mater. 2007;2:142-50.

[90] Schiffman JD, Schauer CL. Cross-linking chitosan nanofibers. Biomacromolecules. 2007;8:594-601.

[91] Zhang YZ, Su B, Ramakrishna S, Lim CT. Chitosan nanofibers from an easily electrospinnable UHMWPEO-doped chitosan solution system. Biomacromolecules. 2008;9:136-41.

[92] Lin L, Perets A, Har-El YE, Varma D, Li M, Lazarovici P, et al. Alimentary 'green' proteins as electrospun scaffolds for skin regenerative engineering. J Tissue Eng Regen Med. 2012.

[93] Chen ZG, Wang PW, Wei B, Mo XM, Cui FZ. Electrospun collagen-chitosan nanofiber: a biomimetic extracellular matrix for endothelial cell and smooth muscle cell. Acta Biomater. 2010;6:372-82.

[94] Geng X, Kwon OH, Jang J. Electrospinning of chitosan dissolved in concentrated acetic acid solution. Biomaterials. 2005;26:5427-32.

[95] Cai ZX, Mo XM, Zhang KH, Fan LP, Yin AL, He CL, et al. Fabrication of Chitosan/Silk Fibroin Composite Nanofibers for Wound-dressing Applications. Int J Mol Sci. 2010;11:3529-39.

[96] Xie D, Huang H, Blackwood K, MacNeil S. A novel route for the production of chitosan/poly(lactide-co-glycolide) graft copolymers for electrospinning. Biomed Mater. 2010;5:065016.

[97] Heinemann C, Heinemann S, Bernhardt A, Worch H, Hanke T. Novel textile chitosan scaffolds promote spreading, proliferation, and differentiation of osteoblasts. Biomacromolecules. 2008;9:2913-20.

[98] Danilchenko SN, Kalinkevich OV, Pogorelov MV, Kalinkevich AN, Sklyar AM, Kalinichenko TG, et al. Characterization and in vivo evaluation of chitosan-hydroxyapatite bone scaffolds made by one step coprecipitation method. J Biomed Mater Res A. 2011;96:639-47.

[99] Moore KA, Lemischka IR. Stem cells and their niches. Science. 2006;311:1880-5.

[100] Mandal BB, Kundu SC. Cell proliferation and migration in silk fibroin 3D scaffolds. Biomaterials. 2009;30:2956-65.

[101] Venugopal JR, Giri Dev VR, Senthilram T, Sathiskumar D, Gupta D, Ramakrishna S. Osteoblast mineralization with composite nanofibrous substrate for bone tissue regeneration. Cell biology international. 2011;35:73-80.

[102] Sasmazel HT. Novel hybrid scaffolds for the cultivation of osteoblast cells. Int J Biol Macromol. 2011;49:838-46.

[103] Mostafa NZ, Uludag H, Varkey M, Dederich DN, Doschak MR, El-Bialy TH. In vitro osteogenic induction of human gingival fibroblasts for bone regeneration. The open dentistry journal. 2011;5:139-45.

[104] Martins A, Pinho ED, Correlo VM, Faria S, Marques AP, Reis RL, et al. Biodegradable nanofibers-reinforced microfibrous composite scaffolds for bone tissue engineering. Tissue Eng Part A. 2010;16:3599-609.

[105] Lahiji A, Sohrabi A, Hungerford DS, Frondoza CG. Chitosan supports the expression of extracellular matrix proteins in human osteoblasts and chondrocytes. J Biomed Mater Res. 2000;51:586-95.

[106] Yang X, Chen X, Wang H. Acceleration of osteogenic differentiation of preosteoblastic cells by chitosan containing nanofibrous scaffolds. Biomacromolecules. 2009;10:2772-8.

[107] Mohammadi Y, Soleimani M, Fallahi-Sichani M, Gazme A, Haddadi-Asl V, Arefian E, et al. Nanofibrous poly(epsilon-caprolactone)/poly(vinyl alcohol)/chitosan hybrid scaffolds for bone tissue engineering using mesenchymal stem cells. The International journal of artificial organs. 2007;30:204-11.

[108] Delorme B, Charbord P. Culture and characterization of human bone marrow mesenchymal stem cells. Methods Mol Med. 2007;140:67-81.

[109] Ngiam M, Nguyen LT, Liao S, Chan CK, Ramakrishna S. Biomimetic nanostructured materials - potential regulators for osteogenesis? Ann Acad Med Singapore. 2011;40:213-10.

[110] Ode A, Duda GN, Glaeser JD, Matziolis G, Frauenschuh S, Perka C, et al. Toward biomimetic materials in bone regeneration: functional behavior of mesenchymal stem cells on a broad spectrum of extracellular matrix components. J Biomed Mater Res A. 2010;95:1114-24.

[111] Jaiswal RK, Jaiswal N, Bruder SP, Mbalaviele G, Marshak DR, Pittenger MF. Adult human mesenchymal stem cell differentiation to the osteogenic or adipogenic lineage is regulated by mitogen-activated protein kinase. Journal of Biological Chemistry. 2000;275:9645-52.

[112] Seong JM, Kim BC, Park JH, Kwon IK, Mantalaris A, Hwang YS. Stem cells in bone tissue engineering. Biomed Mater. 2010;5:062001.

[113] Giordano A, Galderisi U, Marino IR. From the laboratory bench to the patient's bedside: an update on clinical trials with mesenchymal stem cells. J Cell Physiol. 2007;211:27-35.

[114] Acharya C, Adesida A, Zajac P, Mumme M, Riesle J, Martin I, et al. Enhanced chondrocyte proliferation and mesenchymal stromal cells chondrogenesis in coculture pellets mediate improved cartilage formation. J Cell Physiol. 2012;227:88-97.

[115] Erickson IE, Kestle SR, Zellars KH, Farrell MJ, Kim M, Burdick JA, et al. High mesenchymal stem cell seeding densities in hyaluronic acid hydrogels produce engineered cartilage with native tissue properties. Acta Biomater. 2012;8:3027-34.

[116] Lee JB, Jeong SI, Bae MS, Yang DH, Heo DN, Kim CH, et al. Highly porous electrospun nanofibers enhanced by ultrasonication for improved cellular infiltration. Tissue Eng Part A. 2011;17:2695-702.

[117] Rene Oliveres-Navarrete JJO, Claudia Ramirez and Sandra Elizabeth Rodil. Biocompatibility of Niobium Coatings. Coatings. September 15, 2011;1:72-87.

[118] Tchemtchoua VT, Atanasova G, Aqil A, Filee P, Garbacki N, Vanhooteghem O, et al. Development of a chitosan nanofibrillar scaffold for skin repair and regeneration. Biomacromolecules. 2011;12:3194-204.

[119] Krinner A, Hoffmann M, Loeffler M, Drasdo D, Galle J. Individual fates of mesenchymal stem cells in vitro. BMC systems biology. 2010;4:73.

[120] Wang G, Liu X, Zreiqat H, Ding C. Enhanced effects of nano-scale topography on the bioactivity and osteoblast behaviors of micron rough ZrO2 coatings. Colloids Surf B Biointerfaces. 2011;86:267-74.

[121] Teven CM, Liu X, Hu N, Tang N, Kim SH, Huang E, et al. Epigenetic regulation of mesenchymal stem cells: a focus on osteogenic and adipogenic differentiation. Stem Cells Int. 2011;2011:201371.

[122] Marom R, Shur I, Solomon R, Benayahu D. Characterization of adhesion and differentiation markers of osteogenic marrow stromal cells. J Cell Physiol. 2005;202:41-8.

[123] Silber JS, Anderson DG, Daffner SD, Brislin BT, Leland JM, Hilibrand AS, et al. Donor site morbidity after anterior iliac crest bone harvest for single-level anterior cervical discectomy and fusion. Spine (Phila Pa 1976). 2003;28:134-9.

[124] Harkness L, Mahmood A, Ditzel N, Abdallah BM, Nygaard JV, Kassem M. Selective isolation and differentiation of a stromal population of human embryonic stem cells with osteogenic potential. Bone. 2011;48:231-41.

[125] Levi B, James AW, Nelson ER, Vistnes D, Wu B, Lee M, et al. Human adipose derived stromal cells heal critical size mouse calvarial defects. PLoS One. 2010;5:e11177.

[126] Terella A, Mariner P, Brown N, Anseth K, Streubel SO. Repair of a calvarial defect with biofactor and stem cell-embedded polyethylene glycol scaffold. Arch Facial Plast Surg. 2010;12:166-71.

[127] Haberstroh K, Ritter K, Kuschnierz J, Bormann KH, Kaps C, Carvalho C, et al. Bone repair by cell-seeded 3D-bioplotted composite scaffolds made of collagen treated tricalciumphosphate or tricalciumphosphate-chitosan-collagen hydrogel or PLGA in ovine critical-sized calvarial defects. J Biomed Mater Res B Appl Biomater. 2010;93:520-30.

[128] Schwarz F, Ferrari D, Sager M, Herten M, Hartig B, Becker J. Guided bone regeneration using rhGDF-5- and rhBMP-2-coated natural bone mineral in rat calvarial defects. Clin Oral Implants Res. 2009;20:1219-30.

[129] Ratner BD. Biomaterials science : an introduction to materials in medicine. 2nd ed. Amsterdam ; Boston: Elsevier Academic Press; 2004.

[130] Jones KS. Effects of biomaterial-induced inflammation on fibrosis and rejection. Seminars in immunology. 2008;20:130-6.

[131] Gentili C, Cancedda R. Cartilage and bone extracellular matrix. Curr Pharm Des. 2009;15:1334-48.

[132] Boskey AL, Posner AS. Bone structure, composition, and mineralization. Orthop Clin North Am. 1984;15:597-612.

[133] Yang W, Yang F, Wang Y, Both SK, Jansen JA. In vivo bone generation via the endochondral pathway on three-dimensional electrospun fibers. Acta Biomater. 2013;9:4505-12.

[134] Campos MG, Rawls HR, Innocentini-Mei LH, Satsangi N. In vitro gentamicin sustained and controlled release from chitosan cross-linked films. J Mater Sci Mater Med. 2009;20:537-42.

[135] Khor E, Lim LY. Implantable applications of chitin and chitosan. Biomaterials. 2003;24:2339-49.

[136] Zeng YJ, Sun XP, Yang J, Wu WH, Xu XH, Yan YP. Mechanical properties of nasal fascia and periosteum. Clin Biomech (Bristol, Avon). 2003;18:760-4.

[137] de Campos AM, Diebold Y, Carvalho EL, Sanchez A, Alonso MJ. Chitosan nanoparticles as new ocular drug delivery systems: in vitro stability, in vivo fate, and cellular toxicity. Pharmaceutical research. 2004;21:803-10.

[138] Di Martino A, Sittinger M, Risbud MV. Chitosan: a versatile biopolymer for orthopaedic tissue-engineering. Biomaterials. 2005;26:5983-90.

[139] Chung MJ, Park JK, Park YI. Anti-inflammatory effects of low-molecular weight chitosan oligosaccharides in IgE-antigen complex-stimulated RBL-2H3 cells and asthma model mice. Int Immunopharmacol. 2012;12:453-9.

[140] Cui X, Zhao D, Zhang B, Gao Y. Osteogenesis mechanism of chitosan-coated calcium sulfate pellets on the restoration of segmental bone defects. J Craniofac Surg. 2009;20:1445-50.

[141] Ito Y, Hasuda H, Kamitakahara M, Ohtsuki C, Tanihara M, Kang IK, et al. A composite of hydroxyapatite with electrospun biodegradable nanofibers as a tissue engineering material. J Biosci Bioeng. 2005;100:43-9.

[142] Lemon G, Waters SL, Rose FR, King JR. Mathematical modelling of human mesenchymal stem cell proliferation and differentiation inside artificial porous scaffolds. Journal of theoretical biology. 2007;249:543-53.

[143] Grayson WL, Ma T, Bunnell B. Human mesenchymal stem cells tissue development in 3D PET matrices. Biotechnology progress. 2004;20:905-12.

[144] Grayson WL, Zhao F, Izadpanah R, Bunnell B, Ma T. Effects of hypoxia on human mesenchymal stem cell expansion and plasticity in 3D constructs. J Cell Physiol. 2006;207:331-9.

[145] Kean T, Roth S, Thanou M. Trimethylated chitosans as non-viral gene delivery vectors: cytotoxicity and transfection efficiency. J Control Release. 2005;103:643-53.

[146] Ji QX, Zhong de Y, Lu R, Zhang WQ, Deng J, Chen XG. In vitro evaluation of the biomedical properties of chitosan and quaternized chitosan for dental applications. Carbohydrate research. 2009;344:1297-302.

[147] Ong SY, Wu J, Moochhala SM, Tan MH, Lu J. Development of a chitosan-based wound dressing with improved hemostatic and antimicrobial properties. Biomaterials. 2008;29:4323-32.

[148] Rao SB, Sharma CP. Use of chitosan as a biomaterial: studies on its safety and hemostatic potential. J Biomed Mater Res. 1997;34:21-8.

[149] Mir VG, Heinamaki J, Antikainen O, Revoredo OB, Colarte AI, Nieto OM, et al. Direct compression properties of chitin and chitosan. European journal of pharmaceutics and biopharmaceutics : official journal of Arbeitsgemeinschaft fur Pharmazeutische Verfahrenstechnik eV. 2008;69:964-8.

[150] Madihally SV, Matthew HW. Porous chitosan scaffolds for tissue engineering. Biomaterials. 1999;20:1133-42.

[151] Tang C, Xiang L, Su J, Wang K, Yang C, Zhang Q, et al. Largely improved tensile properties of chitosan film via unique synergistic reinforcing effect of carbon nanotube and clay. J Phys Chem B. 2008;112:3876-81.

[152] Onishi H, Machida Y. Biodegradation and distribution of water-soluble chitosan in mice. Biomaterials. 1999;20:175-82.

[153] Aiba S. Studies on chitosan: 4. Lysozymic hydrolysis of partially N-acetylated chitosans. Int J Biol Macromol. 1992;14:225-8.

[154] Lee KY, Ha WS, Park WH. Blood compatibility and biodegradability of partially N-acylated chitosan derivatives. Biomaterials. 1995;16:1211-6.

[155] Li S, Wang XT, Zhang XB, Yang RJ, Zhang HZ, Zhu LZ, et al. Studies on alginate-chitosan microcapsules and renal arterial embolization in rabbits. J Control Release. 2002;84:87-98.

[156] Kang GD, Song SC. Effect of chitosan on the release of protein from thermosensitive poly(organophosphazene) hydrogels. Int J Pharm. 2008;349:188-95.

[157] Fernandes R, Bentley WE. AI-2 biosynthesis module in a magnetic nanofactory alters bacterial response via localized synthesis and delivery. Biotechnology and bioengineering. 2009;102:390-9.

[158] Fernandes R, Tsao CY, Hashimoto Y, Wang L, Wood TK, Payne GF, et al. Magnetic nanofactories: localized synthesis and delivery of quorum-sensing signaling molecule autoinducer-2 to bacterial cell surfaces. Metabolic engineering. 2007;9:228-39.

[159] Kim CH LS, Lim JK, Son Y. Method of Producing Chitosan Scaffold Having High Tensile Strength and Chitosan Scaffold Produced Using This Method. In: USPTO, editor. USA: Cantor Calhoun LLP; 2008.

Appendix – Supplemental Material

Protocol for Making Electrospun CTS-HA-GP Working Solution

1. 0.35g of medium molecular weight CTS and 0.05g of HA are added to 5mL of TFA and stirred for 7 days to ensure proper mixing and dissolution of the solvent. The yielding solution is 7% CTS and 0.1% HA (v/v)
2. After 7 days of stirring, the solution is loaded into a 5mL glass syringe and inserted into the syringe pump. The syringe pump is set for 1.0mL/h and hooked up to a high voltage supply (positive lead to the needle and negative lead to the collecting plate) and held at a constant 15kV.
3. The collecting plate is situated 15cm from the needle tip and the pump is activated to produce nanofibrous scaffolds.
4. In order to ensure maximum fiber collection, the tip must be wiped clean every 10-15 minutes to avoid clogging.
5. Scaffolds are collected after all solution is dispersed and stored in the cabinet until ready for use.

MatLab Code for Generating the 3D and 2D Models Used to Observe Cell Behavior

Code to Plot Theoretical Curves from Literature Values

```
%syms veff vstem0 kss kes


%set constant variables
veff= 0.193      ;%proportional to porosity
vstem0= 0.18    ;%proportional to seeding density
kes= 1.98;
kss= 15.2;

a= 1/2 * kss/kes;
c1=1/2*(a^(-1))*(1-(1+4*a*(veff-vstem0))^.5);
c2=1/2*a^-1*(1+(1+4*a*(veff-vstem0))^.5);
c3=a^-1*vstem0;
```

```
f1=-(c3+c1^2)^-1*(c1-c2)^-1;
f2=(c3+c2^2)^-1*(c1-c2)^-1;
f3=-1/2*(c1+c2)*(c3+c1^2)^-1*(c3+c2^2)^-1;
f4=-(c1*c2-c3)*(c3+c1^2)^-1*(c3+c2^2)^-1*c3^(-1/2);

%syms vecm
%t=((a^2*kes)^-1)*(f1*log(c1/(c1+vecm))+f2*log(c2/(c2+vecm))...
%    +f3*log(c3/(c3+vecm^2))+f4*atan(vecm/c3^.5));
vecm=0:.001:.12;
t=((a.^2.*kes).^-1).*(f1.*log(c1./(c1+vecm))+f2.*log(c2./(c2+vecm))...
    +f3.*log(c3./(c3+vecm.^2))+f4.*atan(vecm./c3.^.5));

vstem=vstem0+a.*vecm.^2;

%ezplot(t,[0,.15]);
plot(t,vstem)
xlabel('time(d)')
ylabel('Cell Volume Fraction')
```

Code to Fit Obtained Data to the 3D Model from Lemon et. al.

```
function t = mikesfun(x,xdata)
%F = x(1)*exp(x(2)*xdata);

% x(1) => veff= 0.193;     %proportional to porosity
% x(2) => vstem0= 0.015;    %proportional to seeding density
% x(3) => kes= 1.98;
% x(4) => kss= 15.2;

%a= 1/2 * kss/kes;
 a= 1/2 * x(4)/x(3);
%c1=1/2*(a^(-1))*(1-(1+4*a*(veff-vstem0))^.5);
 c1=1/2*(a^(-1))*(1-(1+4*a*(x(1)-x(2)))^.5);
%c2=1/2*a^-1*(1+(1+4*a*(veff-vstem0))^.5);
 c2=1/2*(a^(-1))*(1+(1+4*a*(x(1)-x(2)))^.5);
%c3=a^-1*vstem0;
 c3=a^-1*x(2);
f1=-(c3+c1^2)^-1*(c1-c2)^-1;
f2=(c3+c2^2)^-1*(c1-c2)^-1;
f3=-1/2*(c1+c2)*(c3+c1^2)^-1*(c3+c2^2)^-1;
f4=-(c1*c2-c3)*(c3+c1^2)^-1*(c3+c2^2)^-1*c3^(-1/2);


vecm = sqrt((xdata-x(2))./a);

%t=((a^2*kes)^-1)*(f1*log(c1/(c1+vecm))+f2*log(c2/(c2+vecm))...
%    +f3*log(c3/(c3+vecm^2))+f4*atan(vecm/c3^.5));

t=((a.^2.*x(3)).^-1).*(f1.*log(c1./(c1+vecm))+f2.*log(c2./(c2+vecm))...
    +f3.*log(c3./(c3+vecm.^2))+f4.*atan(vecm./c3.^.5));
end
```

```
vstem0=0.001:0.001:0.150;
x = zeros(length(i),4);
resnorm = zeros(length(i),1);

for i=1:150
    [x1,resnorm1] =
lsqcurvefit(@mikesfun,[0.193,i/1000,1.98,15.2],g05,time);
    x(i,:) = real(x1); resnorm(i) = resnorm1;
end

plot(vstem0,real(resnorm))
```

Code to Fit Obtained Data to the 2D Logistic Growth Model

```
Days   = [1 2 3 4 7]';
VCFg00 = [0.077679542 0.126931779 0.146994885 0.183787247
0.196007068]';
VCFg05 = [0.052099761 0.109903986 0.150304384 0.176447921
0.177595734]';
VCFg15 = [0.072562668 0.122034461 0.154474862 0.161272691
0.188675762]';
VCFg20 = [0.074572603 0.119041787 0.149649126 0.154444453
0.193100517]';
cftool
```

Supplemental Material on the Processing and Use of Chitosan as a Biopolymer

Over 100 billion tons of chitin are produced each year from various living sources. Only 75,000 tons of shrimp shells are actually produced each year and in 1988 Japan only produced 2000 tons of chitosan but as of the year 2000, India alone had the potential to produce 60,000-80,000 tons of chitosan per year. Some major manufacturing companies include BioPrawn, Chito-Bios, Kate international and Seafresh Chitosan. [145]

The degree of deacetylation, the distribution of deacetylation and the molecular weight of chitosan are some of the most important variables that will determine the physical and chemical properties of chitosan. Chitosan is generally sold as greater than

75% deacetylated or 75-80% deacetylated because these levels can be achieved without significant chain degradation or additional processing. The molecular weight of unmodified chitin is over 1,000,000g/mol but the molecular weight of most commercial chitosan can range from 100,000 to 1,200,000 grams/mol depending on how it is processed [51].

Chitin's usefulness as a biomedical material is strongly limited by its insolubility, but the conversion of acetamido groups to primary amine groups creates a polymer with a positive charge in an acidic pH (less than 6) and this is what makes chitosan soluble and so much more useful but also more susceptible to degradation [52]. The solubility of chitosan also depends on the distribution of N-acetyl groups. When chitosan has a uniform distribution of acetyl groups, the polymer is less crystalline which results in an increase in solubility. The solubility of chitosan can also be enhanced by creating water soluble salts through spray drying at 175°C [146].

Chitosan is rich in primary amine groups, making it a polycation. These functional groups have the potential to interact favorably with negatively charged substances, including proteins, cell membranes and anionic materials such as alginate. They also give chitosan its hemostatic properties [147]. Chitosan will coagulate whole blood in a process that does not depend on the classic coagulation mechanisms but instead is believed to be caused by interactions with red blood cell membranes and positively charged chitosan [148].

Chitosan can also be used to form complexes with transition metals which can be useful for water purification and recovery of metals such as copper and mercury [38].

Nitrogen in the primary amine acts as an electron donor, which gives chitosan the ability to selectively chelate metals even though they are positively charged. It was shown that samples with greater than 55% deacetylation were most useful for this application. Chitosan's affinity for different metals can vary greatly (Supplementary Figure 1) [38].

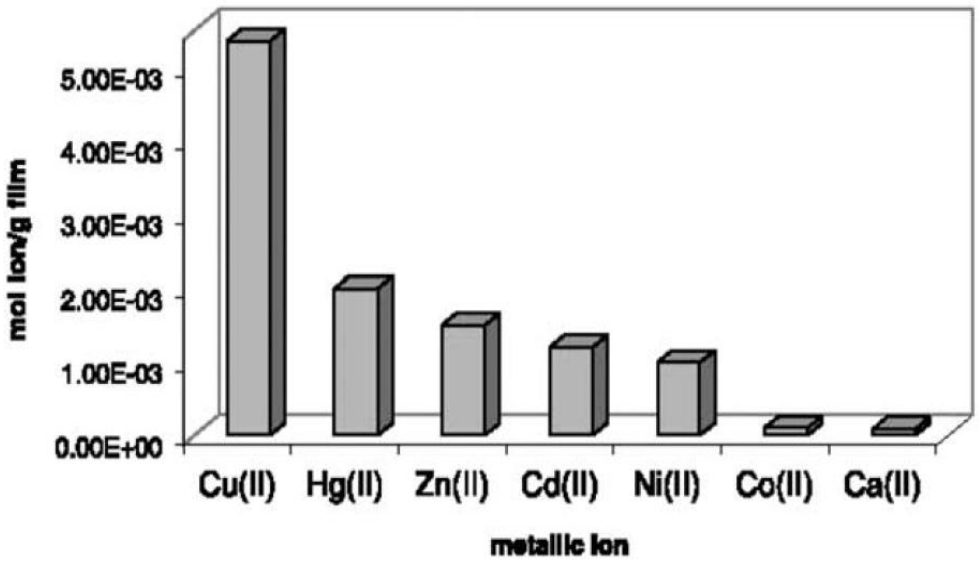

Supplementary Figure 1. The affinity of chitosan to bind different metal ions varies greatly, indicating the versatility of the material and its broad applications. ***Wei X, Zhang C, Gu Q. [Properties, products, and applications of chitosan]. 2010***

Chitosan can be used to form films, coatings, hydrogels, fibers and sponges. Each of these forms has its own unique properties, its own strengths and weaknesses and each form can also be fabricated and modified in a number of ways. However one attribute that Chitosan is generally known for is its toughness or its ability to undergo large amounts of plastic deformation [149].

Chitosan scaffolds can be made by freezing chitosan gels or solutions followed by lyophilization. This material is stiff and inelastic, but when hydrated it will quickly swell and then dissolve. This can be prevented by allowing the material to equilibrate in 0.1M

NaOH for half an hour; however the base will cause changes in the crystallinity of the material which will cause shrinkage and shape change, which is only partially reversed when the material is moved into a solution with neutral pH. Non-porous scaffolds can be strained up to 30-40% and porous scaffolds can be strained from 30-110% with more porous scaffolds being capable of undergoing more strain (Supplementary Figure 2) [150].

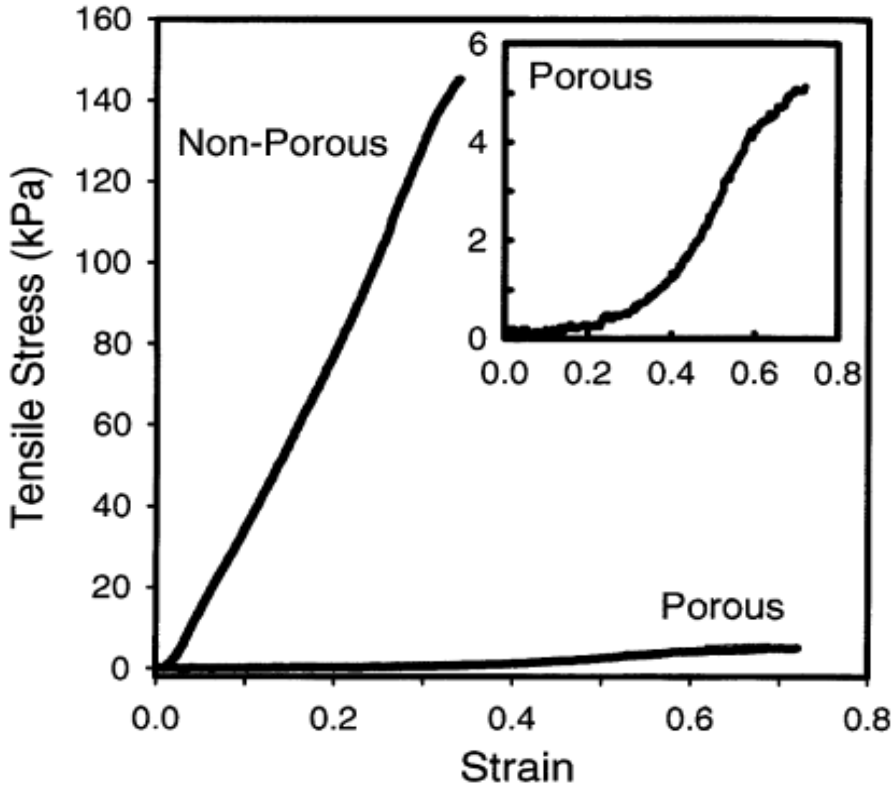

Supplementary Figure 2. The effects of increased porosity on the mechanical properties of chitosan scaffolds. As observed, enhanced porosity will greatly increase the amount of strain chitosan can undergo, which will subsequently increase the Young's modulus making a more elastic material with a decreased toughness. ***Madihally SV, Matthew HW. Porous chitosan scaffolds for tissue engineering. 2009***

While the non-porous bulk scaffold showed a young's modulus on the order of 200kPa, the mechanical properties of a chitosan thin film are significantly higher. Thin films of about 100μm were created by simply pouring a 2% Chitosan solution into a

hydrophobic glass plate and heating at 50° C. The tensile strength of these Chitosan films is on the order of 40 MPa and the young's modulus is on the order of 10 MPa (Supplementary Figure 3), almost 50 times higher than the porous scaffolds, but these thin films could only be strained 12% before failure. The use of composite materials combining chitosan, clay and carbon nanotubes also affected the mechanical properties [151]. For example the addition of 3% clay can increase the tensile strength from 40MPa to over 70MPa while reducing the strain at break from 12% to 4.5%. Similar results were also seen for the addition of 0.4% carbon nano tubes, however the addition of both clay and carbon nanotubes had a synergistic effect, increasing the tensile strength at break to over 110MPa, and increase the strain at break to close to 7% (Supplementary Figure 3) [151].

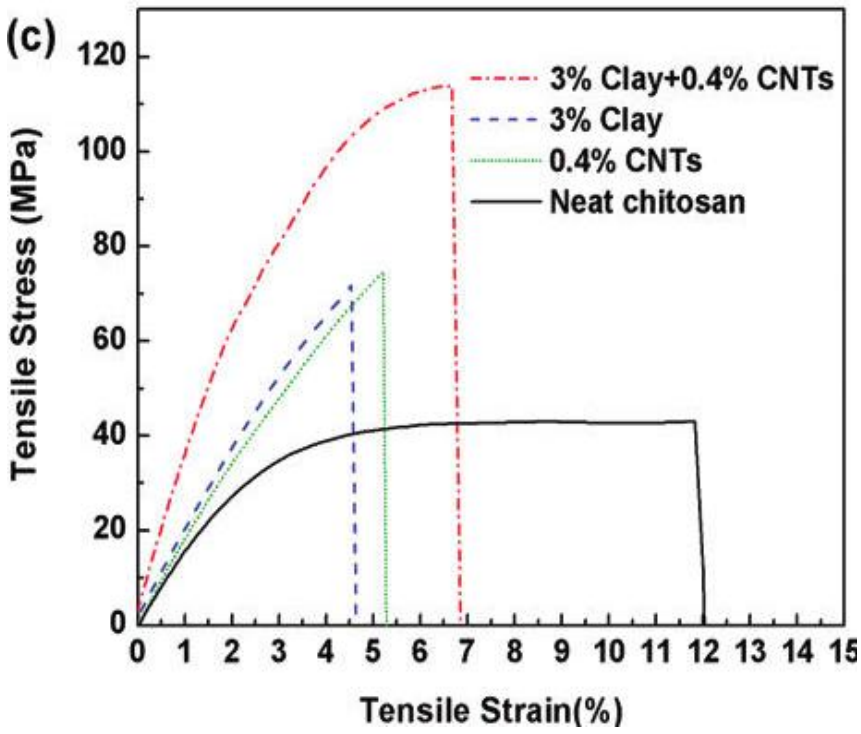

Supplementary Figure 3. The effects of blending materials to tune the mechanical properties of chitosan films were observed. This high tenability indicates again the versatility of chitosan and its wide range of applications in a number of fields. For biomedical purposes, these mechanics could be tuned to meet the different criteria of different tissues. ***Tang et. al. Largely improved tensile properties of chitosan film via unique synergistic reinforcing effect of carbon nanotube and clay. 2008***

Chitosan being a natural biopolymer, has good biodegradability and metabolism aspects, which means it is well tolerated as a biomaterial than other innately different materials like metals or ceramics [152]. Biodegradabilty is a result of chemical enzymatic attack on the biomaterial. Chitosan is primarily broken down by lysozyme in the body [153]. It has been reported that N-acylated chitosans are sparingly digestible by lysozymes as opposed to N-acetyl chitosan [154]. These results can be used to counter the problem and engineer chitosan derivatives with longer functionality periods in the body.

One of the issues is that it is difficult to achieve a burst release with chitosan delivery vehicles. Chitosan is ideal for a sustained and prolonged release, but the initial loading dose (rapid release of drug into the system), which is responsible for quick onset of action is better achieved by other delivery systems. Chitosan is being used with other competitor biomaterials, so as to devise a system which addresses advantages and disadvantages of both the materials. Alginate-chitosan microspheres have been used to achieve embolization effects and release profiles for delivery of antineoplastic drugs to tumor sites [155]. Another example is chitosan with poly(organophosphazene) hydrogels, which is used to achieve loading capacity and prolonged release at the same time [156].

Due to its mechanically stable and tough properties, chitosan has become a highly studied compound in the field of bone tissue engineering. Because bones are very stiff, chitosan must be modified via crosslinking or coupled with a more rigid material. A ceramic of calcium phosphate can be used to make an external casing for a chitosan sponge. The ceramic provides the strength necessary while the bone regrows and the chitosan sponge provides a biologically active matrix in which osteoblasts can attach and lay down the mineralized matrix to regenerate bone [138].

One potential use could be the delivery of osteoinductive genes to a damaged area of the spinal cord. PLA-PEG bone grafts have been tested for spinal fusion techniques because of their stiff properties. Chitosan may be a good material to incorporate in these grafts to generate a material that has predictable degradation rates as well as large pores that can support new bone growth while maintaining the necessary strength before the bone has regenerated. The grafts can be made as hydrogels to enclose the osteoinductive

genes which would release slowly over time and speed up the formation of new bone to result in spinal fusion where there is a damaged disc [138].

The tissue engineering market is expected to be one of the leading applications of chitosan after drug delivery applications and chitosan is at the forefront of research. Chitosan hydrogel composites can be suitable as immunoisolation materials, chitosan-laminin or chitosan-alginate composites improve cell-scaffold interactions and chitosan-peptide materials can allow proliferation of human endothelial cells where chitosan alone will not [135]. These composites can be fine-tuned to potentially meet the focused needs of tissue engineering applications and wound healing applications, which also have emerging prospects for utilization of chitosan.

Chitosan is also involved in the production of magnetic nanofactories. The goal of these magnetic nanofactories is that they will be ingested orally and act as defense modules inside the body. In other words, they will be able to detect a bacterial invader, use the body's natural materials to synthesize an antibiotic and then employ this antibiotic in the body's defense.

Developed at the University of Maryland by Dr. Rohan Fernandes and Dr. William E. Bentley, what these nanofactories do mechanistically is alter the response of target cells by attaching to the surface of the cell and delivering specific "cargo" into it (Supplementary Figure 4). The initially developed nanofactories are dual-modulated. The first module is the cell capture module, which is comprised of chitosan and magnetite (chitosan-mag) and the second module is the synthesis module, which is in charge of synthesizing the substance that will alter response [157]. What this means is

that scientists will be able to initiate localized cellular therapy. Since the material is being synthesized at the site of the target cell, it will only be expressed there and there will be no side effects elsewhere in the body [158].

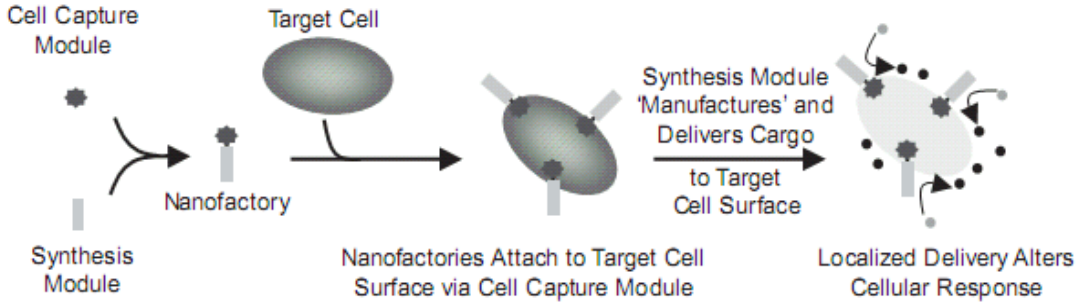

Supplementary Figure 4. The assembling of magnetic nanofactories involves the combination of a cell capture module and a synthesis module. The assembled nanofactory will attach to the surface of the cell, synthesize the "cargo" that will alter the response of the cell and then deliver it to the cell. ***Fernandes et. al. AI-2 biosynthesis module in a magnetic nanofactory alters bacterial response via localized synthesis and delivery. Biotechnology and bioengineering. 2009***

Recently, chitosan has been used a potential candidate for biomimetic scaffolds. For example, chitosan tends to form into film-like structures with long, tubal pores when it is freeze dried and lyophilized. These tubal pores are not inter-connected and range from ~120-150 microns in diameter. These pores, while appropriate for bone scaffolds, are too large to allow appropriate mechanical strength and would also not be sufficient for cellular compatibility. The average pore size for cells, nutrients and wastes to travel through in a scaffold should be between 50-200 microns in diameter. Pores larger than 200 microns will not allow for proper cell adhesion and poor proliferation [159].

In order to overcome this dilemma, Kim et. al. developed a protocol for developing interconnected porous scaffolds made of chitosan having high tensile strength in 2008.

The procedure involved dissolving chitosan in an acidic solvent (formic acid, trifluoroacetic acid, etc.) and then adding an organic aliphatic alcohol (THF, acetonitrile, etc.) that chitosan was not soluble in. A base (NaOH) was used to neutralize the pH of the solution and precipitate the chitosan into the organic solvent layer that was above the inorganic layer. Once precipitated, the product was freeze-dried and lyophilized so that a porous scaffold could be obtained. These scaffolds showed to have highly interconnected pores and a much higher tensile strength [159]. Tunable properties like this further enhance the versatility of chitosan as a biopolymer.

Supplementary Figures

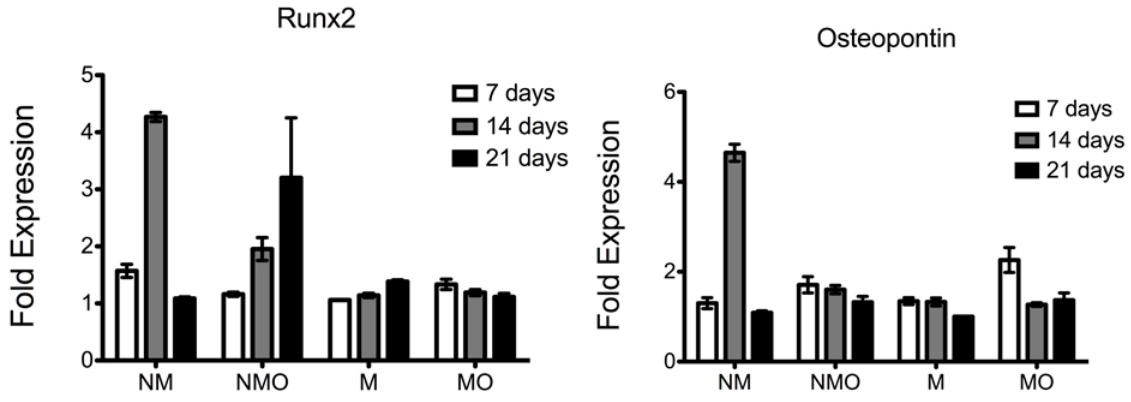

Supplementary Figure 5. An initial gene expression profile of Runx2 and Osteopontin was performed on the differentiation of MSCs towards an osteogenic lineage on CTS-GP scaffolds with and without HA to determine the osteoinductive capacity of the scaffolds. We obtained inconclusive results due to an inability to obtain pure RNA from the samples. We hypothesize that scaffold fragments contaminated the samples so the impurity results in unreliable data. The labels above are coordinated with CTS-GP (NM), CTS-GP in OGM (NMO), CTS-HA-GP (M) and CTS-HA-GP in OGM (MO).

Supplementary Figure 6. Upon collection of the samples, it was observed that 6 samples displayed that the scaffold was moved from its original implantation site and migrated elsewhere on the skull (middle skull shows it moved towards the center and right skull shows it moved down towards the nose). The skull to the left is a comparative sample where the scaffold remained in place.

Vita

FULL NAME: Michael Frohbergh

SCIENTIFIC TRAINING

- PhD Biomedical Science, Drexel University, December 2012
- Dual Bachelor of Art Chemistry and Biochemistry, LaSalle University, May 2007

RESEARCH EXPERIENCE

2008-2012 Research assistant, cranial and maxillofacial tissue engineering, Department of Biomedical Engineering, Science and health Systems, Drexel University

Advisor: Peter I. Lelkes

AWARDS AND HONORS

- Nominated for Teaching Assistant of the Year Award from the Department of the Biomedical Engineering, 2010-2011 and 2011-2012 academic year
- Instructor for the Drexel College of Medicine MiniMed Summer Program, July 2011
- Educational Chair of Sigma Phi Lambda Fraternity at La Salle University, 2004-2007.
- Awarded Founders Scholarship for academic excellence to LaSalle University, 2003 – 2007

PEER REVIEWED PUBLICATIONS AND PATENTS

- **Frohbergh, M.**, Katsman, A., Botta, G., Lazarovici, P., Wegst, U., Schauer, C. and Lelkes, P. (2011), *Electrospun Hydroxyapatite-Containing Chitosan Nanofibers Crosslinked with Genipin for Bone Tissue Engineering***,** Journal of Biomaterials, Accepted Manuscript
- New PCT Patent Appl. No. PCT/US11/55209, filed October 7, 2011 (Claims priority to U.S. Prov'l Appl. No. 61/390,918, filed October 7, 2010). Title: *Electrospun Mineralized Chitosan Nanofibers Crosslinked With Genipin For Bone Tissue Engineering*

In preparation

- **Frohbergh, M.,** Sunkari, C., Johnson, B. and Papazoglou E. (2011), *Development and Assessment of Laboratory Modules for Biomaterials in Tissue Engineering*, Journal of College Science Training.
- **Frohbergh ME**, Katsman A, Mondrinos M, Pimton P, Hankenson K, Oristaglio J, Lelkes P. *Bridging the Gap: The Osseointegrative Properties of Electrospun Hydroxyapatite-Containing Crosslinked Chitosan Nanofibrous Scaffold*.